NREL/TP-451-7045 • UC Category: 271 • DE94011847

In-Situ Characterization of Growth and Interfaces in a-Si:H Devices

Final Subcontract Report
1 May 1991 – 31 May 1994

R. W. Collins, C. R. Wronski, I. An,
Y. Lu, H. V. Nguyen
Pennsylvania State University
University Park, Pennsylvania

NREL technical monitor: B. von Roedern

MASTER

National Renewable Energy Laboratory
1617 Cole Boulevard
Golden, Colorado 80401-3393
A national laboratory of the U.S. Department of Energy
Managed by Midwest Research Institute
for the U.S. Department of Energy
under contract No. DE-AC02-83CH10093

Prepared under Subcontract No. XG-1-10063-10

July 1994

DISTRIBUTION OF THIS DOCUMENT IS UNLIMITED

Available to DOE and DOE contractors from:
Office of Scientific and Technical Information (OSTI)
P.O. Box 62
Oak Ridge, TN 37831
Prices available by calling (615) 576-8401

Available to the public from:
National Technical Information Service (NTIS)
U.S. Department of Commerce
5285 Port Royal Road
Springfield, VA 22161
(703) 487-4650

Printed on paper containing at least 50% wastepaper and 10% postconsumer waste

Major Sections of the Report

Preface

This report presents highlights of research performed from April 1, 1991 through May 31, 1994 under a cost-reimbursable, phased 3-year subcontract from National Renewable Energy Laboratory (a national laboratory of the U.S. Department of Energy operated by Midwest Research Institute) to The Pennsylvania State University (subcontract number XG-1-10063-10 to the prime contract DE-AC02- 83CH10093). The research was carried out under the direction of R.W. Collins, Professor of Physics and Materials Research, serving as principal investigator, with C.R. Wronski, Leonhard Professor of Electronic Materials and Devices, serving as co-principal investigator. Materials preparation and real-time optical studies were carried out in the Intercollege Materials Research Laboratory of The Pennsylvania State University, where the new technique of real-time spectroscopic ellipsometry has been invented recently. This technique has been applied as a powerful probe of amorphous semiconductor nucleation, growth, and interfaces throughout the subcontracted research, as described in detail in the following report. The *ex situ* electrical characterization was performed at the Electronic Materials and Processing Research Laboratory of The Pennsylvania State University. I. An contributed in each phase of this subcontract first as a graduate assistant and later as a post-doctoral researcher; currently he is Assistant Professor of Physics at Hanyang University in Korea. Y. Lu contributed as a graduate assistant in phases two and three. H.V. Nguyen contributed as both a graduate assistant and a post-doctoral researcher in phases two and three; currently he is a Staff Scientist at SGS-Thomson in Dallas, Texas. The contract monitor in the first phase of this project was B. Stafford, who was succeeded by B. von Roedern in the later phases. The authors are grateful for stimulating input throughout the later two phases from B. von Roedern. Helpful comments on the technical content and presentation of this report were provided by W. Luft. The authors are grateful to R. D'Aiello, B. Fieselman, and N. Maley of Solarex Thin Film Division and S. Guha of USSC for supplying the TCO's used in this study.

Individual Objective: The objective of this program is to identify materials parameters that can describe quantitatively the solar cell performance correctly in the initial and stabilized states and are consistent with a microscopic model of the metastable defect site. This objective is to be accomplished by applying results of *in-situ* analyses of a-Si:H surfaces and TCO/p/i interfaces to complement the present understanding of the electronic properties of materials and devices.

Wide-Gap Team Goal: Demonstrate, characterize, and understand improved doped and undoped "wide-gap" materials for use in achieving 15% stabilized photovoltaic modules. ("Wide-gap" materials are defined as those materials with a band gap ≥ 1.9 eV.)

Executive Summary

1. *Intrinsic a-SiC:H Materials (Sec. 1.1-1.2)*

The preparation parameter space for wide-gap intrinsic a-SiC:H has been explored further. For a-SiC:H prepared at the optimum H_2-dilution level of 20, the void volume fraction in the film increases continuously with decreasing substrate temperature below 250°C. In spite of this, we find that a-SiC:H can be prepared with excellent electronic properties at reduced temperatures. For example, the initial state electron ($\mu\tau$)-product for a-SiC:H prepared at 150-180°C is greater than that for a-SiC:H prepared at 250°C. [In the light soaked state, the electron ($\mu\tau$)-products for the two sets of samples are the same.] Other measurements of electronic quality corroborate such behavior. Because the lower temperature material has a wider optical gap by 0.05 eV (yielding E_g~2.00 eV), the lower temperature preparation approach may be preferable for the intrinsic layers in our wide-gap solar cells. More generally, the overall results suggest that there is not a strict correlation between electronic performance and ultimate void volume fraction as deduced from spectroscopic ellipsometry (SE). A strict correlation is observed, however, between the electronic performance and the degree of thin film coalescence deduced from the real-time SE in the initial nucleation stage. It is interesting to note that, for a-SiC:H prepared at the optimum H_2-dilution level of 20, the void volume fraction increases with decreasing substrate temperature at a rate lower than that for optimum a-Si:H prepared without H_2 dilution.

2. *P-Type a-SiC:H Materials (Secs. 1.2)*

Our previous experience with p-type a-SiC:H has suggested that a reduction in void volume fraction correlates with an enhancement in conductivity. Because of this, we have found that a substrate temperature of 250°C yields better p-type material. This temperature is higher than that believed to optimize the middle- or wide-gap i-layer. Our recent work, based on further scans through parameter space, suggest that p-type doped a-SiC:H layers deposited with low H_2-dilution ($[H_2]/\{[CH_4]+[SiH_4]\}\leq 1$ which weakens the TCO interaction) should also be deposited at the lowest power and pressure possible, and above a critical value of the total source gas flow. Such an approach is found to minimize the void volume fraction in the bulk film, all else being equal. We have found that if the total reactive gas flow is reduced below a critical value, the void volume fraction is dramatically increased. This provides direct evidence for the detrimental effect of feedgas depletion on the microstructure.

3. *Intrinsic a-SiC:H : Hydrogenation Effects (Sec. 1.3)*

We find significant differences in the post-hydrogenation characteristics of a-Si:H (8 at.% initial H) and a-SiC:H (20-25 at.% initial H). During exposure to atomic H, a significant number of Si-Si bonds are broken and converted to Si-H bonds within the top 200 Å of the a-Si:H film. This evidently relaxes strain in the network. A similarly strong effect is not observed for a-SiC:H, and the primary effect of diffusing H is to exchange with H in some fraction of the existing Si-H bonds in the network. The different post-hydrogenation behavior observed for the two materials is attributed to the fact that the a-SiC:H network, with its higher H-content, is already effectively relaxed. Our studies suggest that the H which relaxes the a-Si:H network diffuses through Si-Si bond configurations, and not through the void network or Si-H configurations.

4. *P-Type a-Si:H : Hydrogenation Effects (Sec. 2.2)*

A 1.92 eV optical gap p-layer 200 Å thick can be obtained by in-situ hydrogenation of a pure (unalloyed) a-Si:H:B layer. The hydrogenation effect widens the optical gap of the p-layer by a surprising ~0.2 eV. Thus, in-situ hydrogenation over-corrects the band-gap narrowing typically observed with B-doping and provides a possible way of improving the p-layer transparency in a simple processing step. Further studies are ongoing in the cell configuration to see if this processing step is detrimental to the p-layer conductivity. Further studies are also being done to see whether the near-surface of the p-layer can be crystallized using a sufficiently high H flux.

5. *SnO_2/p-layer Interfaces (Sec. 3)*

In earlier work in Phase II, we found that H_2-dilution and substrate temperature are the critical a-SiC:H growth parameters that control the reduction of SnO_2 and determine the amount of interfacial free metal generated when a-SiC:H is deposited on SnO_2. In this study, we find that the concentration of gas phase diborane, used in the formation of the TCO/p-layer interface, is not a critical parameter and has no detectable effect on the process of SnO_2 reduction to free metal. Paradoxically, we find that the reduction of the SnO_2 to free metal actually increases the sheet resistance of the transparent conducting oxide due to a near-interface void structure that forms when the SnO_2 is eroded by plasma exposure. This may reduce the contact area in the device. However, B does seems to play a role to the extent that its presence in the gas phase leads to a greater increase in the sheet resistance of the SnO_2 upon interface formation. This effect appears to be electrical rather than microstructural in nature since it is not correlated with any observed change in the optical characteristics of the interface.

6. *ZnO/p-layer Interfaces (Sec. 4)*

Although free metal is not detected at the ZnO/a-SiC:H:B interface, even under high H_2-dilution conditions of microcrystallite growth, real-time spectroscopic ellipsometry reveals optical changes that can be attributed to ZnO modification by H and B penetration. The optical changes are characterized by an increase in the band gap in the ZnO that results from the Burstein-Moss effect, namely an increase in the Fermi level position higher in the conduction band. As a result, the real-time optical measurement is sensitive to an increase in the carrier concentration that occurs in the ZnO in the near-interface region upon ZnO/a-SiC:H:B interface formation. Typical increases in carrier concentration of 10^{20} cm^{-3} occur in ZnO to a depth of 100-300 Å, depending on a-SiC:H:B preparation conditions. Such changes have been corroborated by SIMS and by qualitative measurements of sheet resistance, before and after interface formation, and are attributed to the generation of Zn interstitials and/or oxygen vacancies by H and to additional doping by B. Similar effects can also occur upon annealing the ZnO at 300°C. We have found no optical or electrical evidence for the formation of a barrier between the ZnO and a-SiC:H:B that would block the transfer of holes in the solar cell configuration.

7. *Microcrystalline SiC:H (Sec. 5.1)*

Films of $Si_{1-x}C_x$ ~1000 Å thick prepared by conventional PECVD at a high source-gas H_2 dilution level of 80 and at variable CH_4:SiH_4 flow ratios up to 1.5:1 (in sccm) consist of Si microcrystals embedded in an a-SiC:H matrix. The C stabilizes the amorphous intergranular phase, but this phase also leads to a more compact film with a lower volume fraction of intergranular voids. Previous observations of shifts to higher energies in the E_0'-E_1 critical point complex in the band structure of the Si microcrystallites are not due to C incorporation in the crystallites, but rather to strain that develops in the coalescing film. Such strain leads to a reduction in the absorption coefficient of the film in the blue part of the spectrum.

8. *Thin P-Type μc-Si:H Prepared by VHF-PECVD (Sec. 5.2)*

The reduction with decreasing thickness in the conductivity for 200 Å → 100 Å μc-Si:H:B p-layers prepared by VHF-PECVD onto glass substrates appears to correlate well with a decline in the crystalline volume fraction in such layers. This emphasizes the importance of achieving a high crystallite nucleation density on the substrate in order to achieve high conductivity p-layers [see: 9. Control of Nucleation in μc-Si:H].

9. *Control of Nucleation in μc-Si:H (Sec. 5.3)*

We have studied single cycles consisting of a-Si:H growth on a Cr substrate, followed by etching with thermally-generated atomic H. Using this approach, we have successfully prepared ultrathin layers (6-12 Å) of relatively dense, single-phase μc-Si:H. Real-time monitoring provides monolayer-level endpoint detection in this process and allows one to identify the phase-purity of the residual crystalline layer on the substrate. The advantage of the growth/etch processing demonstrated here is the ability to obtain a high density μc-Si:H phase as a nucleation promoter at the substrate interface for substrates onto which conventional PECVD μc-Si:H will not readily nucleate. With this approach, difficult interface problems such as ZnO/μc-Si:H:B may be readily resolved.

10. *Real-time Monitoring of a-Si:H-Based Solar Cells in Single-chamber System (Sec. 6.1)*

Techniques have been developed to characterize the formation of the TCO/p/i structure of a solar cell using real-time spectroscopic ellipsometry. This measurement is performed during preparation of optimum p- and i-layers in a single-chamber system. Because the specular SnO_2 TCO that we use is rough on a microscopic scale, the optical modeling is more complex than for a-Si:H:B depositions on smooth c-Si surfaces. We deduce the following information: (a) SnO_2/p-layer interface roughness and free metal (Sn) content in mass thickness, (b) bulk p-layer thickness and optical properties, including optical gap, (c) p/i interface roughness, (d) total p-layer mass thickness, (e) CVD contamination layer mass thickness and optical gap, (f) i-layer thickness and optical properties including optical gap. In our studies, the p-layer is prepared under conditions that minimize SnO_2 reduction to metal. The resulting devices co-deposited on both ZnO and SnO_2 TCO's exhibit similar initial efficiencies of 5%. Thus, the efficiency appears to be limited in our case, not by any TCO/p interface effects, but by a ~20 Å mass thickness a-SiB:H CVD layer with a 1.5 eV optical gap formed during single-chamber flushing between depositing the p- and i-layers. In future work, procedures to eliminate this effect and improve efficiency will be studied using real-time spectroscopic ellipsometry. These include atomic H-treatments after p-layer deposition, buffer layers, and the use of a tri-methyl boron dopant gas.

11. *a-Si:H-Based Solar Cells in Multichamber System (Sec. 6.2)*

Baseline cells have been prepared in a multichamber system having an initial efficiency of ~8%. Our real-time spectroscopic ellipsometry studies have shown that some amount of p/i interface contamination is still likely in this cell in spite of the flushing of the p-layer chamber which is done to prevent p/i chamber cross-contamination. Crude initial attempts to passivate these defects using a special H-treatment in the i-layer chamber have led to an increase in V_{oc} and J_{sc}. Further optimization of the interface using the H-treatment will be undertaken.

12. *General Interface Phenomena (Sec. 3-4, 6)*

A detailed tabulation of the interface effects that represents a summary of our Phase I-III studies appears in Table VI, as a convenience to the casual reader.

Table of Contents

Table of Contents (ctd.)

1. Scanning Preparation Parameter Space: Undoped a-SiC:H Thin Films

1.1 *Overview and Summary of Phase II Studies of Undoped a-SiC:H*

Figure 1 provides a summary of some of the important microstructural and electronic effects of H_2-dilution of the source gases used in plasma-enhanced chemical vapor deposition (PECVD) of SiC:H alloy films. The H_2 dilution along the abscissa is defined as the ratio of the H_2 gas flow to the total source gas flow; i.e., $R=[H_2]/\{[SiH_4]+[CH_4]\}$. R varies from 0 to 40 for the films of Fig. 1 while the SiH_4:CH_4 gas flow ratio is fixed at 3:2 in order to achieve a Tauc gap ~1.92 eV for the amorphous alloys. Other PECVD conditions are as follows: 250°C substrate temperature, 5 W rf power (130 mW/cm^2), and 0.085 Torr partial pressure of source gases. The behavior in Fig. 1 can be demarcated into two regimes (see broken vertical line).

For $R \leq 20$, the films are a-SiC:H, and in this regime the microstructural inhomogeneity, defect density [as measured by α(1.2 eV)], and disorder [as measured by the inverse Urbach slope] tend to decrease with increasing R. In addition for $R \leq 20$, the H-content is constant at 20-25 at.% and the C-content is also constant at x=0.09 (in a-$Si_{1-x}C_x$:H). Thus, the optical Tauc gap remains constant at ~1.95 eV to within ±0.02 eV.

For $R \geq 30$, however, the films are two-phase a-SiC:H/μc-Si:H, and in this regime the inhomogeneous microstructure and apparent defect density increase with increasing R. The nature of these films will be discussed in greater detail later (see Sec. 5.1). Available data suggests that the amorphous component has a similar C content as the fully amorphous films with $R \leq 20$; thus the net C concentration in the film is reduced as the c-Si volume fraction increases [see Fig. 1, second panel from top].

Overall, Fig. 1 shows that for standard PECVD there exists a well-defined optimum in the bulk electronic properties of the alloys for a H_2-dilution ratio of 20-25. One can describe this optimum as corresponding to the maximum H_2 dilution that can be sustained without the formation of the crystalline phase.

Real-time spectroscopic ellipsometry (RTSE) provides insights into the origin of this optimum. The lower panel in Fig. 1 shows the amount of surface smoothening that the a-SiC:H undergoes in the first 50 Å of bulk film growth when thin film nuclei ~20 Å thick make contact and gradually coalesce with increasing film thickness. In the regime with $R \leq 20$, coalescence is enhanced with increasing R. This may be due to (i) the enhancement of precursor surface diffusion by more effective H termination of the film surface (Tanaka and Matsuda, 1987) and/or (ii) the promotion of SiC network crosslinking due to more rapid interchange of H between the gas phase and the surface (Camargo and Beyer, 1989). For $R \geq 30$, coalescence weakens with increasing R. This may be due to H-atom etching of the bonds that connect the neighboring

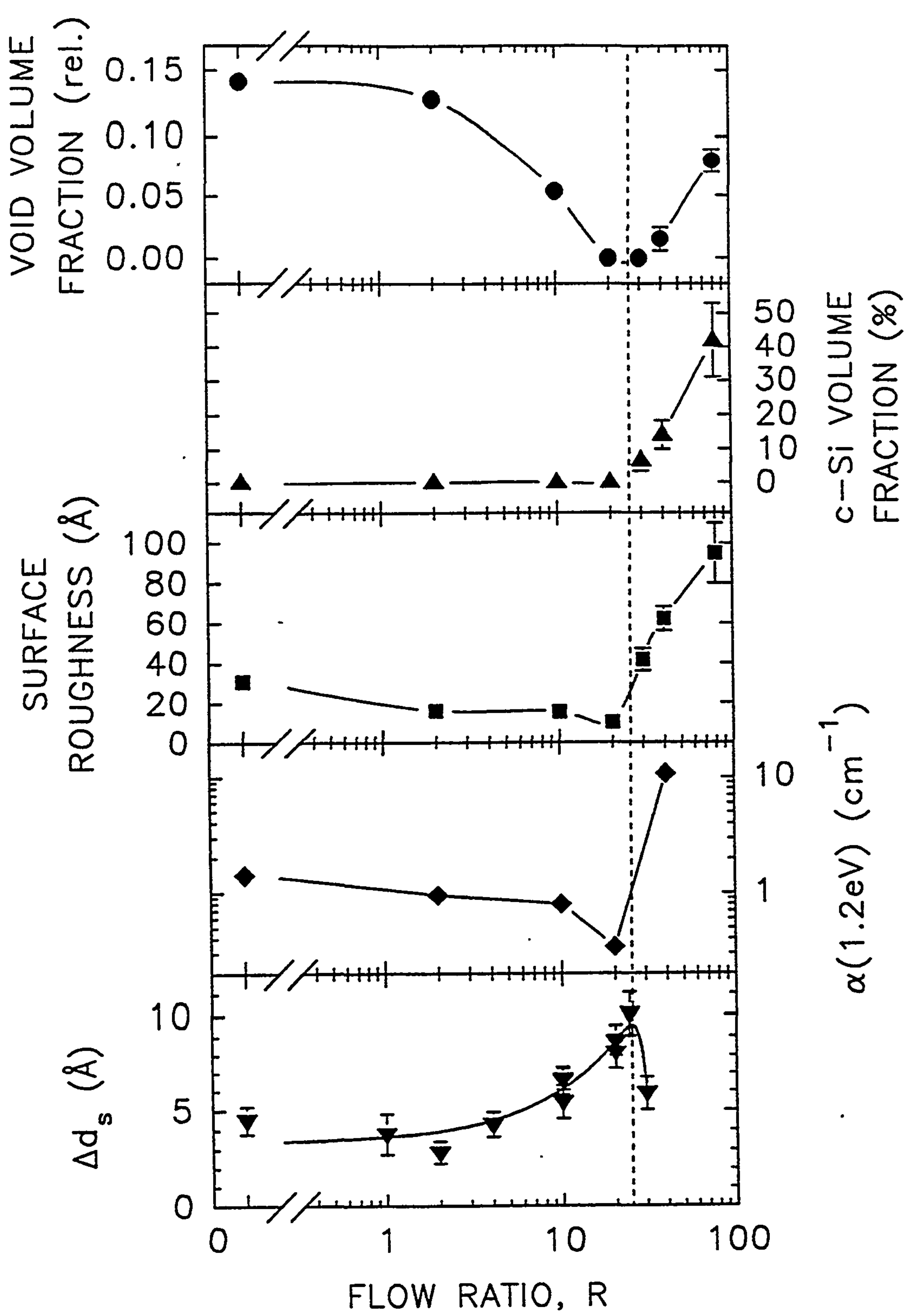

Figure 1. Microstructural and electronic properties of a-SiC:H alloy films (0.3-0.8 μm thick) prepared over a wide range of H_2-dilution (upper four panels). From top to bottom: void volume fraction, crystalline Si volume fraction, surface roughness thickness, and absorption coefficient at 1.2 eV. In the lowest panel, the magnitude of the coalescence characteristic in the first 50 Å is shown for the growth of thinner films. The following conditions were fixed: 250°C substrate temperature, 5 W rf power, and 0.085 Torr partial pressure of source gases. The total source gas flow was decreased from 5 sccm to 2.5 sccm as the dilution level increased above R=20.

microstructural units (Tsai, 1988).

Optimum coalescence at R=20-25 as detected by RTSE leads to a bulk film having the lowest volume fraction of voids and the smoothest surface, as shown by the top and center panels in Fig. 1, deduced from spectroscopic ellipsometry (SE) measurements on thick films.

We suggest that there is a causal relationship between the optimum microstructural evolution, and the minimum in the midgap and band tail defect density. It is likely that the enhanced surface diffusion, hydrogen exchange, and crosslinking lead to a more-ordered, lower defect density network (Luft and Tsuo, 1993). It is expected that defects associated with Si-CH_3 and sp^2 C units in the film are reduced through these processes, as well (Mahan et al., 1985; Camargo and Beyer, 1989).

1.2 *Studies of a-SiC:H in Phase III: Excursions through Preparation Parameter Space Guided by Real Time Spectroscopic Ellipsometry*

In Phase II, we studied the effect of H_2-dilution of the source gases on the microstructural and electronic properties of intrinsic a-SiC:H as described in Sec. 1.1 (Collins et al., 1994a). Other preparation parameters were fixed at values typical of those used for pure a-Si:H, e.g., minimum rf power density and 250°C substrate temperature. If wide-gap intrinsic a-SiC:H alloys are to be fully optimized, the effect of these other parameters on the film properties should be better understood, as well. In addition, the preparation of the highest quality *doped* a-SiC:H onto transparent conducting oxides may also benefit from any insights that can be obtained. Thus, one goal for the doped material studies is to identify the SiH_4/CH_4 plasma conditions that yield homogeneous, high density a-SiC:H films, keeping in mind the limitations associated with the reduction of the transparent conducting oxide (TCO). These plasma conditions can then be considered for our p-type a-SiC:H deposition. The rationale is that a dense, microstructurally uniform amorphous film with the lowest disorder (short of crystallinity, which requires H_2 dilution with its potential detrimental effects on the TCO) can be doped most efficiently.

RTSE provides a convenient way of scanning wide ranges of parameter space quickly and expeditiously. With this technique a series of thin films, each with a different set of process parameters, is deposited onto the same substrate. From the SE measurements collected in real-time, the bulk film void volume fraction and the optical gap (appropriate for the substrate temperature of measurement) can be estimated. Obviously, such measurement does not present a full picture, but it does provide valuable insights into the growth mechanisms and the directions that parameters may need to be adjusted. The ultimate test will come from the preparation and analysis of solar cells. In fact, the input from RTSE described in this section is currently being used to direct the preparation of wide-gap cells in Penn State's multi-chamber system. Given the extensive volume of preparation parameter space, we believe device improvements are better achieved through an understanding of the deposition process.

As an example of the approach, Fig. 2 shows the relative void volume fraction and optical gap shift versus H_2 dilution, obtained from RTSE by depositing a sequence of ~1700 Å thick a-SiC:H films without changing substrates. The following fixed parameters were used: 250°C substrate temperature; 5 W rf power; and 0.08 Torr partial pressure of source gases. For the over-layered samples of Fig. 2, the trend in void fraction with H_2-dilution (solid points) matches the results obtained for the samples in Fig. 1, top panel, (reproduced in Fig. 2 as the diamond points) within the expected experimental error of ±0.01. Second, the shift in the optical gap, no more than ±0.03 eV over the full range $0 \leq R \leq 20$, is also in agreement with the results described in Sec. 1.1 on separate bulk films, at least within experimental error. The latter two observations attest to the validity of the RTSE methods.

Note that in Fig. 2, the optical gap for R=20 is provided as 1.7 eV. The difference between this value and the value obtained from ex situ transmission and reflection data quoted above (1.92 eV) arises from two sources. First, the RTSE data were collected at 250°C where the gap is ~0.15 eV lower than that at 25°C. Second, the RTSE data were analyzed using the constant dipole matrix element method due to Cody, whereas the ex situ data were analyzed by the constant momentum matrix element method due to Tauc (Cody, 1984). The former approach leads to a gap that is ~0.08-0.1 eV lower than the Tauc gap at the same temperature. Thus, the combined effects lead to a gap difference of about 0.25 eV between the Tauc gap and the gap obtained by RTSE at 250°C.

Now that confidence has been established in the RTSE methods, we investigate the effect of the other deposition parameters using these methods. This is just a first step toward the final objective of our optimization studies, which is to establish conditions to be employed for undoped and doped a-SiC:H, the latter to be prepared on TCO's such as SnO_2 and ZnO. Some insights provided by RTSE assist us in doing this with a minimum of time and effort. For the doping applications of a-SiC:H, we focus on low H_2-dilution, i.e., R=1. Above this dilution level, SnO_2 reduction to elemental Sn increases above the monolayer level.

1.2.1 Effect of Substrate Temperature on Void Volume Fraction and Optical Gap

Figure 3(a) shows the relative void volume fraction (top) and optical gap shift versus substrate temperature, obtained from real-time SE by depositing a sequence of ~1700 Å thick a-SiC:H films without changing substrates. The following fixed parameters were used: R=20, i.e., moderate H_2-dilution ratio; 5 W rf power; 0.52 Torr total pressure; 0.085 Torr partial pressure of source gases; and 5 sccm total source gas flow. The solid line result for the optical

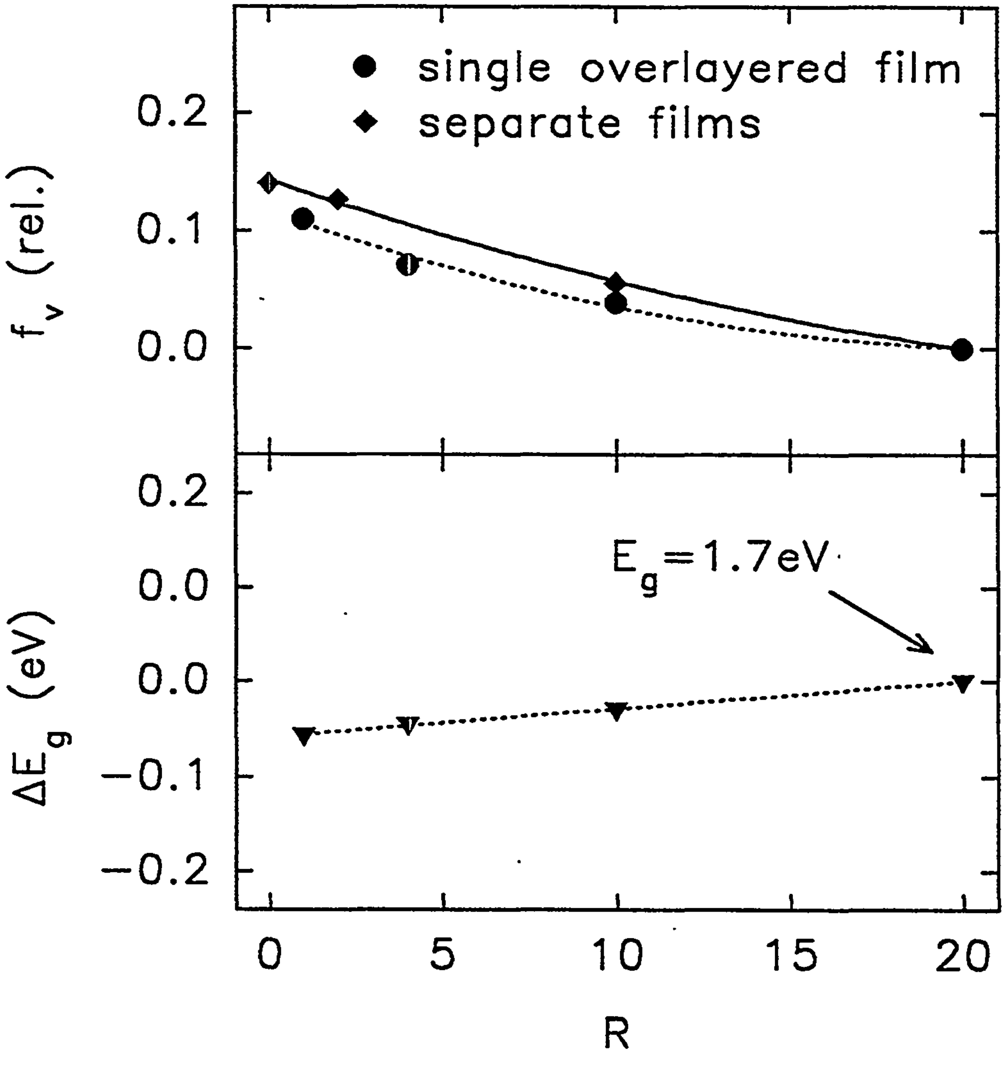

Figure 2. Relative void volume fraction (top) and optical gap shift (bottom) versus H_2 dilution ratio, obtained from real-time SE by depositing a sequence of thin a-SiC:H films without changing substrates (circular and triangular points, respectively). The results for the void volume fraction obtained from a series of individual films is also shown (diamond-shaped points). The following fixed parameters were used: 250°C substrate temperature; 5 W rf power; 0.085 Torr partial pressure of source gases; 5 sccm total flow of source gases.

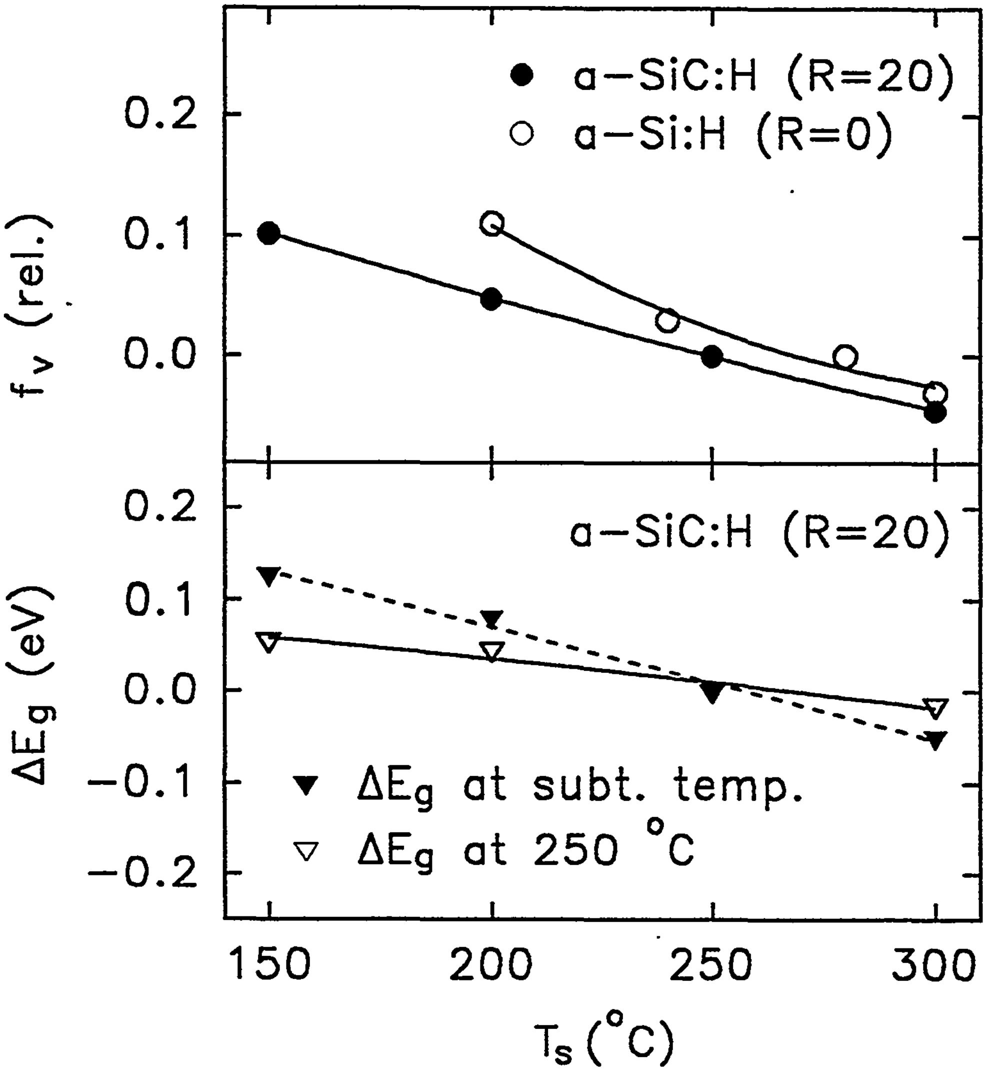

Figure 3(a). Relative void volume fraction and optical gap shift versus substrate temperature, obtained from real-time SE by depositing a sequence of thin a-SiC:H films at moderate H_2-dilution (R=20) without changing substrates (solid points and triangles, respectively). The results for the void volume fraction obtained from a series of individual a-Si:H films prepared without H_2-dilution is also shown in the top panel (open points). At the bottom, the observed optical gap shift (solid triangles) for the a-SiC:H sequence has been corrected for the measurement temperature dependence of the optical gap (open triangles). The following fixed parameters were used for the a-SiC:H films: R=20 H_2-dilution ratio; 5 W rf power; 0.52 Torr pressure of total gases; 0.085 Torr partial pressure of source gases; 5 sccm total source gas flow.

gap variation in the lower panel includes a correction to account for the intrinsic shift of the gap with measurement temperature, estimated in this case to be a linear function of temperature over this range with a coefficient of 7.7×10^{-4} eV/K (Weiser and Mell, 1989). Additional results for the void fraction versus temperature were obtained on unalloyed a-Si:H, prepared without H_2-dilution in a multichamber deposition system and measured ex situ (open points, top panel).

For a-Si:H, optimization of the substrate temperature represents a trade-off between the formation of SiH_n (n>1) bonded units (and the microstructure associated with them) at low substrate temperature and the generation of dangling bonds at high substrate temperature (Luft and Tsuo, 1993). This optimization should be undertaken in the cell configuration, and this has been done for the Penn State a-Si:H-based solar cells. The results of such a study yield an optimum temperature of 200°C, and this is used for the intrinsic layer in our middle-gap baseline solar cell (see Sec 6.2).

In spite of the insensitivity of the real-time optical measurement to the dangling bond component, the results of Figure 3(a) do provide some useful information for input into intrinsic layer preparation. First, the top panel of Fig. 3(a) shows that voids develop in the a-SiC:H with decreasing substrate temperature at a lower rate than in the a-Si:H prepared without dilution. Thus, it is not unreasonable to assume that a substrate temperature lower than the optimum one for a-Si:H would remain acceptable for intrinsic a-SiC:H, which is to be prepared at this moderate H_2-dilution level (R=20). Also, Fig. 3(a) shows that the band-gap shift achieved by preparing the a-SiC:H at 175°C, rather than our previous standard of 250°C, is about 0.04-0.05 eV. These considerations will be of relevance when the electronic properties of intrinsic a-SiC:H prepared at lower temperature are discussed further (see Sec. 1.2.5).

Figure 3(b) reveals very similar trends in the void volume fraction and optical gap versus substrate temperature for a-SiC:H prepared with a fixed H_2-dilution level of R=1. This dilution level is acceptable for doped layer preparation. With this dilution level also, voids appear to develop in the a-SiC:H with decreasing substrate temperature at a lower rate than in the a-Si:H films of Fig. 3(a). Thus, a substrate temperature lower than the optimum one for a-Si:H would also seem to be acceptable for doped a-SiC:H. However, we note here that the doping efficiency appears to be very sensitive to the void structure that develops at low substrate temperature, as has been evidenced by a decreasing conductivity with decreasing temperature (see Sec. 2.1) (Chen and Wronski, 1993). As a result, the doping studies of Sec. 2 have been confined to a substrate temperature of 250°C. This observation also suggests that we use all the deposition parameters at our disposal to reduce the void volume fraction for doped films.

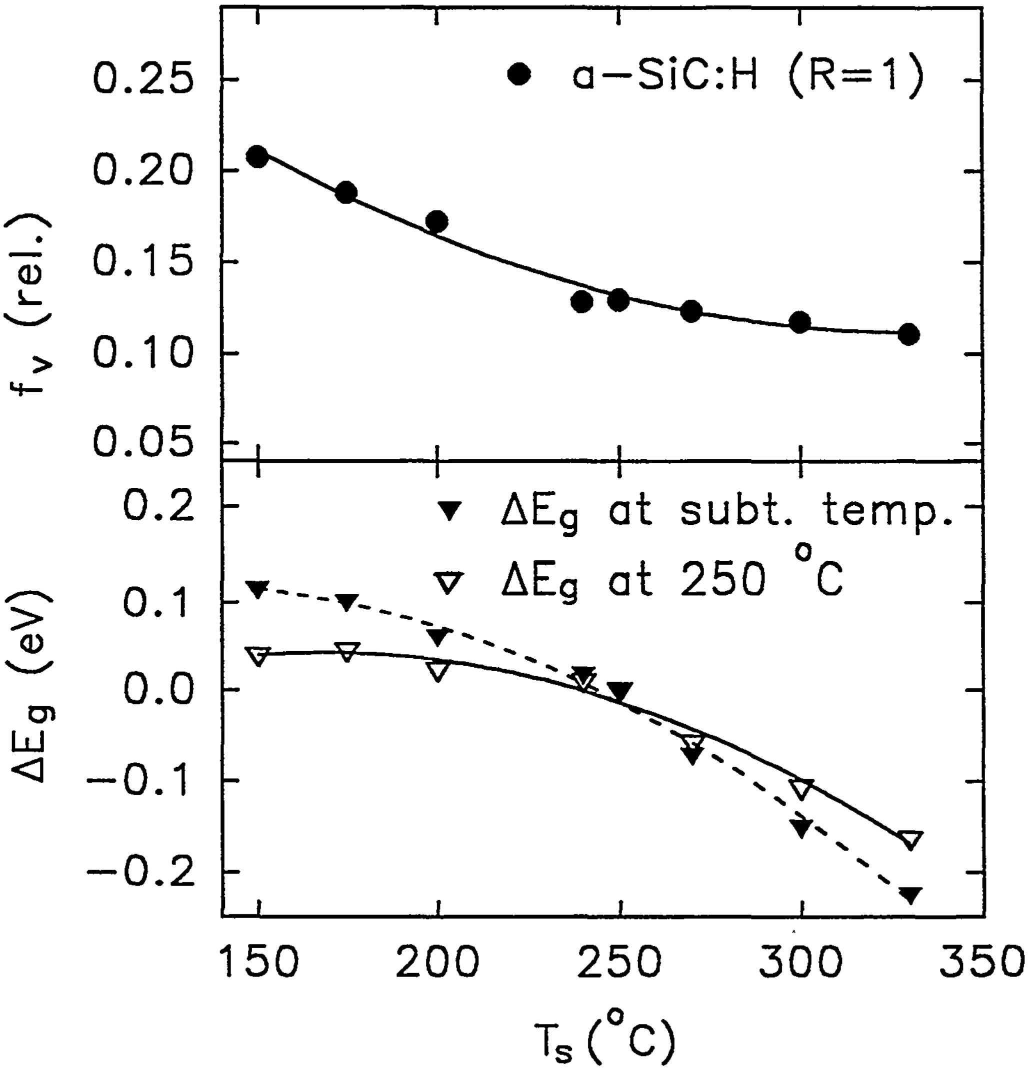

Figure 3(b). Relative void volume fraction and optical gap shift versus substrate temperature, obtained from real-time SE by depositing a sequence of thin a-SiC:H films at low H_2-dilution (R=1) without changing substrates. At the top, the void volume fraction is measured relative to the high density films prepared with R=20 and T_s=250°C. At the bottom, the observed optical gap shift (solid triangles) has been corrected for the measurement temperature dependence of the optical gap (open triangles). The following fixed parameters were used: R=1 H_2-dilution ratio; 5 W rf power; 0.17 Torr pressure of total gases; 0.12 Torr partial pressure of source gases; 10 sccm total source gas flow.

1.2.2 Effect of Plasma Power on Void Volume Fraction and Optical Gap

Figure 4 shows the relative void volume fraction and optical gap shift versus rf plasma power obtained from real-time SE by depositing a sequence of thin a-SiC:H films without changing substrates. The following fixed parameters were used: R=1 H_2-dilution ratio; 240°C substrate temperature; 0.17 Torr pressure of total gases; 0.12 Torr partial pressure of source gases; and 10 sccm total source gas flow. The top panel in Fig. 4 shows that in order to minimize the void volume fraction, the rf power should be kept at the minimum possible value. In addition, the effect of the rf power on the optical gap is relatively weak. As a result, in our studies of doped and intrinsic a-SiC:H, we operate at the lowest possible plasma power while maintaining a high stability plasma at the optimum gas pressure and flows (see Secs. 1.2.3-4). This turns out to be ~5 W (or ~100 mW/cm^2). This approach is similar to that typically used in our unalloyed a-Si:H deposition and midgap cell preparation.

1.2.3 Effect of Gas Pressure on Void Volume Fraction and Optical Gap

Figure 5(a) shows the relative void volume fraction versus total pressure obtained from real-time SE by depositing a sequence of thin a-SiC:H films without changing substrates. The following fixed parameters were used: R=1 H_2-dilution ratio; 5 W rf plasma power; 240°C substrate temperature; and 10 sccm total source gas flow. The effects of pressure on the microstructure are relatively weak compared to temperature and power. Overall it can be concluded that the lowest pressure, achieved with the pumping port butterfly wide open, yields the lowest void volume fraction. For doped films with R=1 with a total gas flow of 20 sccm, this corresponds to a pressure of 0.17 Torr for our pumping system. In the case of the a-SiC:H alloys, some degree of physical bombardment at the lower pressures may lead to the same effect as H_2-dilution, namely, the promotion of precursor diffusion and enhancement of coalescence through more rapid exchange of H between the surface and the gas phase.

1.2.4 Effect of Source Gas Flow on Void Volume Fraction and Optical Gap

In Figure 5(b), we show the relative void volume fraction versus total source gas flow obtained from real-time SE by depositing a sequence of thin a-SiC:H films without changing substrates. The following fixed parameters were used: R=20 H_2-dilution ratio; 5 W rf plasma power; 240°C substrate temperature. These results show that when the total gas flow is reduced below 5 sccm for R=20, there is a rapid increase in the void volume fraction. This effect is consistent with source gas depletion. Depletion is believed to lead to more reactive radicals in the

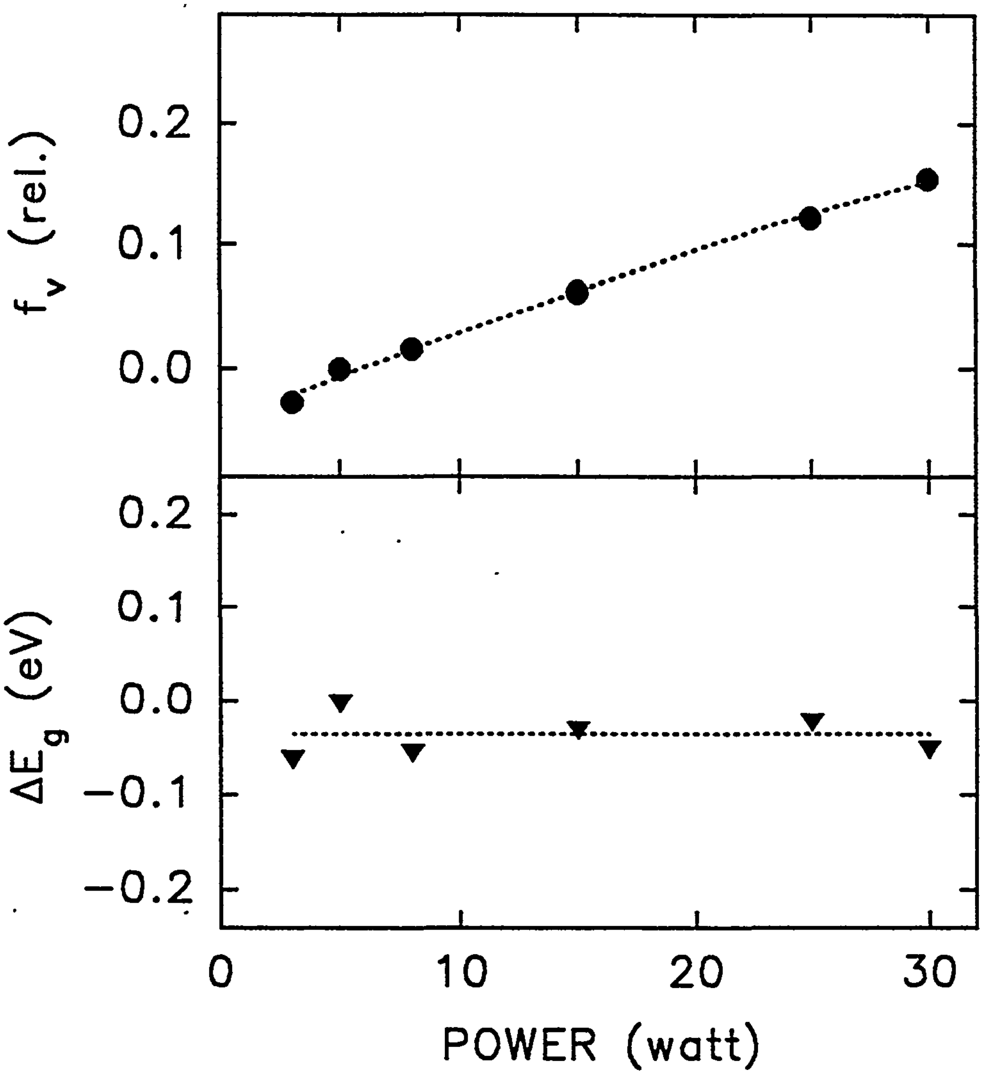

Figure 4. Relative void volume fraction (top) and optical gap shift (bottom) versus rf plasma power obtained from real-time SE by depositing a sequence of thin a-SiC:H films without changing substrates. The following fixed parameters were used: R=1 H_2-dilution ratio; 240°C substrate temperature; 0.17 Torr pressure of total gases; 0.12 Torr partial pressure of source gases; 10 sccm total source gas flow.

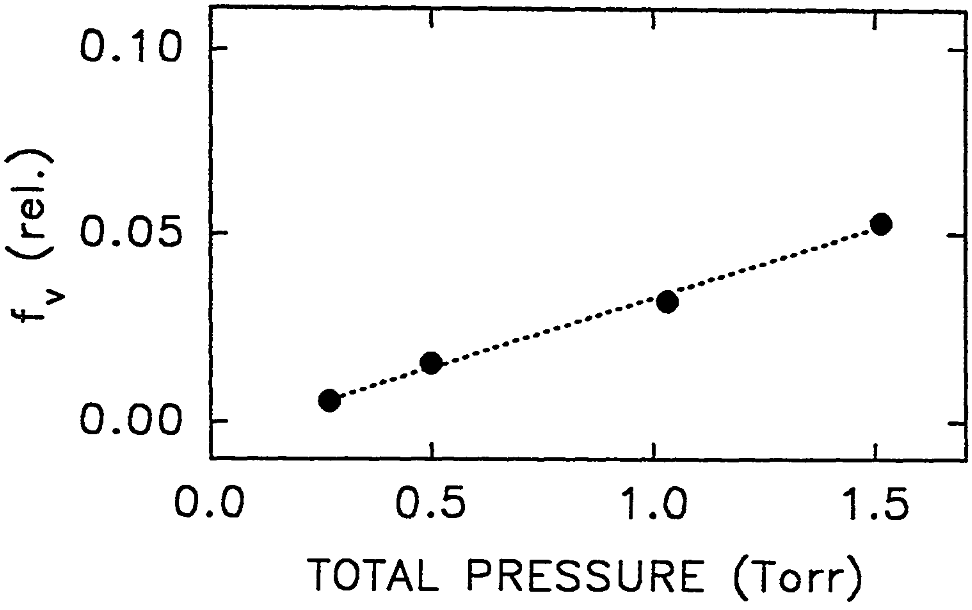

Figure 5(a). Relative void volume fraction versus total pressure obtained from real-time SE by depositing a sequence of thin a-SiC:H films without changing substrates. The following fixed parameters were used: R=1 H_2-dilution ratio; 5 W rf plasma power; 240°C substrate temperature; 10 sccm total source gas flow.

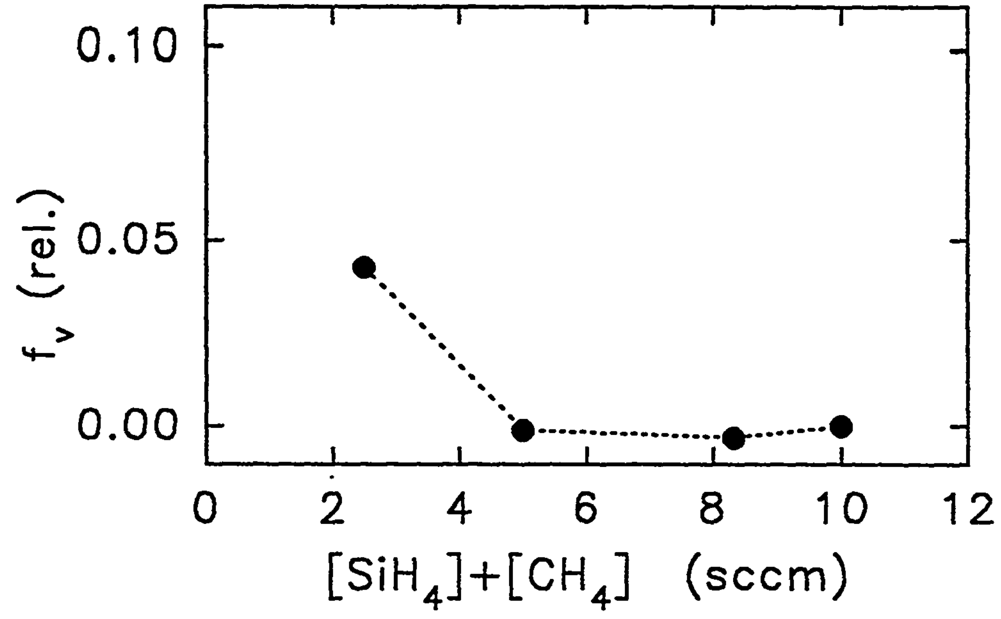

Figure 5(b). Relative void volume fraction versus total source gas flow obtained from real-time SE by depositing a sequence of thin a-SiC:H films without changing substrates. The following fixed parameters were used: R=20 H_2-dilution ratio; 5 W rf plasma power; 250°C substrate temperature.

gas phase, which exhibit a reduced surface diffusion length. This in turn leads to microstructural heterogeneity, as observed in Fig. 5(b). In general, we choose the source gas flow to be as high as possible, while still maintaining a low pressure. For doped films with R=0-1, for example, we use a source gas flow of 10 sccm.

1.2.5 Further Optimization of the Electronic Properties of Undoped a-SiC:H

Single, thick wide-gap alloys have been prepared with a H_2-dilution level of R=20 and a substrate temperature of 180°C, under otherwise similar deposition conditions as the samples of Fig. 1. This work was motivated by the observations of Fig. 3(a). We find that the measured electronic properties of this lower temperature material are essentially the same as its higher substrate temperature counterpart shown in Fig. 1. As an example of this, Figs. 6(a) and (b) depict the photoconductivity and the electron ($\mu\tau$)-product versus generation rate for three samples: one with R=20 and T_s=250°C, a second with R=0 and T_s=250°C, and a third with R=20 and T_s=180°C. This comparison reveals the improvement obtained at T_s=250°C through H_2-dilution, in consistency with the results of Fig. 1. It also shows the relatively weak effect of substrate temperature on electronic properties. A similar conclusion is reached, based on the corresponding α(1.2 eV) data.

These latter observations force us to conclude that a strict correspondence does not occur between the minimum void volume fraction and the optimum electronic properties. If such a correspondence were to occur, then the electronic properties should degrade as the substrate temperature is reduced from 250°C to 180°C, and the substrate temperature should be increased to 300°C (rather than decreased as in Figs. 6) in order to achieve improved properties. [We have not explored these higher temperature conditions because of the problems at the TCO/p interface that appear to be exacerbated with increasing temperature (see Sec. 3).] The observed breakdown in the connection between void fraction and electronic properties may result from (i) the insensitivity of microstructural measurements to isolated dangling bonds and/or (ii) the insensitivity of electrical measurements to some isolated-H-induced density deficit. As an example of the former situation, a-Si sputtered without H can be prepared with very high density, but its electronic properties are poor due to the presence of isolated dangling bonds. As an example of the latter situation, the higher H-content in materials prepared at low substrate temperatures may lead to a lower density of Si-Si bonds without additional electronically active defects. Thus, the trends in the void volume fraction in Figs. 1-5 need to be interpreted with care. In further work, we will investigate whether the breakdown in this correlation is confined to the substrate temperature process variable. For other variables such as plasma power which tend to control the development of columnar microstructure, the correlation most likely remains valid, based on

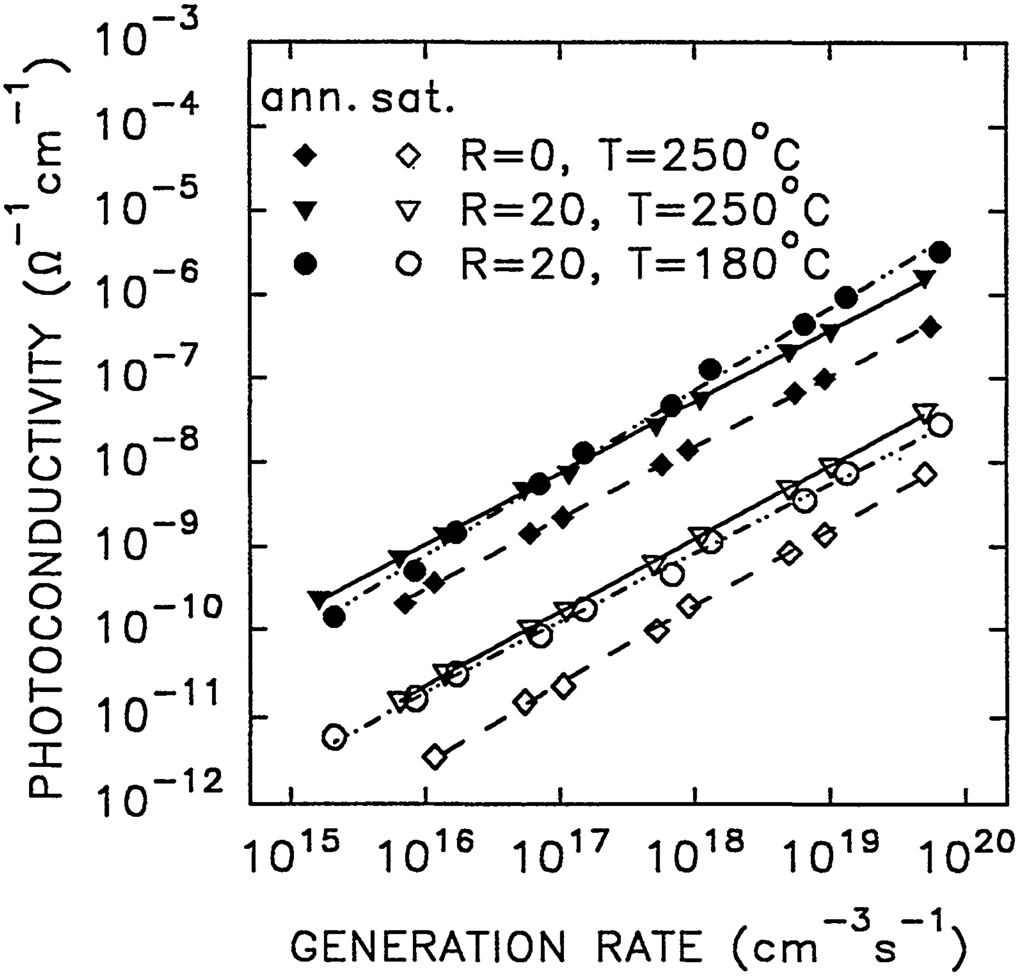

Figure 6(a). Photoconductivity as a function of generation rate for three films of a-SiC:H in both annealed (ann.) and fully light-soaked (sat.) states. Films wth R=20 were prepared at 180°C and 250°C; films at T_S=250°C were prepared with R=0 and R=20. The following conditions were fixed: 5 W rf power; 0.085 Torr partial pressure of source gases; 5 sccm source gas flow.

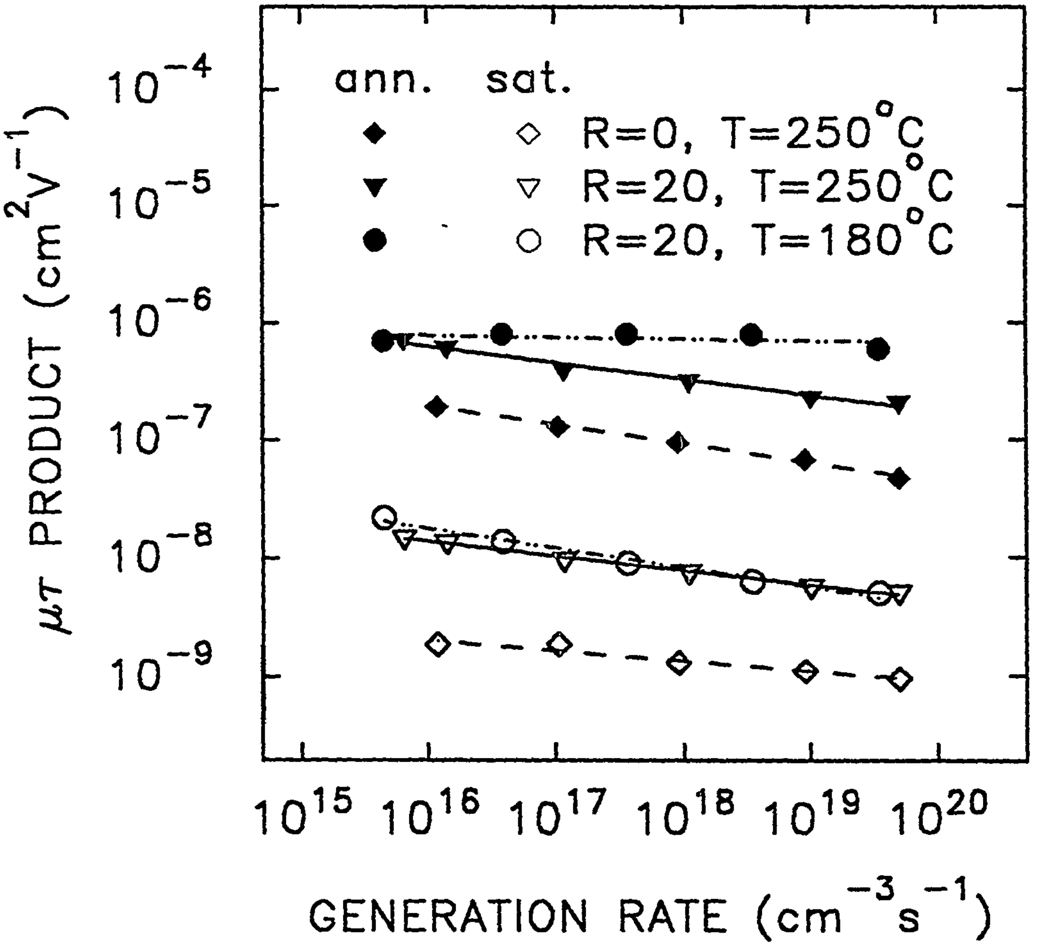

Figure 6(b). Electron ($\mu\tau$)-product as a function of generation rate for three films of a-SiC:H in both annealed (ann.) and fully light-soaked (sat.) states. Films wth R=20 were prepared at 180°C and 250°C; films at T_S=250°C were prepared with R=0 and R=20. The following conditions were fixed: 5 W rf power; 0.085 Torr partial pressure of source gases; 5 sccm source gas flow.

considerations in the next paragraph.

Further studies of the microstructural evolution by RTSE reveal that the smoothening effect during coalescence is the same for a-SiC:H alloys prepared with R=20 and substrate temperatures ranging from 150°C to 250°C. As a result, the correlation between good electronic properties and extensive smoothening during microstructural coalescence as discussed in Sec. 1.1 remains valid (Li et al., 1992; Collins et al., 1994b). In fact no exception to this correlation has been found in variations of substrate temperature, plasma power, H_2-dilution, C-incorporation, and even deposition process (sputtering vs. PECVD). The combined observations of this paragraph and the previous one suggest that there are two types of void structures in amorphous semiconductors: one type forms upon incomplete coalescence, is columnar in nature and electrically detrimental, and the second type occurs even in completely coalescing films, is point-like in nature and electrically benign (Lu et al., 1994).

As a final point, an inspection of the data in Fig. 6(a)-(b) suggests that, although the initial state properties of the a-SiC:H prepared at 180°C with R=20 may be somewhat improved over those for a-SiC:H prepared at 250°C, the properties in the light-soaked state are essentially the same.

1.3 *Post-Hydrogenation of a-SiC:H*

In previous studies, we have shown that a-Si:H can be post-hydrogenated in-situ at a temperature of 250°C, generating the atomic H using a heated filament (Collins et al., 1992). This approach was motivated by a number of considerations: (i) in-situ H-treatments may have beneficial effects on bulk layer and device interface properties, (ii) the filament H-treatment avoids direct plasma exposure of the surface, and the H impinges on the surface at thermal energies, (iii) the filament is a very effective way of generating atomic H as demonstrated in the diamond film growth field, and most importantly (iv) the method can be used in conjunction with conventional parallel-plate PECVD device fabrication for modification of interfaces.

In intrinsic a-Si:H films, a significant additional amount of H, typically ~5 at.% bonded in monohydride configurations, can be incorporated in the top ~200 Å of the film in a 30 min. filament H-treatment (Collins et al., 1992). By alternating growth and H-treatment to achieve a uniformly elevated H-content, one can prepare films exhibiting minor improvements in the subgap absorption and stability compared to control films prepared without the H-treatments. An assessment of all the results obtained to date on this subject, however, suggests that the H-treatments reduce the run-to-run variability in film quality that exists for control samples. As a result, the routine H-treated films exhibit very similar electronic characteristics as the best control films. This suggests that some of the excess H is in fact passivating defects and impurities that exist under less-than-optimum growth or vacuum conditions; the remainder of the H is paired in configurations that are stable and inert, and serve to increase the optical gap of the material.

We report here our initial attempts at performing similar experiments on a-SiC:H. There are two motivating reasons for extending this study. (i) The potential for improvement of the bulk properties of the alloys is greater. (ii) We are interested in H-treating the p/i heterojunction interface in the solar cell configuration, and therefore need to understand better the effect of atomic H on a-SiC:H:B.

Figure 7 shows the evolution of the additional Si-H volume fraction averaged over the top ~200 Å of a thick a-Si:H film, obtained during a weak 1 hr filament-generated H-treatment (An et al., 1993). Because the detection mode here is RTSE, we are sensitive to the conversion of Si-Si bonding units to Si-H units, due to the different spectral dependences of their polarizabilities. We are not sensitive to the incorporation of unbonded H or to the replacement of existing H in Si-H units. The final saturation value in Fig. 7 corresponds to an additional H-content of about 4 at.%. Corresponding results for the exposure of a-$Si_{1-x}C_x$:H (with R=0; x≈0.09) to filament-generated H under identical conditions are also provided in Fig. 7. For both a-Si:H and a-SiC:H samples, the substrate was maintained at 250°C during film growth, and the sample was maintained between 240 and 250°C during the H-exposure process.

It is clear that there is little change in the optical response of the a-SiC:H with H-treatment, compared with that of a-Si:H. There are at least two possibilities to explain the difference between the results for a-Si:H and a-SiC:H. The first possibility is that H-diffusion into the a-SiC:H may be blocked. It has been proposed that the diffusion of H in unalloyed a-Si:H progresses through Si-Si bond insertion, and the Si-O bonds on air-exposed surfaces have been observed to block thermal H-penetration into the bulk (An et al., 1993). A similar diffusion barrier effect can develop for the alloys if, upon H-exposure, the sample surface develops sufficient Si-C and C-H bonds that are stronger than the Si-Si bonds. A second possibility is that the H penetrates the a-SiC:H via the Si-Si bonds or void structure, but once there does not effect a change in bonding. Because the a-SiC:H already contains ~20-25 at.% H (as opposed to the 8 at.% in the a-Si:H), its network may already be relaxed and further Si-Si bond breaking may not be energetically favorable.

Recent ex situ secondary ion mass spectrometry (SIMS) studies show that the latter model is the correct one. Figure 8(a) presents deuterium (D), hydrogen (H), and H+D SIMS profiles for a-SiC:H (R=0) exposed to atomic D at 240-250°C under the same conditions as in the optical experiment of Fig. 7. What appears to be happening here is that free D is exchanging with the H at existing bonding sites in the material. The freed H leaves the network, and the net effect is a nearly constant H+D concentration profile. There appears to be a slight increase in H+D concentration in the top 200 Å of the film, but given the uncertainties of SIMS, we cannot

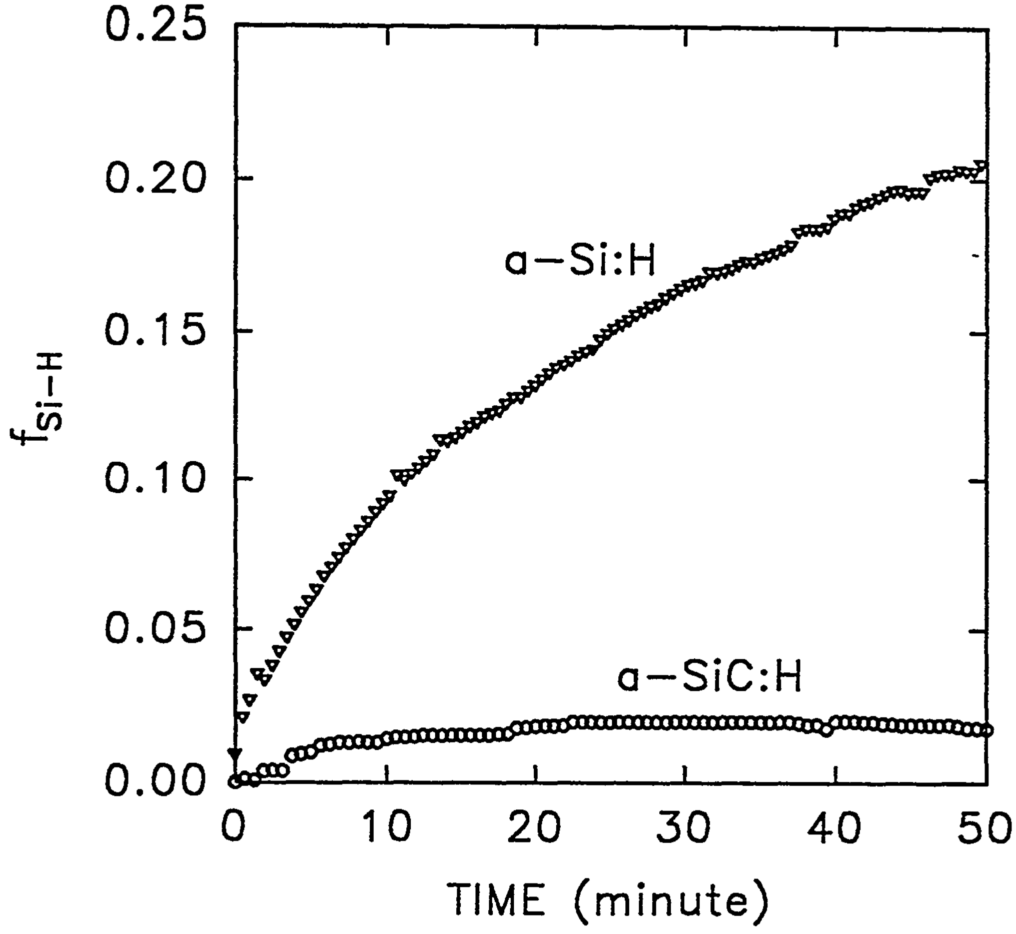

Figure 7. Evolution of Si-H component volume fraction in the top 200 Å of a-Si:H and a-SiC:H (R=0) during exposure of opaque films to atomic hydrogen generated by a heated filament. The sample was maintained at 250°C during growth and between 240 and 250°C during the H-exposure process.

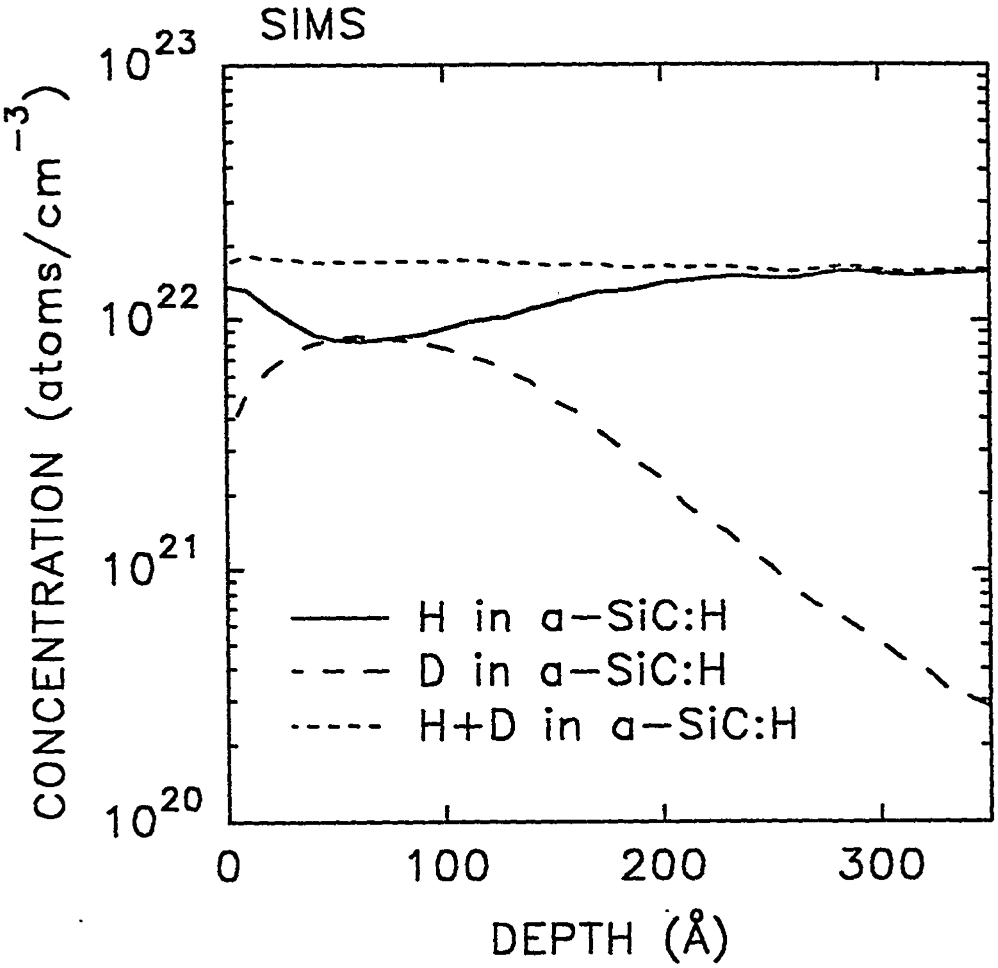

Figure 8(a). Secondary ion mass spectrometry profiles of hydrogen (H) and deuterium (D), and H+D concentrations in an a-SiC:H film (R=0) exposed to atomic D for 60 min. at 240-250°C. After the exposure, the a-SiC:H was capped by material prepared under the same conditions for protection against the ambient.

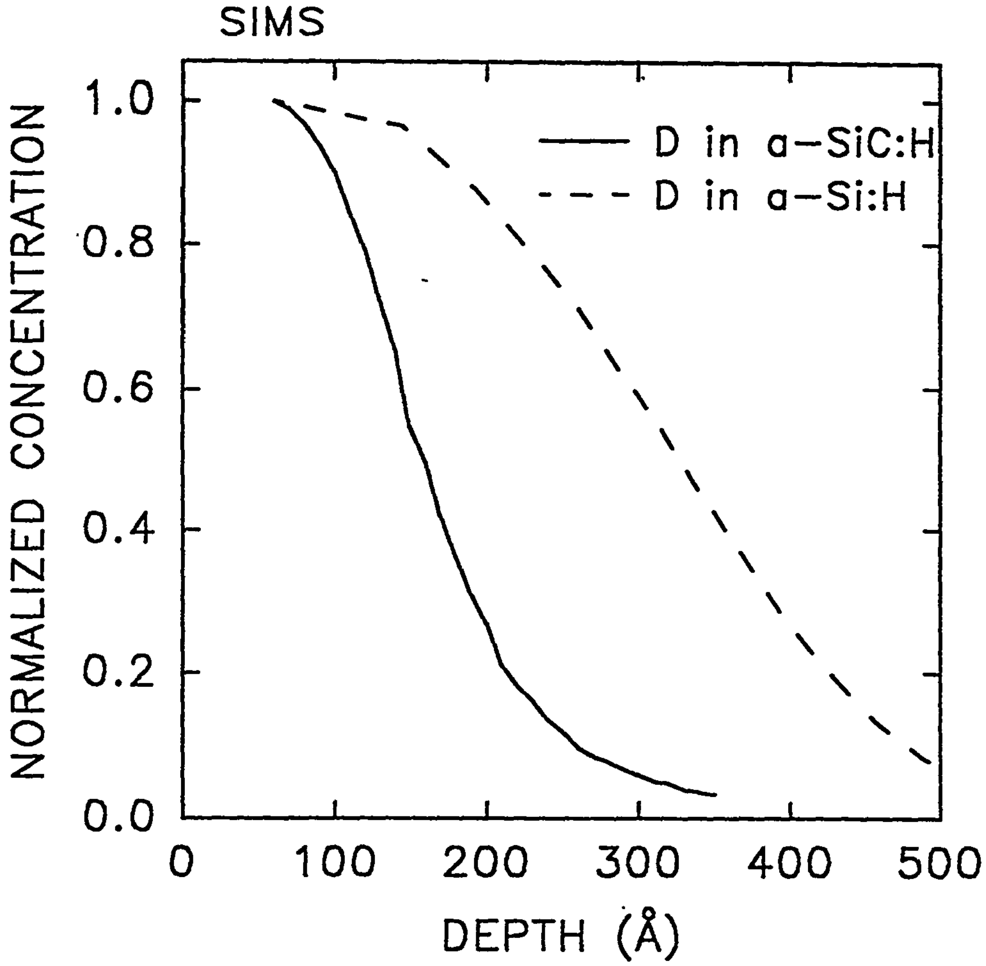

Figure 8(b). Normalized SIMS profiles comparing the penetration of D in a-SiC:H, reproduced from Fig. 8(a), with the corresponding results for a-Si:H obtained earlier under similar H-exposure conditions. The higher void volume fraction and bonded H-content in the initial a-SiC:H film suggests that the more effective H-transport in the a-Si:H does not occur through voids, but rather through Si-Si bonds.

interpret this as being meaningful. In Figure 8(b), we compare the D diffusion profile for a-SiC:H, reproduced from Fig. 8(a) with the corresponding result for a-Si:H, exposed to D under similar conditions. The penetration depth of D in the a-SiC:H is a factor of about 2 lower than that in a-Si:H (150 Å vs. 300 Å). Because of the much higher void volume fraction and H content in the a-SiC:H with R=0 compared to a-Si:H, this result suggests that the D diffuses predominantly through the Si-Si bond network, rather than through the void structure or through the Si-H bonds.

Because H *does* penetrate the a-SiC:H network as shown by the SIMS D profile, it is possible that it induces electronic changes that cannot be detected at the macroscopic level of RTSE. In order to assess this possibility, it is necessary to prepare thick a-SiC:H by alternating growth and H-exposure, as has been done for a-Si:H. Studies along this line, intended to improve bulk alloy properties and stability, are now in progress. Further H-treatment approaches, that have been undertaken to improve solar cell interfaces are described in in Sec. 2.2.

A final point of discussion involves a comparison between the results in Fig. 7 for a-Si:H and a-SiC:H. As noted above, the comparison seems to suggest that the role of the additional H is to break Si-Si bonds, and in the process relax strain in the Si-Si bonding network. In contrast, the a-SiC:H network with its higher void volume fraction and bonded H-content appears to be sufficiently relaxed so that no further bonds are broken by the diffusing H. In addition the smaller number of Si-C bonds may also help to stabilize the network. In spite of these observations, it is found that the alloys typically exhibit at least as high a saturated light-induced defect concentration than unalloyed films, but often higher. Thus, the light induced defect density and ultimate stability of the a-Si:H and a-SiC:H materials show little correlation with macroscopic sample processes that strongly vary the sample properties. The results of Fig. 7, and those obtained earlier for the H-relaxation of a-Si:H, lead to questions as to whether the "*weak* Si-Si bond" is the site for the light-induced defect (Stutzmann et al., 1985).

In fact, we do believe that the diffusing H in a-Si:H does preferentially break and passivate the strained and weak Si-Si bonds, thus relaxing the network, however, this has little effect on the electronic stability. When the atomic H concentration in the near-surface is increased above a critical level, the structure relaxes into the lowest energy crystalline state (see Sec.5.3).

1.4 *Final Comments on Preparation Parameter Variations for a-SiC:H*

In spite of the improvements achieved through H_2-dilution of the source gases, the improved a-SiC:H retains the poor stability typical of these alloys. In fact some of the improvement gained through optimized preparation is lost upon light-soaking to saturation, as has been described in

Phase II of this project (Collins et al., 1994a). As noted by von Roedern, the range of electronic properties obtained through variation of H_2-dilution is smaller than the range obtained by light soaking the optimum material (von Roedern, 1993). Because the microstructural properties of the film (e.g., void and H content) do not change with light-soaking, this tends to suggest that it is the electronic state that is the most important, with a slight modulation of that state provided by the microstructure.

One primary conclusion is that we have not been successful at solving the stability problem with the use of a-SiC:H, and in fact may have exacerbated the problem somewhat by adopting this system. One key point is that the band gap widening achieved with this alloy system is attributable more to the excess H that is incorporated, rather than the C. It may be that certain Si-H (and/or C-H) bonding configurations are detrimental to stability. Thus, we intend to remain open in looking at other alloy systems, for example involving N, in which the gap shift is achieved through different means.

2. P-Type Doped a-Si:H and a-SiC:H Thin Films

In the study to be described next, the goal was to establish the doping conditions for a-SiC:H p-layers. Such layers must be incorporated into baseline a-Si:H solar cells fabricated in our single-chamber research system (see Sec. 6.1). Our previous studies have hinted at the reduction of the doping efficiency with increasing void volume fraction in a-SiC:H films (Chen and Wronski, 1993). In particular, higher conductivity films are prepared nearer the upper end of the substrate temperature scale, 250°C [see Fig. 3(b)], where the void volume fraction begins to saturate. (Higher temperatures lead to unacceptably high TCO reduction.)

Thus, our approach in the doping studies was to use conditions chosen to lead to a low void density in the film as determined from Secs. 1.2.1-1.2.4, while maintaining sufficiently low H_2-dilution conditions again to minimize TCO modification. Some H_2 in the gas mixture is inevitable ($0.1 \leq R \leq 1$), however, since H_2 is the diborane carrier gas in our case. [This carrier gas was chosen in order to avoid cylinder/line CVD -- and flowmeter clogging -- that occurs with SiH_4 as the carrier gas (Collins, 1988).] The low level of dilution used in p-type a-SiC:H deposition ($0.1 \leq R \leq 1$) avoids detectable reduction of the SnO_2 transparent conducting oxide (TCO) used in baseline cell preparation (see Sec. 3.1). It appears that the H_2 dilution level can be increased when ZnO TCO is employed (see Sec. 4.2). This may be another direction that can be pursued in an attempt to increase the doping efficiency further, however, such an effect has yet to be demonstrated.

In spite of the well-known CVD problems associated with diborane use, our real-time optical studies were undertaken with this dopant source since diborane has been used routinely over the past several years in baseline a-Si:H-based midgap cell development in the multichamber system at Penn State. At this time, we are currently switching both research and solar cell operations to trimethyl boron (TMB) as the p-type layer gas supply. We expect to compare the results of this section and those of successive sections, obtained with the diborane dopant source, with the corresponding results obtained in the future with TMB. Of particular interest is a comparison of the decomposition rates of the gases on a-SiC:H:B surfaces.

2.1 *P-Type Doped a-Si:H and a-SiC:H Preparation*

Figure 9 shows selected properties of thick (0.3-0.8 µm) p-type a-SiC:H and a-Si:H prepared as a function of gas phase doping in our research system. The gas phase doping here is defined as a ratio of the gas flows by: $[B_2H_6]/\{[CH_4]+[SiH_4]\}$. Because the B_2H_6 gas was diluted to 1% in H_2, R increased from 0 to 1 with increasing gas phase doping level over the range of Fig. 9. All other preparation parameters were held constant for this series of samples. The substrate temperature was 250°C; the total gas pressure was 0.17 Torr; the plasma power was 3 W (78 mW/cm^2); and the total source gas (SiH_4 or CH_4+SiH_4) flow was 10 sccm. The properties plotted in Fig. 9 include: E_{04}, the energy at which $\alpha=10^4$ cm^{-1}; E_g, the room temperature Tauc gap; E_σ the dark conductivity activation energy; and σ_{RT}, the room temperature conductivity. Selected data for these samples along with their preparation conditions are also tabulated numerically in Table I.

Of significant interest in Fig. 9 are the changes in optical gap and activation energy. For both the a-SiC:H and the a-Si:H, the optical band-gap shows its characteristic decrease as a function of doping level. In fact the decrease between 0 and 1% doping level for a-SiC:H, 0.26 eV, is even larger than that for unalloyed a-Si:H, 0.20 eV. In order to avoid such large decreases in the gap and maintain the largest spread between the gap and the activation energy (1.37 eV), we choose a moderate doping ratio of 0.1%. Such (activation/gap) energy characteristics are also obtained in our multichamber system, and were employed for the Penn State baseline cell of Sec. 6.2.

2.2 *Hydrogenation of P-Type Doped a-Si:H*

We have also studied the possibility of widening the p-type a-Si:H:B and a-SiC:H:B optical gaps through in-situ atomic hydrogen treatment of the p-layer as described in Sec. 1.3. If this process is successful, it would be very convenient to apply to the cell preparation process. The p-layer is usually deposited to a thickness of ~200 Å, and this is the approximate penetration depth of the H achieved in a single treatment of ~30 minutes.

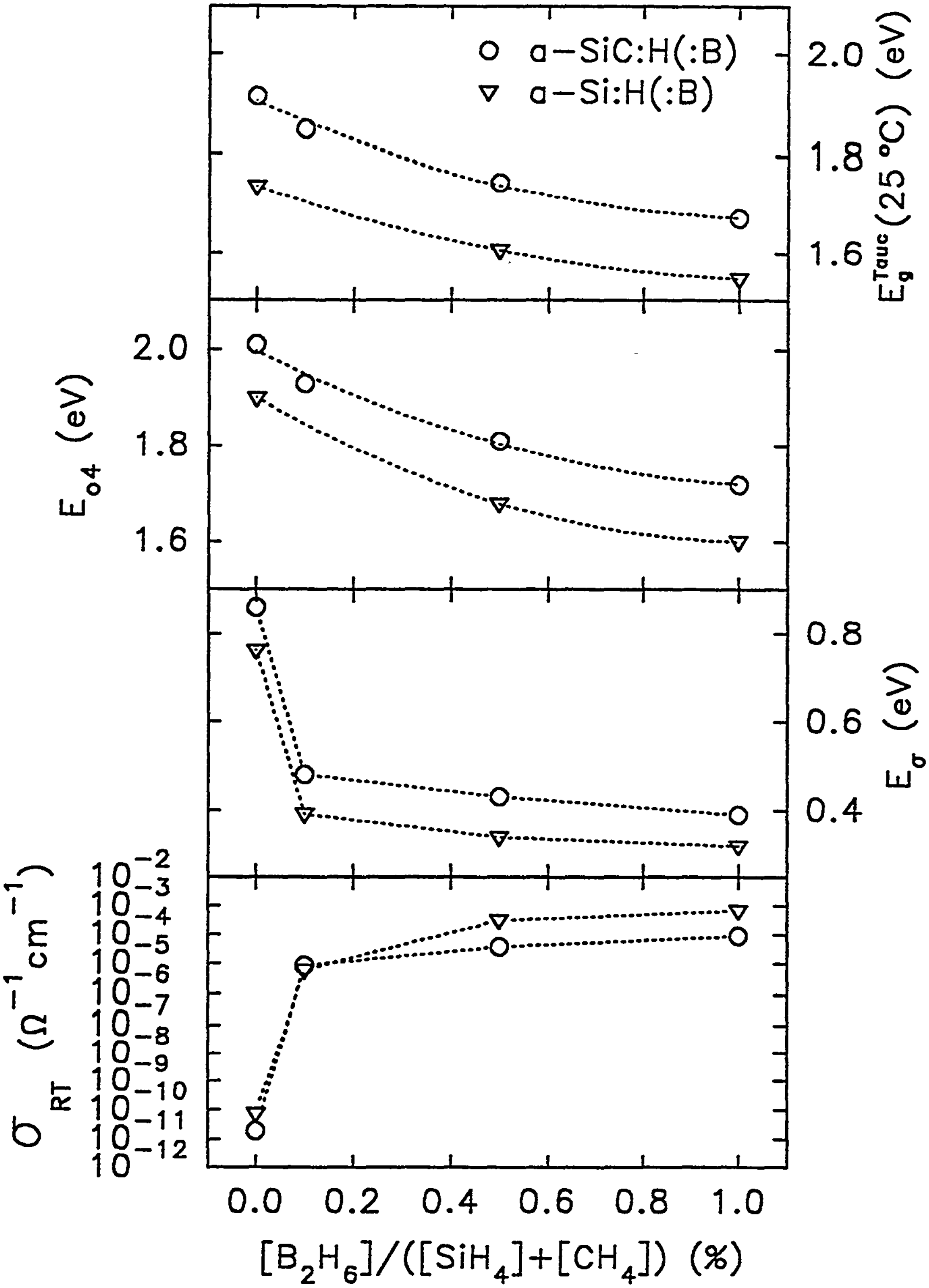

Figure 9. Tauc Gap, E_{04}, E_σ, and σ_{RT} versus p-type gas phase doping for selected a-Si:H:B and a-SiC:H:B samples. The gas phase doping is defined as a ratio of the gas flows by: $[B_2H_6]/\{[CH_4]+[SiH_4]\}$. Because the B_2H_6 was diluted to 1% in H_2, and because no excess H_2 dilution was used here, the 0.1% and 1% doping levels correspond to R=0.1 and R=1, respectively. The substrate temperature was 250°C; the total gas pressure was 0.17 Torr; the plasma power was 3 W (78 mW/cm^2); and the total CH_4+SiH_4 flow was 10 sccm.

TABLE I

SAMPLE	$[B_2H_6]/([SiH_4]+[CH_4])$	$E_g^{Tauc}(25^oC)$ (eV)	E_{04} (eV)	E_σ (eV)	σ_{RT} ($\Omega^{-1}cm^{-1}$)
a-SiC:H	0.000	1.912	2.01	0.86	1.90E-11
a-SiC:H:B	0.001	1.846	1.93	0.48	8.56E-6
a-SiC:H:B	0.005	1.747	1.81	0.43	3.76E-5
a-SiC:H:B	0.010	1.674	1.72	0.39	9.11E-5
a-Si:H	0.000	1.74	1.90	0.76	7.25E-11
a-Si:H:B	0.001			0.39	5.98E-6
a-Si:H:B	0.005	1.606	1.68	0.34	3.12E-4
a-Si:H:B	0.010	1.546	1.60	0.32	6.83E-4

Table I. The data for the p-type a-SiC:H and a-Si:H samples of Fig. 9 presented in tabular form. E_g is the room temperature Tauc gap, E_{04} is the energy at which $\alpha=10^4$ cm^{-1}, E_σ is the dark conductivity activation energy, and σ_{RT} is the room temperature conductivity.

Figure 10 shows the evolution of the ellipsometric parameter ψ at 3.0 eV for 0.1%-doped a-Si:H:B and a-SiC:H:B during exposure at 250°C to atomic H. The preparation conditions for the p-type layers were the same as those used in Fig. 9. The magnitude of the change in ψ provides an estimate of the degree of Si-Si bond-breaking by H-incorporation. The results show that the effect of the H-treatment on the optical properties of the a-SiC:H alloy film is very weak in comparison with that of the unalloyed film. The same conclusion was reached in studies of undoped films, as well (see Fig. 7). A comparison of data of Fig. 10 with the raw data from which Fig. 7 was derived reveals that the H-treatment generates a larger change in the doped material optical properties.

In order to demonstrate the magnitude of this effect, the top panel of Figure 11 shows the dielectric functions of the unalloyed p-type a-Si:H:B at the elevated temperature before and after the process of Fig. 10. The lower panel presents the imaginary part of the dielectric function plotted as $\varepsilon_2^{1/2}$ versus energy, in order to obtain a measure of the optical gap (constant dipole matrix element, or Cody, method). The 250°C optical gap for untreated a-Si:H:B is 1.48 eV; correction for the elevated temperature yields a room temperature gap of 1.63 eV; and correction for the difference between Tauc gap (constant momentum matrix element) and the gap from the Cody method (~0.08-0.1 eV) yields a conventional room temperature Tauc gap of 1.72 eV. Figure 11 shows that the gap increases by about 0.2 eV upon H-treatment. This effect is much larger than was achieved in our previous experience with undoped materials. In fact with a predicted room temperature Tauc gap of 1.90 eV, this material actually has a wider optical gap than our as-deposited p-type a-SiC:H. Apparently, the role of the H-treatment of a-Si:H:B is not only to increase the H-content and widen the gap, but also to reduce the extensive band-edge broadening that occurs with B-incorporation.

The next step in this study, currently in progress, is to deposit thin layers of H-treated a-Si:H:B and measure their transport characteristics. The goal is to measure the room temperature conductivity and the Fermi level position of the H-treated material. Our first experiment toward this goal used a 0.1% doping level and revealed an activation energy of 0.39 eV. This value is equivalent to that obtained on thicker doped layers prepared without the H-treatment (see Table I). Thus, in this case, the spread between the optical gap and conductivity activation energy is estimated to be 1.52 eV. If such a large spread between the gap and activation energies is consistently obtained in the H-treated state in future experiments, then the treated a-Si:H:B will be incorporated into solar cells prepared in our multichamber system.

One further point of interest involves the shape of the single wavelength treatment characteristics in Fig. 10. The corresponding characteristics for undoped a-Si:H show a smooth exponential decay in ψ that occurs upon igniting the filament used to generate atomic H in the treatment process. The more complex behavior in Fig. 10, for example the appearance of an

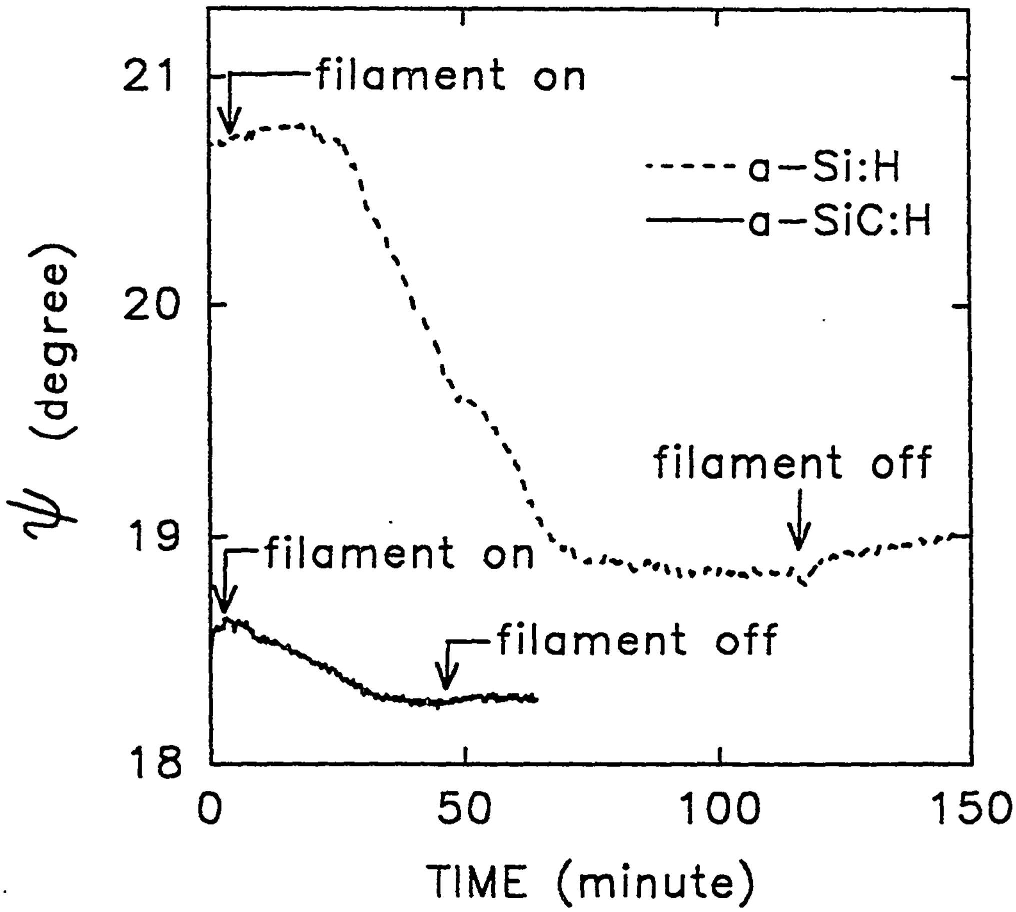

Figure 10. Evolution of the ellipsometric parameter ψ at 3.0 eV for 0.1%-doped a-Si:H:B and a-SiC:H:B during exposure to atomic H. The other sample preparation conditions were the same as those used in Fig. 9. The data collected after extinguishing the filament provide information on the kinetics of H detrapping (see Fig. 12).

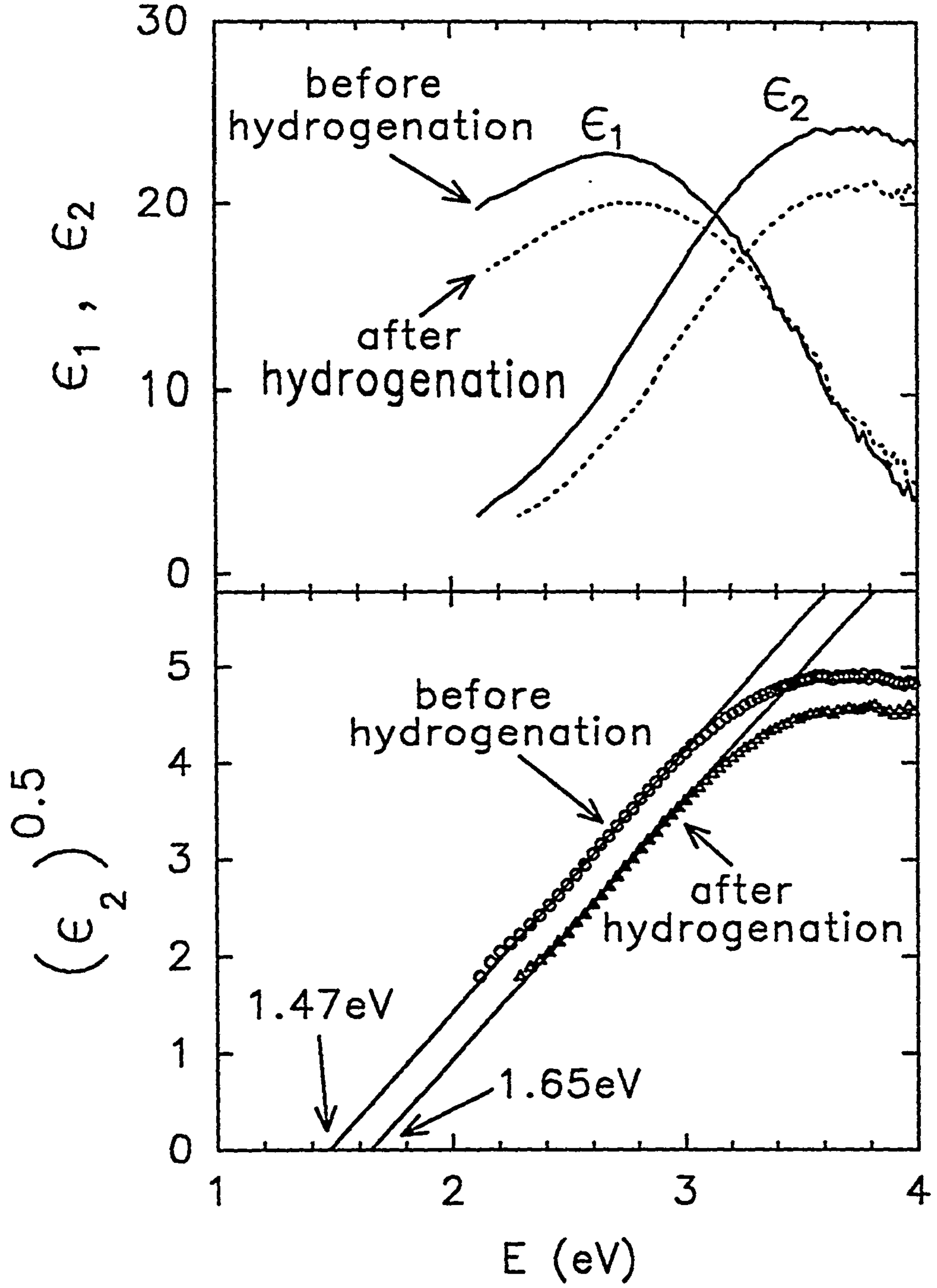

Figure 11. Dielectric function (top) and optical gap determination via the $\varepsilon_2^{1/2}$ extrapolation method (bottom) for 0.1%-doped a-Si:H:B, obtained before and after a 2 hr exposure to atomic hydrogen generated by a hot filament. The other sample preparation conditions were the same as those used in Fig. 9. The filament conditions were maintained below the threshold for etching. The effects of substrate temperature (250°C) and gap extrapolation lead to a 0.25 eV narrower gap in (b) than the room temperature Tauc gap. Thus, the room temperature Tauc gap of the H-exposed a-Si:H:B material is expected to be ~1.9 eV.

initial increase in ψ for the a-Si:H:B, occurs when atomic H etches the chamber walls of chemisorbed Si-B species that form via the CVD process (Collins, 1988). This leads to the development of several monolayers of the material on the a-Si:H:B and a-SiC:H:B surfaces. These results show that any in-situ H-treatment of the p-layer during solar cell preparation in our multichamber system must be done after the substrate/p-layer has been transferred to the i-layer growth chamber.

A final point on the H-treatment of a-Si:H:B relates to the stability of the incorporated H that is responsible for the band gap increase. Figure 12 shows the evolution of the relative Si-Si bond volume fraction for 0.1%-doped a-Si:H:B, obtained upon extinguishing the filament used for atomic H exposure. The sample was held at 250°C throughout the measurement process. These results have been obtained from an analysis of the longer time data in Fig. 10, in order to highlight the detrapping of H atoms that leads to Si-Si bond re-formation (An et al., 1993). Data were also collected 42.5 hrs later in an attempt to characterize the stability of the remaining H. The solid line is a fit to the data utilizing three reaction rates. About 6% and 35% of the initial incorporated H detrap at rates of 1.3×10^{-2} s^{-1} and 1.6×10^{-4} s^{-1}, respectively. The 6% H will probably detrap before the sample can be cooled sufficiently, and is thus unstable. The remaining 59% detraps at a rate $< 2.2\times10^{-6}$ s^{-1} and is highly stable. If we assume an attempt frequency of 10^{12} to 10^{13} s^{-1}, the three observed rates correspond to activation energies of (1.49±0.05) eV, (1.68±0.05) eV, and (1.88±0.06) eV, respectively.

3. Interfaces between SnO_2 and P-Type a-SiC:H

In Phase II, we described the effects of PECVD growth of intrinsic a-SiC:H layers on SnO_2 (Collins et al., 1994a). Two main points were noted.

First, we were able to quantify the free Sn that forms at the interface as a result of the reduction of the TCO. The H_2 dilution ratio and substrate temperature were found to be key parameters that control the degree of SnO_2 reduction and the amount of free metal generated at the interface. In Figure 13, we review this information and add new results. Here the amount of free metal contamination is plotted in terms of the mass thickness detected by RTSE at the SnO_2/a-SiC:H(:B) interface for films of different H_2 dilution. For the solid points, the a-SiC:H was undoped and the substrate temperature was 250°C. For the open point, the a-SiC:H was undoped but the substrate temperature was 170°C. The open triangles represent new results in which the a-SiC:H was doped using a gas phase diborane mixture of 0.1%. On the basis of the results in Fig. 13, we suggest that the presence of doping levels of diborane in the gas phase do not exert a significant influence on SnO_2 reduction characterized by free metal formation. Thus, we can view the full range of results in Fig. 13 as being appropriate for doped and undoped

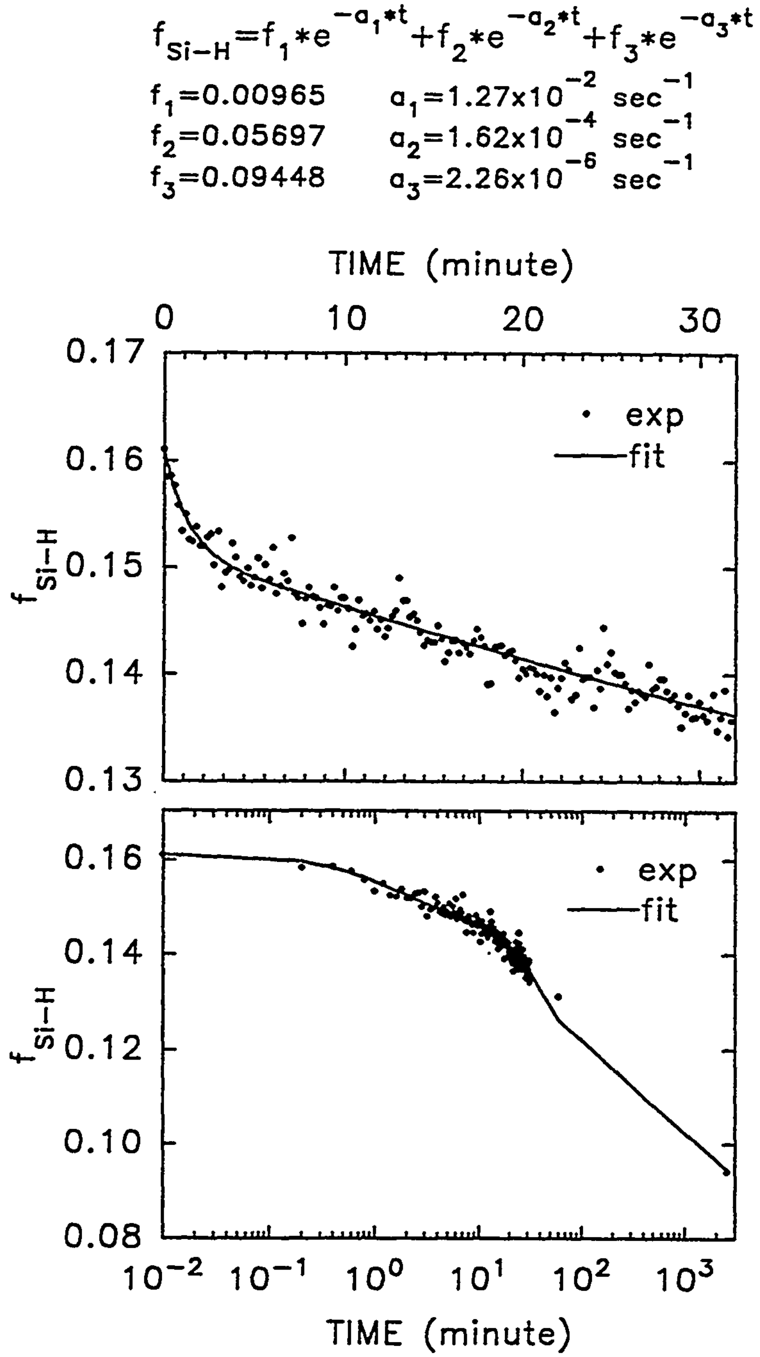

Figure 12. Evolution of the Si-Si bond volume fraction for 0.1%-doped a-Si:H:B obtained after extinguishing the filament used for atomic H exposure. These results have been extracted in an analysis of the longer time data in Fig. 10, in order to highlight the detrapping of the H atoms that are incorporated during the H-exposure and the re-formation of Si-Si bonds. Data were also collected 42.5 hrs later in an attempt to characterize the stability of the remaining H. The solid line is a fit to the data utilizing three reaction rates. About 6% and 35% of the initial incorporated H detrap at rates of 1.3×10^{-2} s^{-1} and 1.6×10^{-4} s^{-1}, respectively. The former H will probably detrap before the sample can be cooled and so will not be stable. The remaining 59% detraps at a rate < 2.2×10^{-6} s^{-1} and is highly stable. If we assume an attempt frequency of 10^{12} to 10^{13} s^{-1}, these rates correspond to activation energies of (1.49±0.05) eV, (1.68±0.05) eV, and (1.88±0.06) eV respectively.

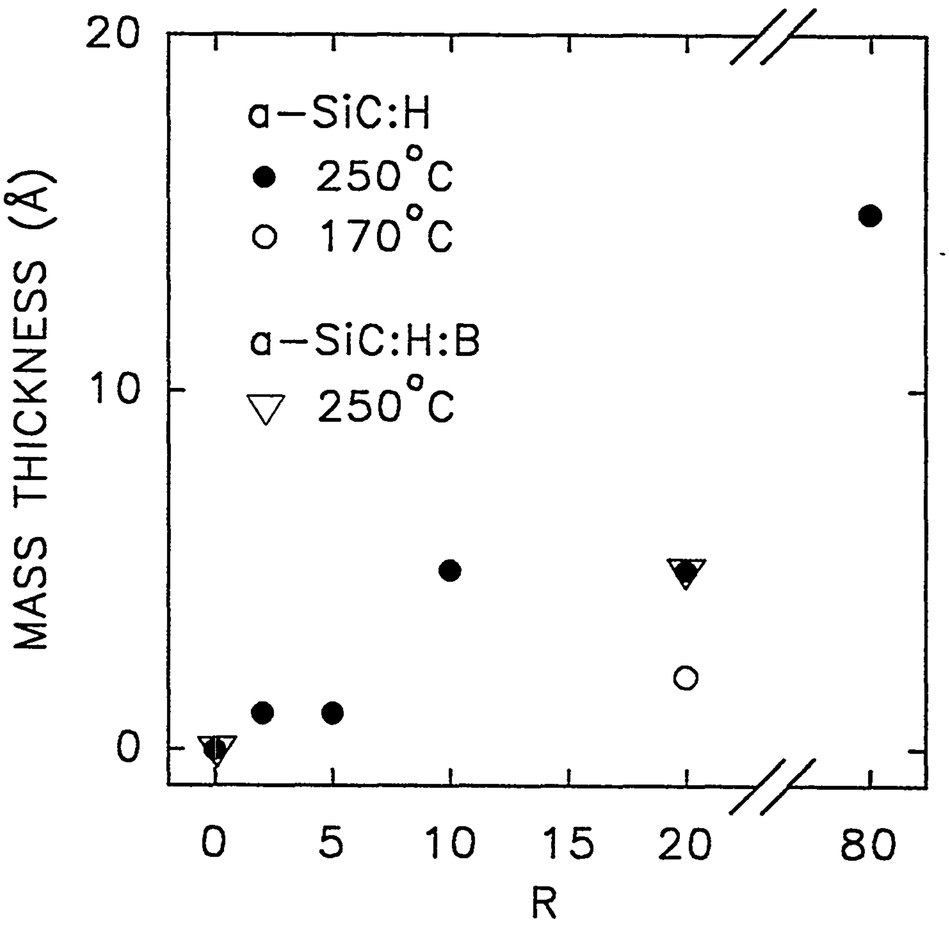

Figure 13. Metal contamination plotted in terms of mass thickness detected by RTSE at the SnO_2/a-SiC:H(:B) interface for films of different H_2 dilution ratio R. For the solid points, the a-SiC:H was undoped and the substrate temperature was 250°C. For the open circle, the a-SiC:H was undoped but the substrate temperature was 170°C. For the open triangles, the a-SiC:H was doped using a gas phase diborane mixture at 0.1%.

materials.

As the second point noted in Phase II, the free Sn at the SnO_2/a-SiC:H interface was found to diffuse away from the interface on a time scale of many days. It was suggested that the Sn diffuses into the amorphous semiconductor, rather than being reabsorbed into the TCO. It was further suggested that *this is a possible irreversible solar cell degradation mechanism.* Additional measurements are planned with a chemically-specific probe, e.g., SIMS, Auger electron spectroscopy or uv photoelectron spectroscopy, in order to test these suggestions further.

The observed SnO_2/p-layer interface effects discussed in detail in this section are also included in the summary of Table VI, presented below.

3.1 *Role of Hydrogen in the Reduction of SnO_2*

In order to understand better the changes that the SnO_2 surface undergoes when a-SiC:H is deposited onto it, we first studied the morphology of a film surface exposed to atomic H. In particular, scanning electron microscopy (SEM) was performed on solar cell-grade specular SnO_2 exposed to filament-generated atomic H for 45 minutes. Such an procedure induces the same optical change as does a brief direct H_2 plasma exposure. Electron micrographs suggest that the film develops metallic clusters. In this process, it appears that regions of SnO_2 in the neighborhood of grain boundaries are etched away leaving free metal atoms that form clusters.

Electrical measurements of SnO_2/a-SiC:H(:B) interfaces provide further support for this conclusion. Table II includes the coplanar resistivity (in Ω cm) of 700 Å SnO_2 before and after being over-deposited with undoped and 0.1% gas-phase-doped a-SiC:H films. Three depositions were performed in an attempt to explore the effects of H_2-dilution and doping. The substrate temperature for all three depositons was 250°C. The increase in resistivity of SnO_2 for all depositions is counterintuitive in light of the metallic build-up detected optically. The only possible conclusion is a loss in near-interface continuity of the SnO_2, parallel to the substrate plane. We suspect that this is a direct result of a near-interface columnar morphology that develops in the SnO_2 which is generated by the H-etching process noted above.

One might conclude, on the basis of the numerical results in Table II, that doping and H_2 dilution both play important roles in the generation of this type of microstructure, and when combined have a multiplicative effect. However, such a conclusion would be inconsistent with the results of Fig. 13, which shows that the B interaction at the SnO_2 surface plays no role in additional metal formation. It is possible that B-diffusion in the near surface of SnO_2 serves to compensate n-type dopants in the TCO and reduce its conductivity. Such an effect would be observed electrically, but not optically.

TABLE II

SAMPLE	BEFORE (Ωcm)	a-SiC:H (R=20)	a-SiC:H:B (R=0.1)	a-SiC:H:B (R=20)
ZnO	9.46×10^{-4}	7.55×10^{-4}	6.99×10^{-4}	6.56×10^{-4}
SnO_2	7.60×10^{-3}	1.43×10^{-2}	1.43×10^{-2}	5.14×10^{-2}

Table II. Tabular information on coplanar resistivity of 1000 Å ZnO and 700 Å SnO_2 TCO's before and after the deposition of undoped and 0.1% gas-phase-doped a-SiC:H films. Three depositions on each TCO substrate were performed in order to explore the effects of H_2-dilution and doping. The substrate temperature in all cases was 250°C. The increase in resistivity for SnO_2 suggests a decrease in near-surface continuity. The decrease in resistivity for ZnO suggests an increase in the carrier concentration in the near surface region.

Here we have suggested that the grain boundary regions are preferentially attacked to yield free Sn which is sufficiently mobile at these temperatures to aggregate on the film surface. Such a mechanism would suggest that textured SnO_2 with its larger grain size will be less susceptible to attack and reduction by atomic hydrogen. In addition to the detrimental presence of free Sn, the columnar type of morphology generated at the interface is expected to lead to a patchy junction in which the current is channeled through the columns. It is possible that this could lead to filamentary shorts in the solar cell. Again, the best way to minimize these problems is by forming the interface with minimum H in the plasma and at a substrate temperature as low as possible. As noted above, both of these effects result in a high void volume fraction in the doped layer and possible reductions in the doping efficiency. The ultimate solution to this trade-off may be to switch to ZnO (or ZnO-coated SnO_2) which is more stable (see Sec. 4).

3.2 *B-contamination at the SnO_2/a-SiC:H Interface*

Another approach applied to assess the potential role of B as a contaminant (in addition to free metal) at the SnO_2/a-SiC:H interface is to expose the TCO surface to the gas mixture used in the preparation of the p-type material. If the diborane were to chemisorb strongly on the SnO_2 surface, then the surface would be subsequently activated for thermal CVD of SiH_4 (Collins, 1988). The chemisorption and thermal CVD can be readily detected by RTSE. The chemisorption/CVD process is a possible way for the SnO_2 surface to become heavily contaminated with B in the typical ~1 min. duration between bringing the p-type gas mixture into the chamber and striking the plasma to form the p-layer.

Figure 14 depicts the evolution of the SE data in real time during exposure of the SnO_2 surface to the p-type gas mixture consisting of 6 sccm of SiH_4, 4 sccm of CH_4, and 10 sccm of B_2H_6 @ 1% in H_2. This mixture yields a gas phase doping level of 1%, intended to enhance the chemisorption. The substrate temperature was 250°C and the pressure was 0.2 Torr. The spectra in Fig. 14 reveal gradual changes over the time scale of exposure of 3 hr, consistent with contamination of the SnO_2 surface with a-Si:B CVD material generated during exposure to the gas mixture used to prepare p-type a-SiC:H:B. However, the changes are very small compared to those that occur upon SnO_2 reduction. The changes are also small compared to those that occur during in-situ exposure of clean a-SiC:H:B to this gas mixture.

Figure 15 shows a (ψ, Δ) trajectory at 2.52 eV extracted from the full data set of Fig. 14. The solid line is a model for the development of the chemisorbed material, assuming it is CVD a-SiB:H. In such thin layers, it is difficult to rule out some reduction of the TCO, as well. In any case, this model yields a final thickness of ~5 Å and an average growth rate of ~0.03 Å/minute. Thus, after 1 min. the layer covers about 1/100 of the SnO_2 surface, and we can conclude that this

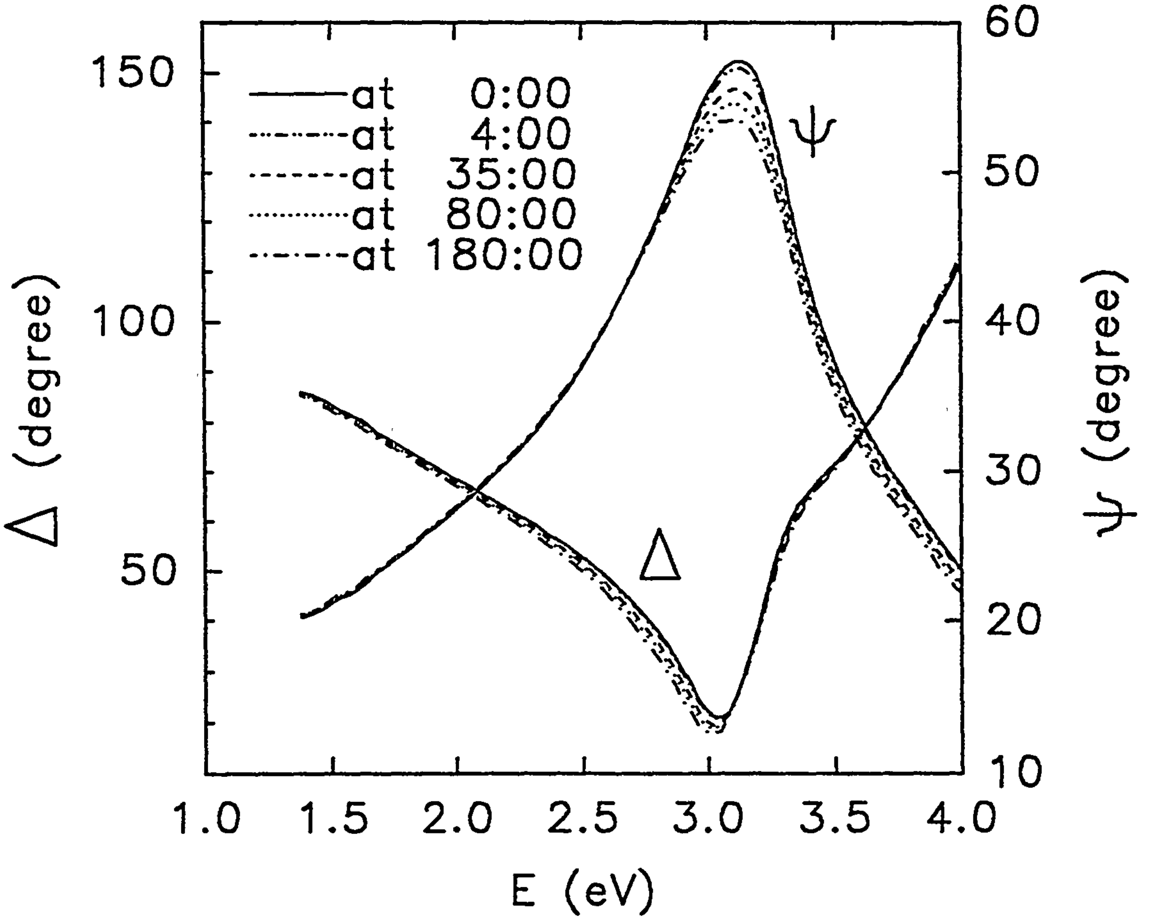

Figure 14. Evolution of the full ellipsometric spectra collected during a 180 minute exposure of a SnO_2 surface to the gas mixture used to prepare p-type a-SiC:H:B. The values in the figure denote the exposure time in minutes for each pair of spectra. The gradual change results from the contamination of the surface with a-Si:B CVD material. The gas phase doping level was set at 1% in this experiment.

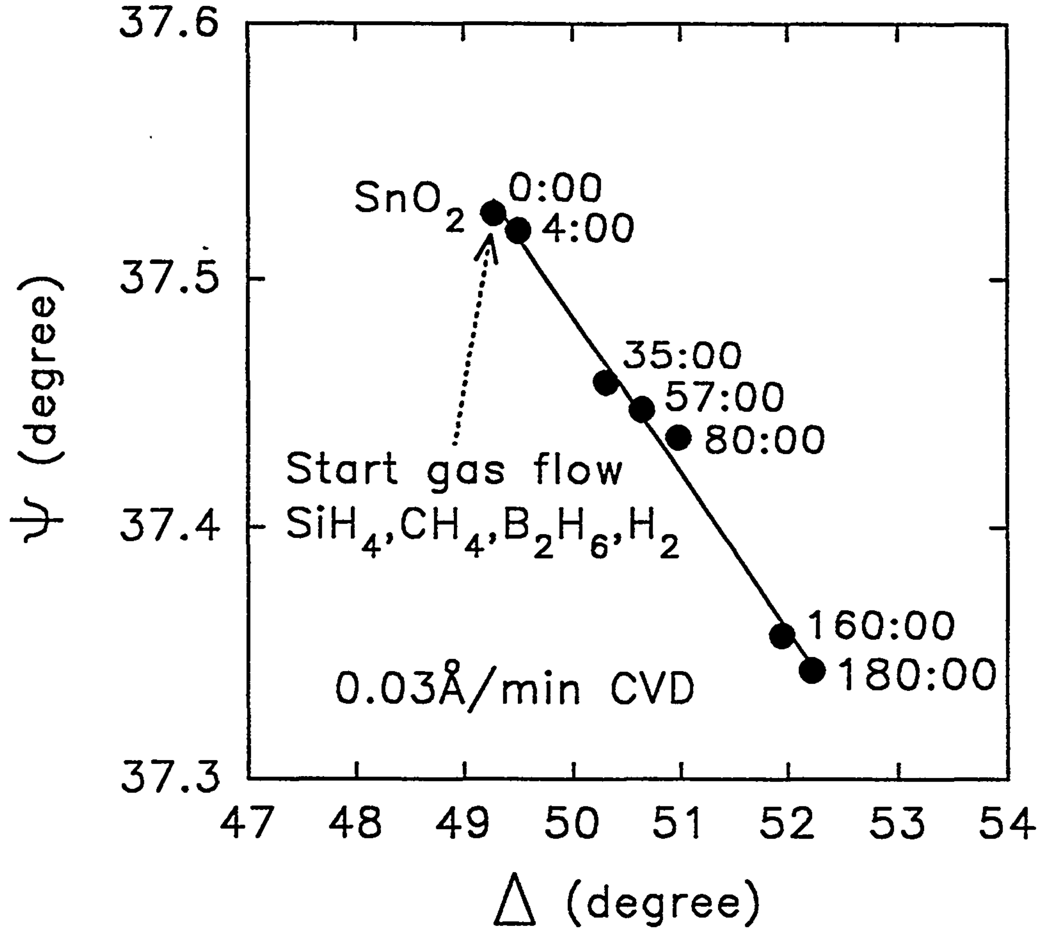

Figure 15. The (ψ, Δ) trajectory at 2.52 eV extracted from the full data set of Fig. 14, collected during a 180 minute exposure of a SnO_2 surface to the gas mixture used to prepare p-type a-SiC:H:B. The solid line is a model for the growth of the CVD a-Si:B thin film material. This analysis yields a final thickness of ~5 Å and an average growth rate of 0.03 Å/minute.

contamination mechanism is of little consequence. This is consistent with the results of Fig. 13 showing that the addition of B_2H_6 to the gas phase has little effect on the interfacial metal content. If excess B were being generated at the interface and not included separately in the optical model, it would be misinterpreted as metallic contamination because of its strong absorption and lead to an enhancement in the detected metal mass; obviously this is not happening.

4. ZnO and ZnO/a-SiC:H(:B) Interfaces

At present, SnO_2 is the most widely-used TCO in spite of the fact that it can be severely reduced in PECVD environments. Although the reduction problem can be mitigated by p-layer deposition at moderate T_s and little or no H_2-dilution of reactive gases, the SnO_2 prevents one from using certain layers predicted to improve cell quality. These include microcrystalline silicon-carbide p- or high T_s (400°C) i-layers.

Because of the problems with SnO_2, attention has been shifting to doped ZnO as an alternative TCO. In Phase II, it has been reported that ZnO is highly resistant to reduction in H_2-enriched PECVD environments and does not experience the concomitant optical losses that SnO_2 does (Collins et al., 1994). Because of the promise of ZnO, the nature of the interaction (if any) between ZnO and overdeposited PECVD a-Si:H-based alloys is of special interest. Here we extend the RTSE investigation of Phase II concerning interface formation between ZnO and i- and p-type hydrogenated amorphous silicon-carbon (a-SiC:H), presenting new results that provide a clearer picture of the nature of the interfacial interaction. The observed ZnO/p-layer interface effects discussed in detail in this section are included in the summary of Table VI, presented below. Before discussing such effects in detail, some of the characteristics of ZnO will be reviewed

Undoped ZnO thin films can be prepared n-type, with resistivities as low as 10^{-3} Ω cm, as a result of stoichiometry deviations in which Zn interstitials and/or oxygen vacancies act as donors (Jin et al., 1988). By heavily doping ZnO (e.g., with Al, B, Ga or In), the resistivity can be lowered further, without a loss in transparency over the solar spectrum. An increase in carrier concentration in ZnO, whether through an increase in excess Zn or dopant concentration, leads to a widening of the optical gap due to the Burstein-Moss effect (Burstein, 1954; Moss, 1954), moderated by many-body effects on the conduction and valence bands (Berggren and Sernelius; 1981). The former effect dominates, and the optical gap increases from 3.35 eV for nominally-intrinsic, stoichiometric ZnO to ~4.0 eV for ZnO:Al with a carrier concentration of ~$5\text{x}10^{20}$ cm^{-3} (Jin et al., 1988). Because real-time SE can monitor the optical gap of the ZnO upon heating to the deposition temperature and upon interface formation, the technique also provides insights into possible changes in the electrical properties of the ZnO in these processes.

This work will be described in Secs. 4.1 and 4.2.

The ZnO films used in this study were sputtered onto glass and Si substrates in large-area runs from two industry sources. Undoped sets of samples from USSC showed optical gaps of 3.35 eV, comparable with near-stoichiometric, undoped ZnO in the literature. Al-doped sets from Solarex showed optical gaps of 3.75 eV, typical of an Al content of 1 at.% and a free electron concentration of 2.5×10^{20} cm^{-3}. Very thin films (ranging from 280 Å to ~1000 Å thick) were utilized in order to enhance the sensitivity of SE. Analyses of the ZnO dielectric functions using effective medium theory suggest void volume fractions < 5-10 vol.% for all sample sets, when measured relative to 0.3 μm thick films. Thus, in spite of the thinness of the ZnO, our results are believed to be characteristic of thicker films as well.

4.1 *Stability of ZnO*

Prior to studying the interfaces between a-SiC:H and ZnO, it is necessary to pre-anneal the TCO above the deposition temperature in order to stabilize its bulk structure. In this way, we ensure that the TCO does not change during interface formation as a result of annealing at the deposition temperature. If this were to occur, it would greatly complicate analysis of interfacial phenomena. In addition, because the optical gap energy provides information on electron concentration, we can also learn about possible changes in the electrical properties of the ZnO upon annealing.

Figure 16 shows the dielectric functions of an undoped ZnO film before and after a one hour anneal at 320°C under vacuum. The small enhancement of the dielectric response without a shift in the gap can be attributed to densification of the structure without any change in the electron concentration. For comparison, Figure 17 shows the dielectric functions of a doped ZnO sample before and after an identical anneal. In this case, the shift in the optical gap value by 0.08 eV to higher energies can be attributed to an increase in the electron concentration by $\sim1\times10^{20}$ cm^{-3} (Jin et al., 1988). This may be attributed to the generation of additional oxygen vacancies or Zn interstitials, or to an increase in the efficiency of dopant atoms in the network.

4.2 *Interfaces between ZnO and a-SiC:H(:B)*

Before describing the results of our interface studies, we briefly review the experimental conditions. In particular, we emphasize that the full spectroscopic capability of RTSE is a key component that provides detailed insights into interface formation.

Films of a-SiC:H were prepared onto ZnO by PECVD. The plasma power, CH_4/SiH_4 flow ratio, and substrate temperature T_s were fixed at 5 W (0.13 W/cm^2 flux), 2:3, and 250°C,

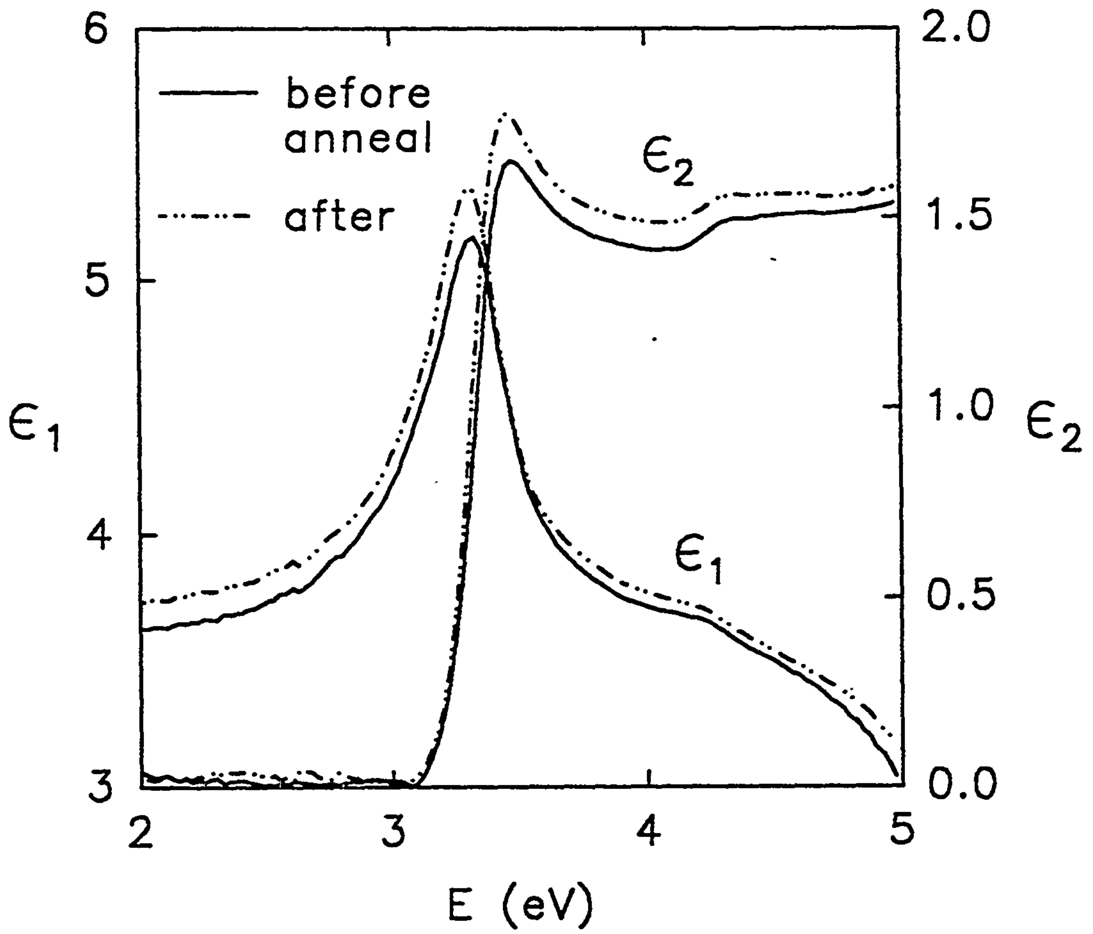

Figure 16. The dielectric functions of an undoped ZnO film before and after a one hour anneal at 320°C under vacuum. The small enhancement of the dielectric response without a shift in the gap can be attributed to densification of the structure without any change in the electron concentration.

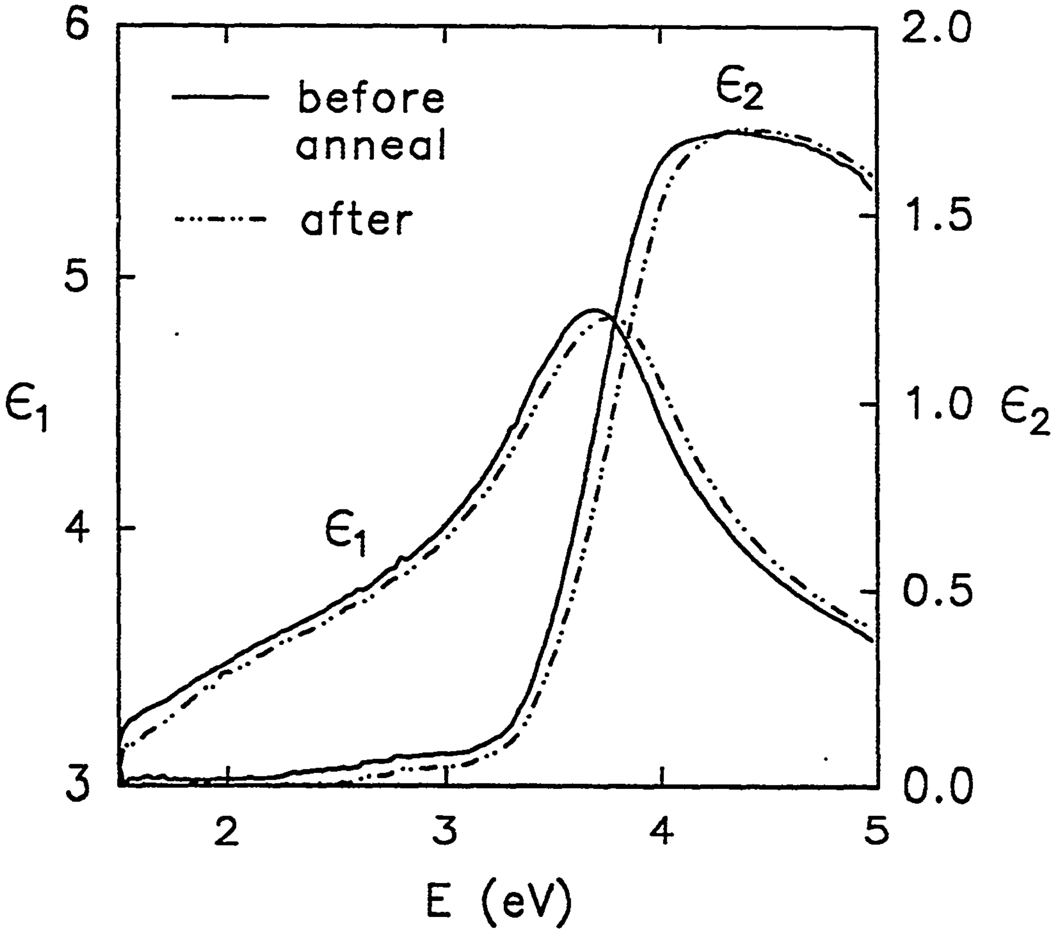

Figure 17. The dielectric functions of a doped ZnO sample before and after a one hour anneal at 320°C under vacuum. The shift in the optical gap value to higher energies can be attributed to a change in the electron concentration by ~10^{20} cm^{-3}.

respectively, yielding films with x=0.09. Interfaces were formed either with or without reactive gas dilution by H_2. To explore the specific role of gas phase H in the formation of the ZnO/a-SiC:H interface, we first discuss results for optimum electronic-quality alloys prepared with a dilution ratio, $H_2/(CH_4+SiH_4)$, of R=20. Interfaces were also formed between ZnO and the typical p-type a-SiC:H used in devices, where the $B_2H_6/(CH_4+SiH_4)$ flow ratio was 0.1%. Because the B_2H_6 was diluted to 1% in H_2, this gave a H_2-dilution ratio of R=0.1. The acquisition time for one pair of ellipsometric spectra from 1.5 to 4.5 eV was 0.16 s, and the repetition time was ~1 s.

The real-time SE (ψ, Δ) data collected during a-SiC:H growth with R=20 could only be understood within the framework of a model in which the underlying ZnO itself is modified upon interface formation. Even in the (unprocessed) real-time (ψ, Δ) spectra, the nature of the modification was clearly evident, namely, a shift to higher energies in the absorption onset or optical gap of the ZnO. The dominant contribution to the shift occurs during nucleation when the a-SiC:H is discontinuous.

Figures 18 and 19 show the results of a self-consistent, quantitative interpretation of the real-time spectra over the full range of accessible photon energies. The details of this analysis are included in the Phase II report (Collins et al., 1994a). Here we provide an overview of the earlier work and include new information that provides a clearer picture of the interfacial interaction (An et al., 1994). In the analysis, we determine (i) the initial nucleation and growth characteristics of the a-SiC:H (Fig. 18), (ii) the dielectric function of the modified ZnO (Fig. 19, inset), and (iii) the time evolution of the modified ZnO layer thickness (Fig. 19, main part).

The behavior shown in Fig. 18 is similar to that obtained for the growth of a-SiC:H on c-Si under identical conditions (Lu et al., 1993). For $t < 60$ s, a single layer (thickness: d) simulates the clusters that form in the initial stages of growth. For $t > 60$ s, a surface layer (thickness: d_s) simulates the microscopic roughness that is present once clusters make contact and an underlying bulk layer (thickness: d_b) forms. Cluster contact is complete and coalescence begins at t~60 s, when d_s=25 Å and d_b=3 Å. From this point onward, d_b increases linearly, and d_s relaxes (eventually to 12 Å). For $t < 60$ s, when the film is discontinuous, Fig. 19 reveals the layer-by-layer conversion of ZnO to the modified form with a 0.07 eV wider optical gap, as shown by the imaginary parts of the two dielectric functions at 250°C in the inset. Based on direct evidence presented in next two paragraphs, we propose that the behavior of Fig. 19 arises from the diffusion-limited penetration of H into the ZnO during plasma exposure (see Figs. 20 and 21).

Support for this proposition comes from a simpler experiment: RTSE during direct exposure of ZnO at 250°C to a weak atomic H flux generated by a filament. As described in Phase II, the data collected in this experiment could only be understood in terms of a layer-by-layer conversion of the original ZnO to a wider-gap material, in consistency with a diffusion front passing

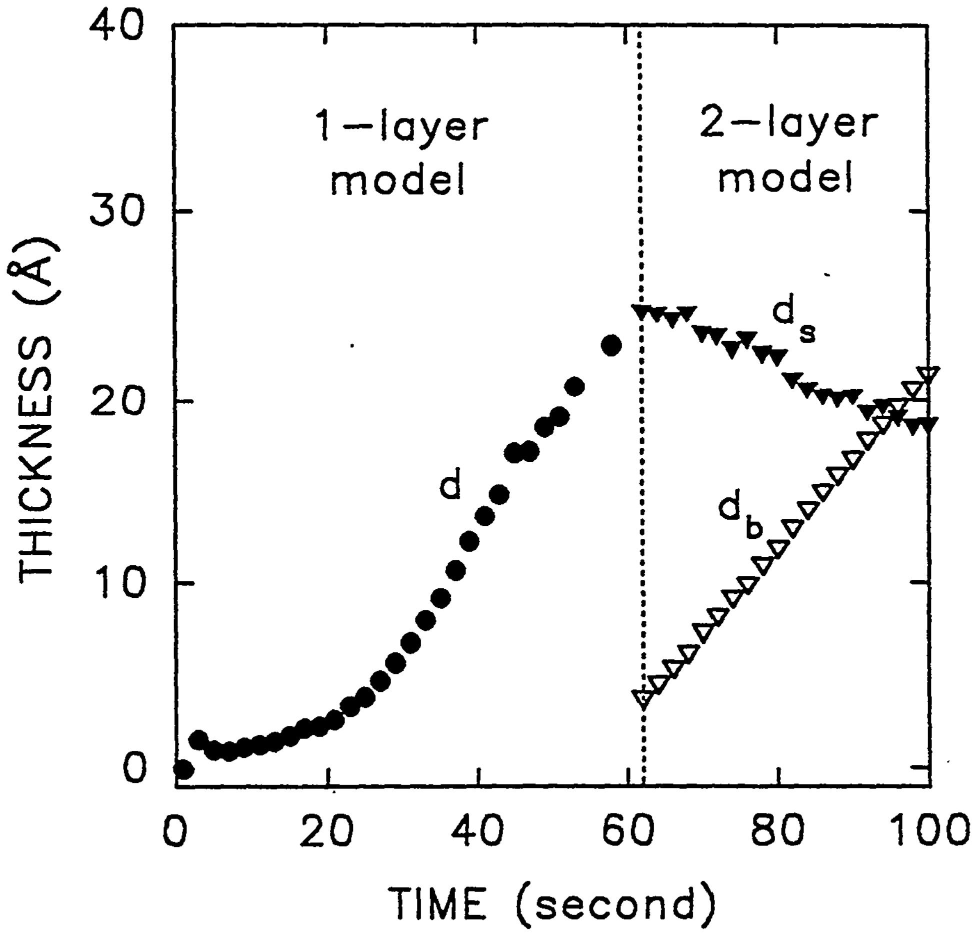

Figure 18. Time evolution of the thickness of a low-density nucleating layer (d: solid circles) in a one-layer model for t<60 s during the growth of a-SiC:H with R=20 onto undoped ZnO. The evolution of a low density roughness layer (d_s: solid triangles) and an underlying bulk layer (d_b: open triangles) in a two-layer model are shown for t>60 s. These results were deduced from real-time SE measurements.

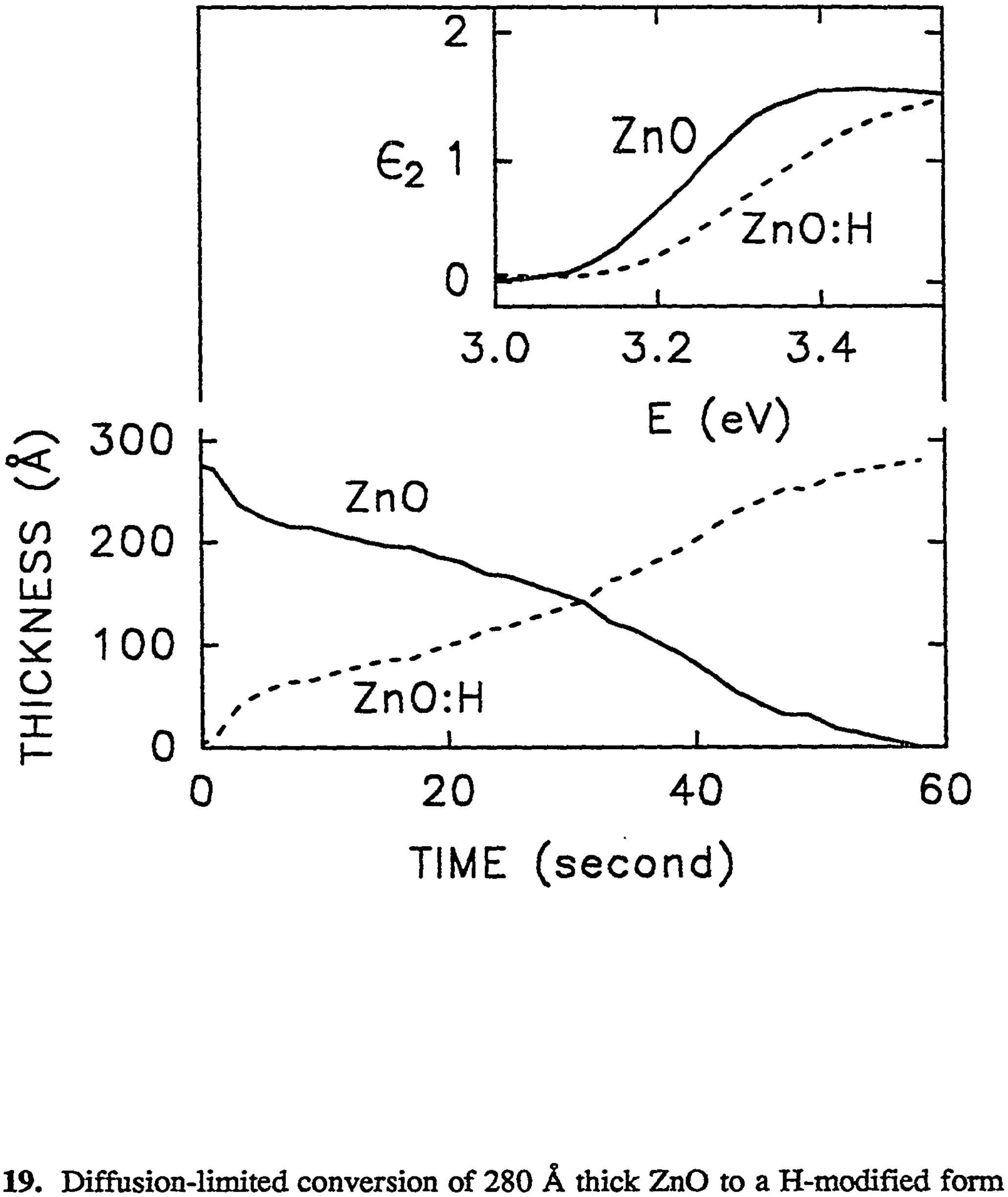

Figure 19. Diffusion-limited conversion of 280 Å thick ZnO to a H-modified form (ZnO:H) with a wider optical gap during the ZnO/a-SiC:H preparation of Fig. 18. The inset provides the imaginary parts of the dielectric functions in the neighborhood of the absorption onset for the as-deposited and modified ZnO, both measured at 250°C.

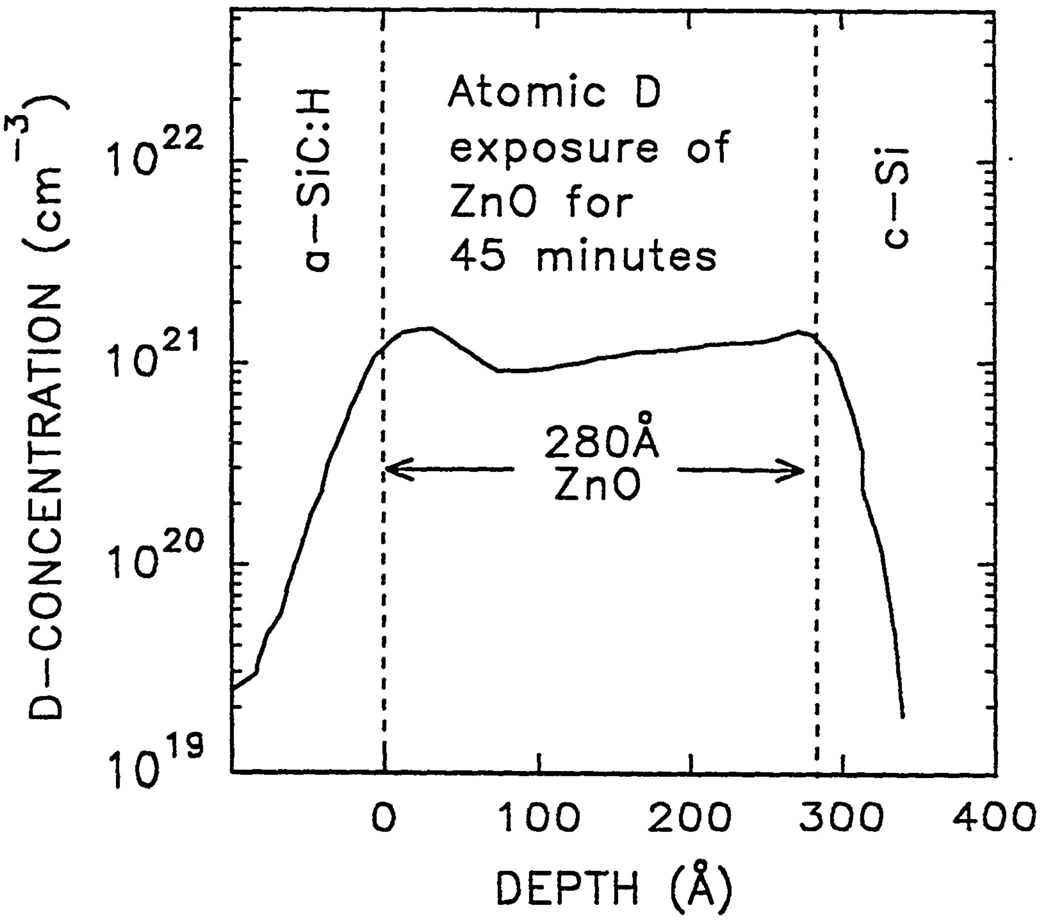

Figure 20. Deuterium depth profile from secondary ion mass spectrometry obtained on a 280 Å undoped ZnO sample exposed to a weak flux of atomic D for 45 minutes. In this time, the changes in the ellipsometric spectra saturated. After D-exposure, the sample was cooled to 215°C and capped with a-SiC:H prepared with no H_2 dilution (R=0).

throughout the film (Collins et al. 1994a). To demonstrate that H is directly involved in this change, Figure 20 shows a secondary ion mass spectrometry (SIMS) D profile of a 280 Å thick ZnO film exposed to atomic D for 45 minutes. By this time, the RTSE data showed no further changes. After atomic D exposure, the ZnO was cooled to 215°C under vacuum in an attempt to arrest further changes in the D profile. Finally, the interface region was capped with an undeuterated a-SiC:H layer with R=0 for protection against the environment. In Fig. 20, we observe a fairly uniform elevated D concentration in the film of $(1 \pm 0.3) \times 10^{21}$ cm^{-3} which is sufficient to account for the optical change.

A second assumption implicit in the analysis of Fig. 19 is that the modification of ZnO upon interface formation occurs throughout the full 280 Å thickness by t=60 s. As support for this assumption, SIMS analysis corroborates both the diffusion length and time scales as deduced by RTSE and shown in Fig. 19. In Fig. 21, we show a high resolution SIMS deuterium (D) profile for similarly-prepared a-SiC:H on undoped ZnO, 1000 Å thick. The only difference is that the alloy was deposited for only 30 s using D_2 as a diluent. Then the discontinuous film was cooled to 215°C under vacuum, and the interface region was capped with an undeuterated a-SiC:H layer with R=0 for protection. These results provide additional direct support for the role of H-modification of the ZnO in the observations of Fig. 19. In this case, the SIMS profile reveals a D tail that extends into the ZnO, falling by a factor of two at 180 Å. The 180 Å value in Fig. 21, if interpreted as the position of the diffusion front, is in good agreement with the value of ~150 Å obtained at t=30 s from the SE analysis of Fig. 19. *This agreement promotes confidence in the validity of the overall SE interpretation.*

Although the results in Figs. 18-19 were deduced for the model system of intrinsic a-SiC:H on undoped ZnO, as described in Phase II, a similar optical gap shift and conversion characteristic is found for p-type a-SiC:H prepared with R=20, and for substrate films of doped ZnO. For p-type a-SiC:H prepared without H_2-dilution, the initial H-incorporation effect on the ZnO is still clearly observable, but not as pronounced. There are two reasons for this result. First, the H in this case is derived mostly from hydrides, and second, due to the higher growth rate for R=0.1, the ZnO is exposed to the plasma for 15 s before it is fully covered (vs. 60 s for R=20). For the case of R=0.1, however, we find that some H diffuses from the p-type a-SiC:H into the ZnO in an equilibration process that continues to widen the ZnO gap even after the interface is formed (t > 15 s).

Figure 22 shows a comparison of raw ellipsometric ψ spectra before (open circles) and after (solid circles) the deposition of 0.2 monolayers of a-SiC:H on undoped ZnO. The upper data set (shifted by 2° for clarity) is for a-SiC:H prepared with 0.1% doping, but without additional H_2 dilution (R=0.1). The lower data set is for undoped a-SiC:H prepared with a high H_2 dilution level (R=20). The latter results are from the data set of Figs. 18 and 19. For deposition of

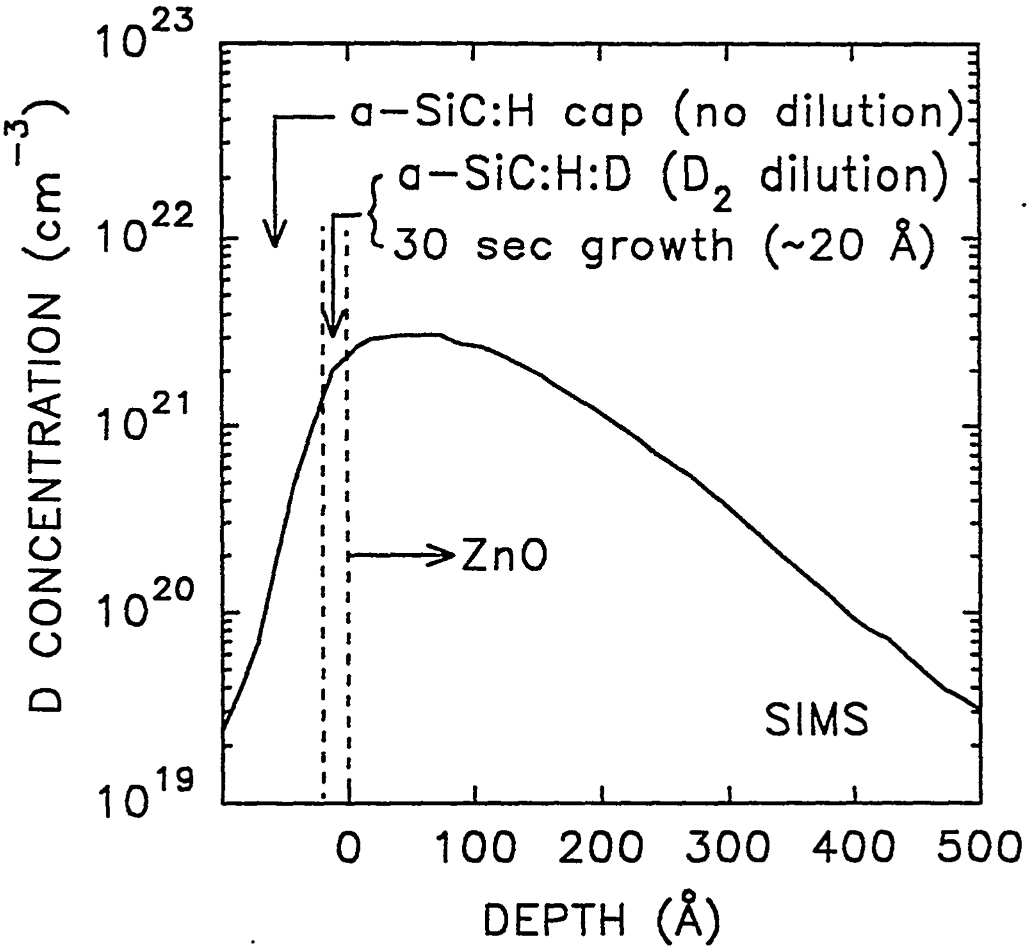

Figure 21. Deuterium depth profile from secondary ion mass spectrometry obtained on an a-SiC:H sample prepared onto undoped ZnO with D_2 dilution in the first 30 s of deposition. After 30 s, the sample was cooled to 215°C and capped with a-SiC:H prepared with R=0.

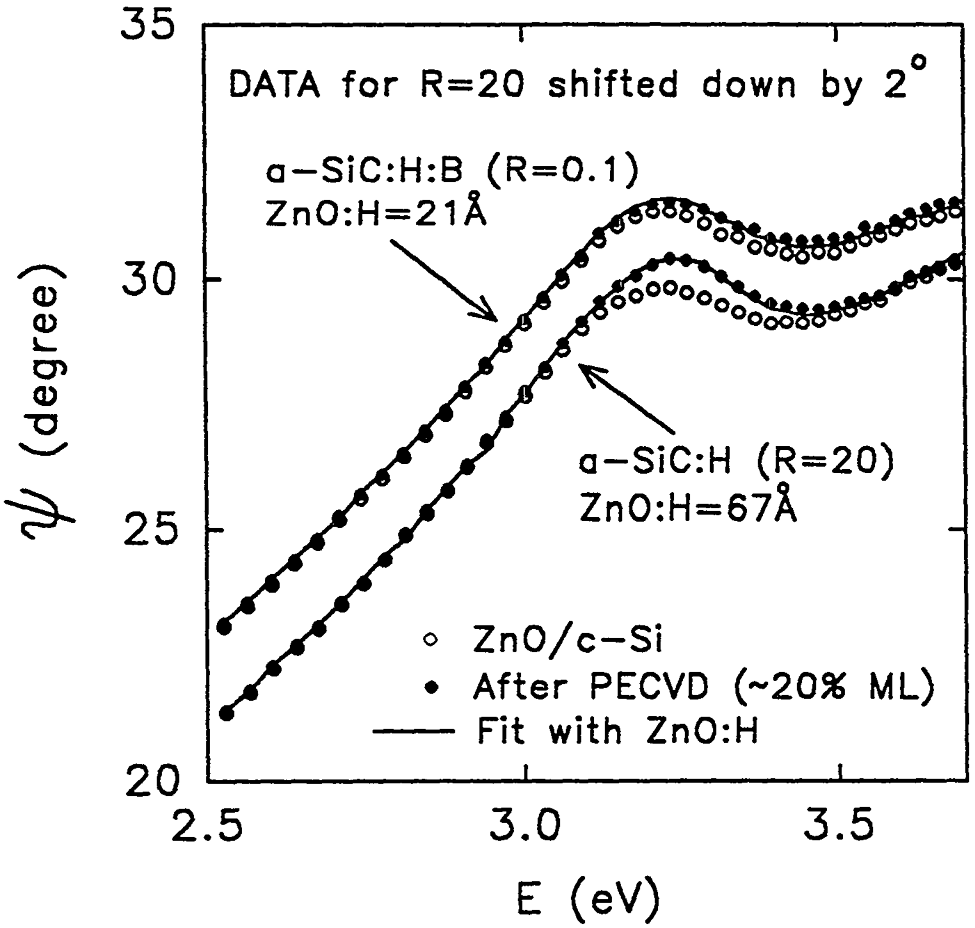

Figure 22. Raw ellipsometric ψ spectra before (open circles) and after (solid circles) the deposition of 0.2 monolayers of a-SiC:H on undoped ZnO. The upper data set (shifted by 2° for clarity) is for a-SiC:H prepared with 0.1% doping, but without additional H_2 dilution (R=0.1). The lower data set is for undoped a-SiC:H prepared with a moderate H_2 dilution level (R=20). The latter results are from the data set of Figs. 18 and 19. For deposition of a-SiC:H with such a low coverage, no change in ψ is expected. The change in ψ in the neighborhood of the ZnO optical gap can be attributed to H-penetration upon plasma striking. Note that the magnitude of the effect is larger for the deposition with R=20. In this case, the H has penetrated ~70 Å, in comparison to ~20 Å for R=0.1.

a-SiC:H with such a low coverage, no change in ψ is expected. The change in ψ in the neighborhood of the ZnO optical gap can be attributed to H-penetration upon plasma striking. Note that the magnitude of the effect is a factor of three-to-four larger for the deposition with R=20. In this case, the H has penetrated ~70 Å, in comparison to ~20 Å for R=0.1

The optical gap shift in the inset of Fig. 19 provides an estimate of the increase in carrier concentration ΔN in the near-interface ZnO, using a model that includes both the band gap widening due to the Burstein-Moss shift and the narrowing due to many-body effects. This model yields $\Delta N \sim 8 \times 10^{19}$ cm^{-3} for the observed optical gap shift of 0.07 eV (Jin et al., 1988). This result, in combination with the combined SIMS profiles for H and D in the ZnO, suggests that ~0.1-1% of the incorporated H is active in generating point defects (e.g., O vacancies or Zn interstitials), or defect complexes that contribute free electrons to the ZnO lattice.

Further evidence of the change in the properties of the ZnO at the interface is inferred from electrical conductivity measurements presented in Table II. In these experiments, coplanar contacts were deposited onto 1000 Å thick doped ZnO, and the resistivity of the TCO was measured before, during, and after the deposition of 300 Å layers of i- and p-type a-SiC:H. Overdeposition leads to a reproducible decrease in the effective resistivity of the ZnO from an initial value of 9.5×10^{-4} Ω cm to $(6.5-7.5) \times 10^{-4}$ Ω cm. Owing to the incomplete permeation of H through this ZnO film, the actual resistivity of the modified near-surface layer is expected to be lower than the latter value. These results, although difficult to interpret quantitatively, corroborate the increase in carrier concentration deduced optically.

4.3 *Role of B-contamination at ZnO/a-SiC:H:B Interfaces*

Figure 23 shows the final results of an analysis performed on RTSE data collected during exposure of ZnO to the gas mixture used to prepare p-type a-SiC:H. Here a gas flow ratio of 1:6:4 (doping gas):SiH_4:CH_4 (in sccm) was used and the total pressure was 0.2 Torr. The doping gas is 1% B_2H_6 in H_2, as usual. The data reveal a diffusion characteristic as the near-surface ZnO converts to a wider band-gap material over time. In the case of p-type gas exposure, only 50 Å conversion occurs over the course of an hour. This diffusion process is much slower than that observed during filament-generated atomic H exposure of ZnO (~15 s for 50 Å conversion) or $SiH_4/CH_4/H_2$ plasma exposure (~3 s for 50 Å conversion at R=20). We suggest that, in the experiment of Fig. 23, B_2H_6 breaks up on the surface and the resulting B is the diffusing species. The B dopes the near-surface of the ZnO p-type and enhances the electron concentration. This leads to the ~0.1 eV widening of the gap detected by RTSE.

As has been observed in the case of p-type gas exposure of SnO_2, there is only a weak CVD effect on ZnO. No more than 0.2 monolayers of a-Si:B:H material accumulates on the surface

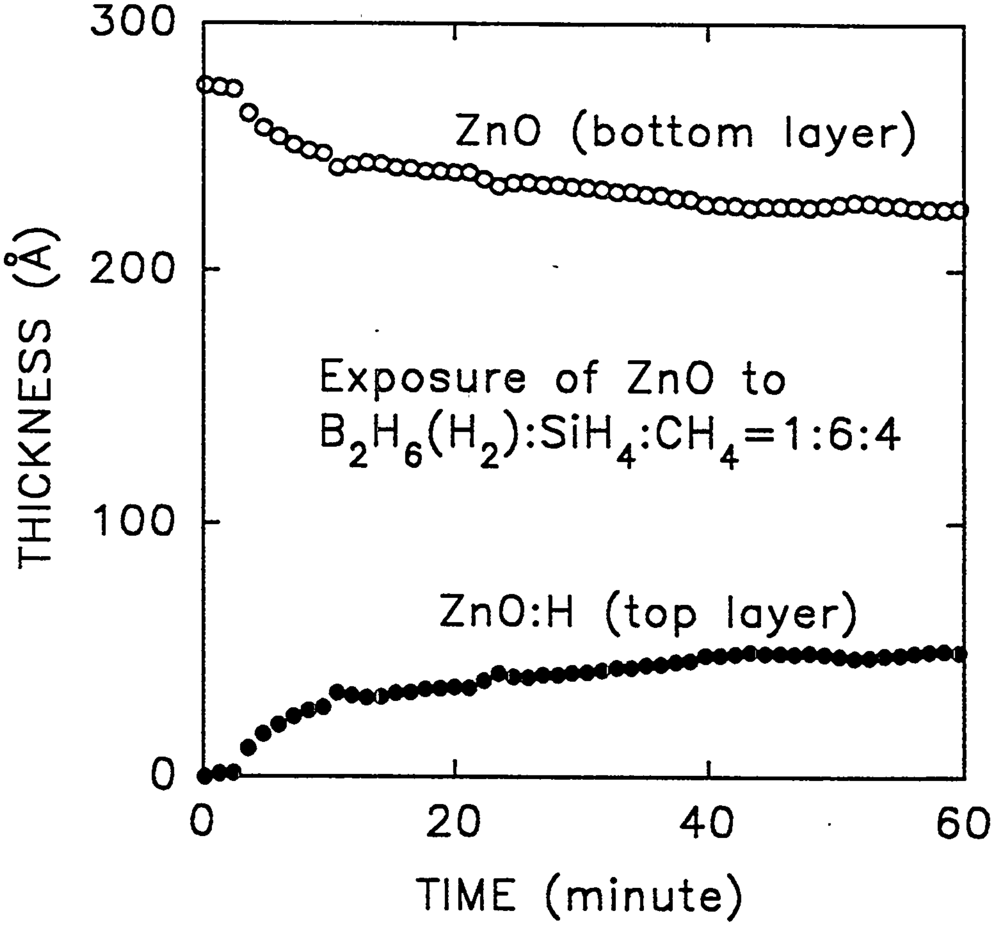

Figure 23. Evolution of modified layer thickness during exposure of ZnO at 250°C to the p-type gas mixture used to prepare a-SiC:H. Here the gas flow ratio is 1:6:4 (doping gas):SiH_4:CH_4 (in sccm) and the total pressure is 0.2 Torr. The doping gas is 1% B_2H_6 in H_2.

over a one hour exposure time. Thus, the average CVD layer growth rate is <0.008 Å/min. (<13 fm/s in SI units!). In general, the change that the ZnO surface undergoes in the time during which it is exposed to the p-type gas mixture is small compared with the changes induced upon plasma ignition. The results and subsequent discussion of Figure 23 suggests that for p-type deposition on ZnO, not only H, but also B, may diffuse into the ZnO and contribute to the optical gap widening effect.

The observed ZnO/p-layer interface effects discussed in detail in this and the previous sub-sections are included in the summary of Table VI, presented below.

4.4 *Comments on Role of H- and B-contamination of Transparent Conducting Oxides in the Solar Cell Configuration*

In general, preparation conditions for TCO's are established as a trade-off that balances high conductivity and high optical transparency. In Secs. 4.1-4.3, we have described various processes that may occur during the formation of interfaces between ZnO and p-type a-SiC:H and may affect this balance in the near-interface region of the ZnO. Each of these processes is characterized by a widening of the optical gap arising from an increase in the Fermi level position, and hence electron concentration, in the ZnO. The dominant such process is diffusion of H into the ZnO during p-layer nucleation, although post-nucleation H- and B-diffusion, and ZnO annealing may also occur. In spite of the fact that no excess optical absorption is detected by RTSE, it is possible that some additional optical losses in solar cells result from the enhancement in free carrier absorption in the ZnO near-interface region. Thus, such a loss would be different in nature than that observed for SnO_2, in which a true metallic phase is generated at the interface. Further assessment of optical losses in the near-interface region of ZnO are in progress, based on the predictions of the Drude model (Wooten, 1972) and the increase in carrier concentration deduced by RTSE.

In the absence of significant optical losses, it seems that an enhancement in the electron concentration in the near-interface ZnO would serve only to improve the device characteristics of the structure. However, such a conclusion is not definitive, since the nature of the contact is not well established. For example, if a narrow band of interface states controls the transport across the junction, an increase in the near-interface carrier concentration may lead to an increase in interface resistance. However, within such a model, the nature of the contact would also be a sensitive function of the initial doping level, as well. To our knowledge such sensitivity has not been reported.

In addition, we have observed no evidence in the RTSE data of any process that could be associated with a high interface resistance. For example it might be possible for oxygen atoms to leave the ZnO and react with Si at the interface to form a SiO_2 blocking layer. Typically, doped ZnO has an oxygen deficiency, and this reaction would then lead to free Zn at the interface, which is not observed. In comparing interfaces, it is interesting to note that free metal forms at the SnO_2/a-SiC:H:B interface, and the interface resistance in this case is relatively low; free metal does not form at the ZnO/a-SiC:H:B interface, and the interface resistance is believed to be higher. Thus, it is possible that a monolayer of free metal at the interface is beneficial to its electrical properties. In future studies of ZnO, we intend to expose the surface of the material to various controlled chemical treatments while probing by RTSE. In this way, we will attempt to establish treatment conditions that yield free Zn at the surface. Solar cells will be prepared on surfaces with and without the treatments, and an assessment of their performance will be undertaken.

5. Group IV Microcrystalline Thin Films

In Phase II, we reported the results of an optical study of microcrystalline films prepared by hydrogen dilution of methane-silane gas mixtures (Collins et al., 1994a). Figure 1 shows how the Si crystallite volume fraction in the film depends on the H_2-dilution ratio R for thick films. The earlier Phase II study was incomplete in that unexplained shifts in the band structure critical points for the microcrystallites away from those for bulk c-Si were observed. It was speculated that such shifts arise from the incorporation of C into the crystallites. In the first part of this section, we will clarify this issue, finding that our speculation was incorrect.

In the second part of this section, we will describe the results of a study of microcrystallite development in 100-300 Å thick p-type μc-Si:H films prepared by very high frequency (VHF)-PECVD (Prasad et al., 1991). This approach yields a high plasma density and may be favorable for the development of microcrystallites in thinner layers than is observed using conventional rf PECVD. In spite of this expectation, a loss of crystalline connectivity in these films appears to be correlated with a significant reduction in the conductivity for selected depositions in which the conductivity has been measured. In an attempt to improve upon this situation, we describe an alternative method for preparing ultrathin crystalline films that serve as seed layers for the immediate nucleation of microcrystals on any substrate.

5.1 *Microcrystalline SiC Films*

The films utilized in this first part of our study were deposited at a substrate temperature of 250°C, an rf power of 5 W (130 mW/cm^2), a H_2-dilution ratio of R=80, a total pressure of 1.4 Torr, and a total H_2 flow of 200 sccm. The variable in these studies was the SiH_4:CH_4 gas flow ratio which ranged from 2.5:0 to 1:1.5 (in sccm). Ultimately, the goal of this study was to observe how the variable C incorporation affected the electronic structure of the crystallites. Before describing the crystallite electronic transitions, we will discuss the microstructure. In Table III, the final results of the microstructural analysis for films having thicknesses ranging from ~800 Å to ~1700 Å. These results were obtained by fitting the dielectric functions as measured by SE. A two-layer model is used in the microstructural analysis, consisting of low-density surface and dense bulk layers. The surface and bulk layers in turn are analyzed as three-phase mixtures of a-SiC:H, μc-Si:H, and void. Such modeling has led to very good fits so there is no need to appeal to a crystalline SiC phase in these films.

An electron microprobe analysis of the film with a 1.5:1 SiH_4:CH_4 ratio yields an estimated $Si_{1-x}C_x$ composition of x=0.05. Purely amorphous $Si_{1-x}C_x$:H films prepared with R values from 0 to 20, but the same SiH_4:CH_4 ratio (3:2, in sccm), yield x=0.09. Because the microcrystalline films have 60 vol.% amorphous component, we can conclude from these results that the amorphous component in the microcrystalline films has the same Si:C ratio as the pure amorphous films prepared with the same SiH_4:CH_4 ratio. This shows that the crystallites form in such a way as to exclude C from the film, leading to a lower net C concentration.

Figure 24 shows the volume fractions of the three phases in the bulk layer as a function of the CH_4:SiH_4 gas flow ratio for films on oxide-covered c-Si substrates (solid points). Clear trends can be observed with increasing CH_4 flow. The a-SiC:H component increases from 0.43 to 0.70, the μc-Si:H component decreases from 0.47 to 0.26, and the void volume fraction falls from 0.10 to 0.04. Results for a ZnO substrate (open point) reveal a somewhat lower volume fraction of crystallites, suggesting that it may be more difficult to nucleate the crystallites in this case. The trends for depositions on c-Si substrates lead to two suppositions: (i) C stabilizes the amorphous phase under our deposition conditions, and (ii) the microcrystalline phase induces additional voids. The latter effect is probably due to the fact that microcrystallites cannot fill all space and therefore trap voids in the film. This effect is observed in Figure 1 as well: a void density increase accompanies the development of microcrystals with increasing R.

Table IV shows the results of second derivative analyses of the microcrystallite dielectric functions, designed to determine the energy position of the density-of-states critical points in the microcrystallites. In this case, we present results for those depositions on c-Si and Cr substrates that yield films containing a sufficient volume of crystallites for accurate analysis. In comparing the results with the bulk Si critical point energies, it is clear that the E_0'-E_1 critical point complex shifts upward in energy, while the E_2 critical point complex shifts downward in energy. This effect is observed independent of whether C has been incorporated in the film. Thus, the effect cannot be due to C incorporation in the crystallites as suggested in our Phase II report. Further insights are gained from the fact that isolated c-Si particles do not exhibit such shifts (Nguyen and Collins, 1993), and the shifts occur only after the thin films have coalesced. This observation

TABLE III

SAMPLE (SiH_4:CH_4; substrate)	Bulk Layer				Surface Roughness Layer			
	a-Si(C):H	c-Si	Void	d(Å)	a-Si(C):H	c-Si	Void	d(Å)
Si:H (2.5:0 Si sub)	0.426 ±0.079	0.472 ±0.078	0.102 ±0.014	1231.6 ±33.7	0.449 ±0.030	0.266 ±0.024	0.285 ±0.018	77.6 ±13.7
SiC:H (2.0:0.5 Si sub)	0.566 ±0.050	0.352 ±0.050	0.082 ±0.006	1364.5 ±25.5	0.437 ±0.081	0.212 ±0.041	0.351 ±0.070	41.9 ±13.3
SiC:H (1.5:1.0 Si sub)	0.596 ±0.033	0.335 ±0.032	0.069 ±0.006	1220.6 ±19.7	0.523 ±0.192	0.106 ±0.113	0.371 ±0.155	22.8 ±11.6
SiC:H (1.0:1.5 Si sub)	0.700 ±0.045	0.262 ±0.044	0.038 ±0.011	785.8 ±20.0	0.500 ±0.052	0.258 ±0.028	0.242 ±0.044	62.4 ±13.9
SiC:H (1.5:1.0 ZnO sub)	0.691 ±0.034	0.267 ±0.032	0.042 ±0.011	1520.4 ±19.8	0.521 ±0.074	0.170 ±0.033	0.309 ±0.066	52.8 ±11.6

Table III. Microstructural analysis of 800-1600 Å thick mixed phase a-Si(C):H/μc-Si:H films prepared onto c-Si and ZnO substrates with a H_2-dilution ratio of R=80. The only variable deposition parameter in this series was the SiH_4:CH_4 ratio which ranged from 2.5:0 to 1:1.5 (in sccm). A two-layer model for the film is employed, consisting of a bulk layer and a surface roughness layer. The composition of the bulk layer is plotted versus CH_4 flow in Fig. 24.

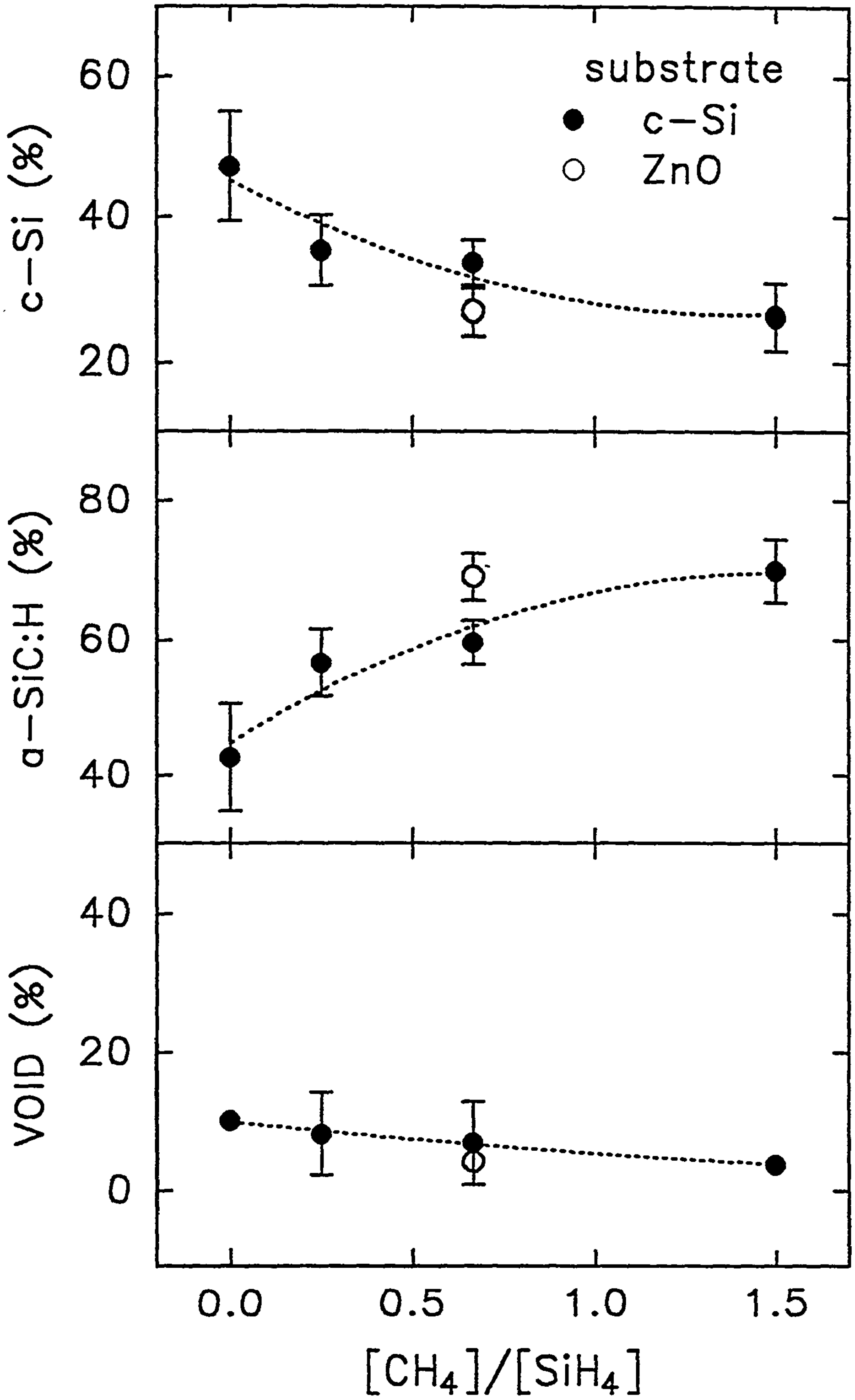

Figure 24. Volume fractions of c-Si, a-Si(C):H, and void in the bulk layer, plotted as a function of the CH_4/SiH_4 flow ratio, for the mixed phase a-Si(C):H/μc-Si:H films of Table III. The substrates were c-Si (solid circles) and ZnO (open circle), and the H_2-dilution ratio and substrate temperature were fixed at R=80 and T_s=250°C, respectively.

TABLE IV

SAMPLE (SiH_4:CH_4; substrate)	E_0'-E_1		E_2	
	E (eV)	Γ (eV)	E (eV)	Γ (eV)
c-Si	3.376±0.002	0.120±0.002	4.275±0.003	0.078±0.003
μc-Si:H (5:0 Cr sub)	3.397±0.030	0.256±0.030	4.236±0.004	0.224±0.040
μc-Si:H (5:0 Si sub)	3.448±0.012	0.270±0.012	4.253±0.014	0.228±0.014
μc-Si:H (4:1 Cr sub)	3.410±0.048	0.305±0.048	4.233±0.029	0.194±0.029
μc-Si:H (4:1 Si sub)	3.426±0.018	0.312±0.018	4.255±0.016	0.244±0.016
μc-Si:H (3:2 Si sub)	3.461±0.047	0.413±0.047	4.247±0.066	0.270±0.066
μc-Si:H (3:2 Si sub)	3.413±0.083	0.398±0.083	4.261±0.057	0.243±0.057

Table IV. Energy positions and widths for the two dominant crystalline Si optical transitions, E_0'-E_1 and E_2, determined for the c-Si component of the mixed phase a-Si(C):H/μc-Si:H films of Table III. Corresponding results for bulk, single-crystal Si appear at the top. Data are included for depositions on c-Si and Cr substrates for which there is sufficient c-Si component in the film to extract an accurate dielectric function. All deposition parameters were fixed, except for the CH_4/SiH_4 flow ratio, which identifies the sample at the left. The H_2-dilution ratio and substrate temperature were 80 and 250°C, respectively.

suggests that the shifts are due to strain in the crystallites that is generated as the crystallites contact one another. In any event the effect appears to be beneficial for microcrystalline p-layers in solar cells in that it leads to a weaker absorption in the blue part of the spectrum.

5.2 *Thin p-Type Doped Microcrystalline Si Films*

Table V shows the results of a microstructural analysis of very thin p-type μc-Si:H films prepared by VHF-PECVD (70 MHz) on Corning 7059 glass substrates. These results were obtained in an analysis of ex situ spectroscopic ellipsometry data collected over a wide range, from 1.6 to 5 eV (see Fig. 25 for a typical best fit). Three differences should be noted here in comparison to the results of Table III and Fig. 24. First, the films are much thinner, ranging from ~100 Å to ~300 Å; second, no carbon is intentionally included, and, third, the films are doped p-type. For these depositions, SiH_4, B_2H_6, and H_2 gases were used. The H_2-dilution level (H_2/SiH_4) was given by R=60, with a total H_2 gas flow of 100 sccm. The doping gas flow ratio, B_2H_6/SiH_4, was 0.7%. The total gas pressure was 6 Torr. The plasma power was 10 W, yielding a flux of 75 mW/cm^2 at the substrate. The substrate temperature was 170°C.

For the data presented in the Table, a single-layer model was used for film thicknesses less than 180 Å. For these thicknesses, a two-layer model for the film could not be used since there was no clear distinction between surface and bulk. This indicates that coalescence has occurred only partially, as indicated by the fact that the void contents of these films are greater than 0.35 in volume fraction. For total thicknesses of ~220 Å or greater, coalescence has progressed further, as indicated by the applicability of a two-layer model for the film with a relatively dense underlayer (0.14 void volume fraction) and a low density overlayer which essentially consists of crystallites protruding randomly above the film surface. Figure 25 show the typical quality of the fit between the raw ellpsometric data and the best fit model that utilizes two layers for the thickest (300 Å total) μc-Si:H film. The excellent fit over the full photon energy range attests to the validity of our analysis.

Figure 26 shows the crystalline, amorphous, and void volume fractions in the bulk layer versus total film thickness, and Figure 27 shows the conductivity plotted logarithmically versus crystalline volume fraction for selected films. The drop in conductivity between crystalline volume fractions of ~0.25 and 0.10 may separate conduction through contacting crystallites at high crystallite volume fraction, and conduction through an amorphous matrix at low volume fractions. Obviously, the goal in making high conductivity, doped μc-Si:H in very thin layers is to achieve a high volume fraction of crystallites in the layers. The next part of this section describes a first step in this direction.

TABLE V

SAMPLE NUMBER	Bulk Layer				Surface Roughness Layer		
	a-Si:H	c-Si	Void	d(Å)	c-Si	Void	d(Å)
R100293B	0.489 ±0.013	0.116 ±0.013	0.395 ±0.004	106.91 ±2.15	0	0	0
R050293B	0.449 ±0.016	0.158 ±0.016	0.393 ±0.004	130.17 ±2.72	0	0	0
R030293B	0.354 ±0.024	0.289 ±0.024	0.357 ±0.005	180.85 ±3.84	0	0	0
R020293B	0.437 ±0.036	0.419 ±0.031	0.144 ±0.018	179.20 ±8.20	0.291 ±0.052	0.70 ±0.05	38.06 ±2.46
R010293B	0.441 ±0.027	0.479 ±0.026	0.080 ±0.006	257.38 ±2.82	0.295 ±0.023	0.70 ±0.02	44.11 ±1.18

Table V. Microstructural analysis of very thin, mixed phase p-type μc-Si:H films prepared by very high frequency plasma-enhanced chemical vapor deposition (VHF-PECVD) onto glass substrates with a B_2H_6/SiH_4 doping gas flow ratio of 0.7%, a H_2-dilution ratio of R=60, and a substrate temperature of 170°C. The only variable deposition parameter in this series was deposition time which yielded thicknesses ranging from 100 to 300 Å. For the two thicker films, a two-layer model is employed, consisting of a bulk layer and a surface roughness layer. For the thinner layers, a one-layer model was employed. The composition of the single layer or bulk layer is plotted versus thickness in Fig. 26.

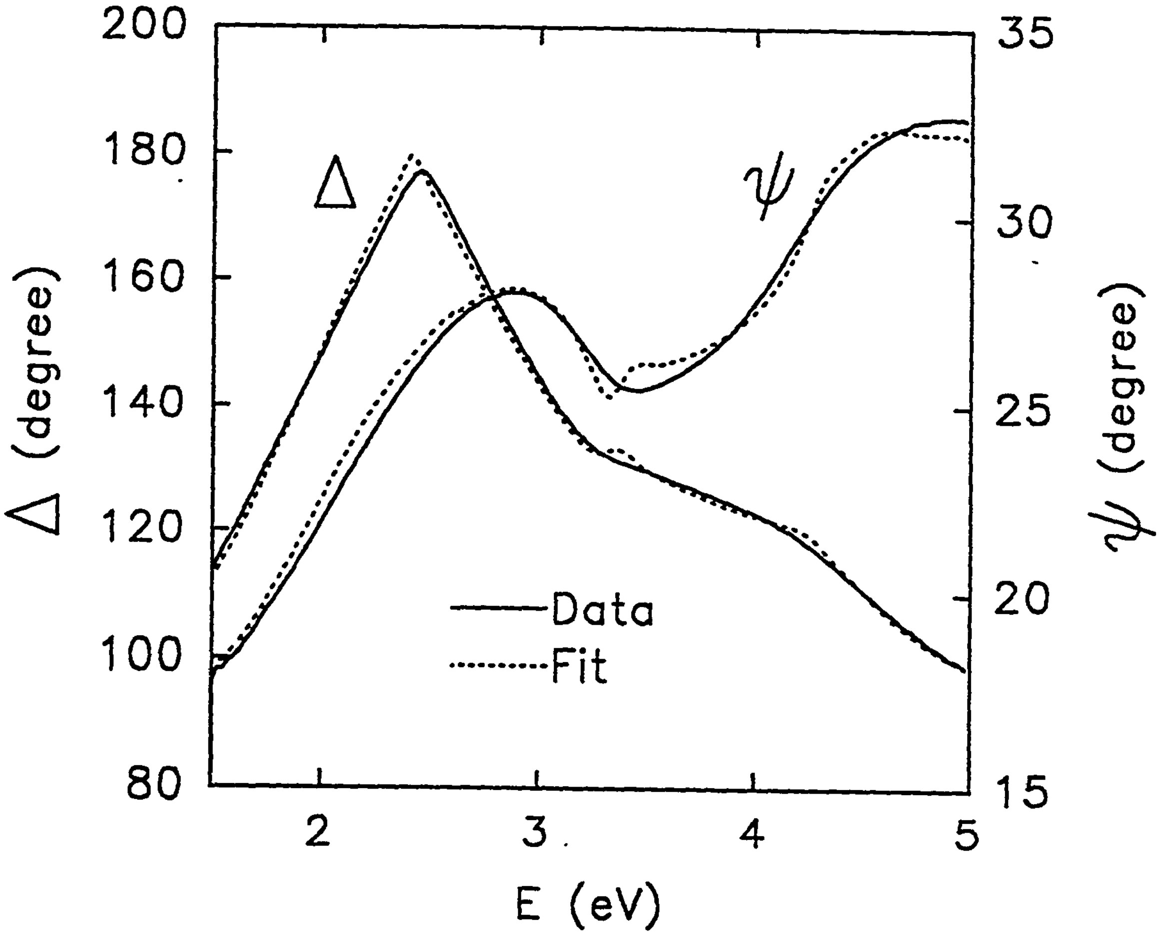

Figure 25. Experimental spectroscopic ellipsometry data (solid) plotted in terms of ψ and Δ for the thickest μc-Si:H:B film of Table V, prepared by VHF-PECVD. The broken line respresents the best fit using the model parameters provided in the last row of Table V.

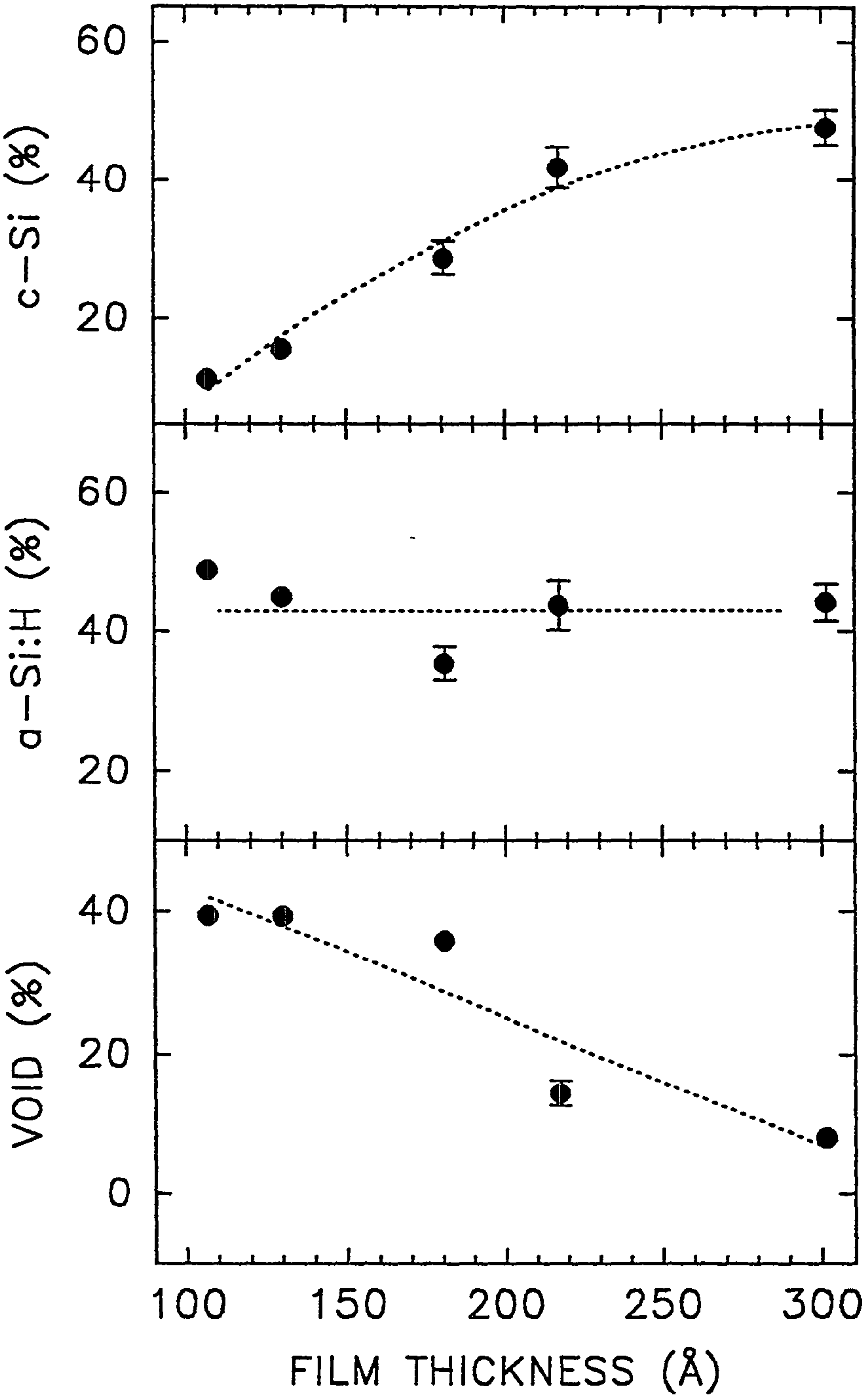

Figure 26. Volume fractions of c-Si, a-Si:H, and void in the bulk layer plotted as a function of total thickness for the p-type μc-Si:H films of Table V, prepared by VHF-PECVD onto glass substrates. These results were obtained from an analysis of ex situ spectroscopic ellipsometry data.

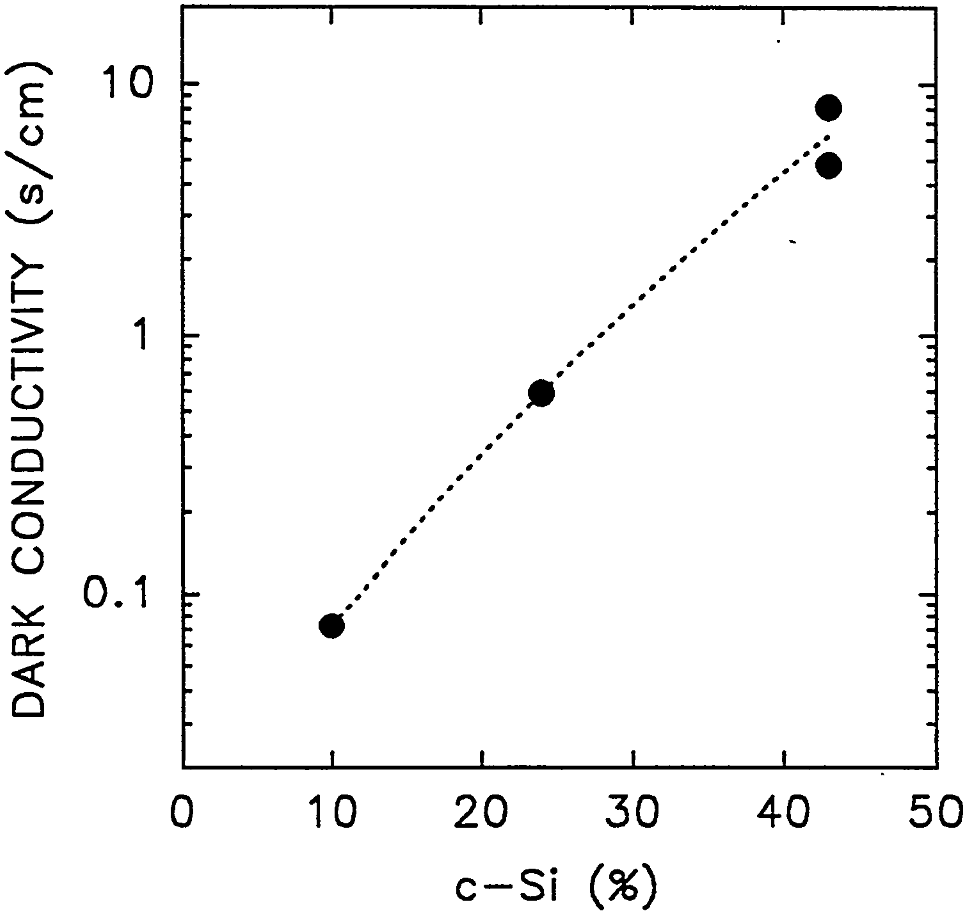

Figure 27. Room temperature electrical conductivity plotted versus c-Si volume fraction in the bulk layer for the p-type μc-Si:H films of Table V, prepared by VHF-PECVD onto glass substrates.

5.3 *Microcrystal Nucleation on Arbitrary Substrates via Seeding*

As described in the previous part, the applications of doped μc-Si:H in solar cells are limited by the difficulty of nucleating the crystalline phase onto different substrate materials. As an example, μc-Si:H growth on Cr substrates yields a nucleation density as low as 3×10^{10} cm^{-2} (Nguyen and Collins, 1993), meaning that the coalescence of nuclei commences only after a film thickness of ~300 Å. A low nucleation rate also occurs on some transparent conducting oxide (TCO) substrates, and this effect tends to compound the problem of TCO modification by gas phase atomic H (Nguyen and Collins, 1994).

In spite of nucleation problems, considerable flexibility exists in the preparation of μc-Si:H thin films. For example, μc-Si:H can be obtained by alternating a-Si:H growth by PECVD with H_2 plasma exposure at 150-250°C (Asano, 1990). Apparently during the H_2 plasma exposure step, hydrogen diffuses into the a-Si:H and disrupts the near-surface Si-Si bonding sufficiently to allow network relaxation to the crystalline state, accompanied by a release of H_2. Crystallization may also be assisted by atomic-scale surface roughness on a-Si:H, that permits greater movement of near-surface Si atoms during relaxation. The plasma crystallization phenomenon also provides an explanation for the compatibility of a-Si:H and μc-Si:H deposition. When μc-Si:H is deposited on a-Si:H from a H_2-rich plasma, the near-surface a-Si:H crystallizes to form nucleation sites for μc-Si:H (Yang et al., 1993).

In this part, we present a study of the evolution of thin film Si microstructure during an etching process that yields near-surface crystallites. Etching is performed with thermally-generated atomic hydrogen in order to avoid plasma damage. Real-time spectroscopic ellipsometry (RTSE) is applied to characterize the evolution of the near-surface μc-Si:H and underlying a-Si:H layer thicknesses, as well as the optical properties of the layers. It is found that near the end of the etching process, an ultrathin, single-phase layer of Si microcrystallites is present on the substrate surface. These crystallites are densely packed on the substrate in comparison with those of conventional single-phase μc-Si:H prepared by PECVD. For example, films 10 Å thick almost fully cover the substrate surface with an estimated Si-Si bond packing density that is 60% of the bulk value. The results of this investigation suggest processing methods for improving interfaces in μc-Si:H junctions.

5.3.1 Experimental Details for Generating μc-Si:H Seed Layers

The a-Si:H films etched in this study were prepared to initial thicknesses of 150-200 Å by rf PECVD under the following conditions: 250°C substrate temperature; 52 mW/cm^2 plasma power flux; and 0.2 Torr SiH_4 pressure. The substrate was an opaque chromium film deposited onto glass by dc magnetron sputtering, under conditions chosen to optimize the microstructure. Thus, roughness at the a-Si:H/Cr interface is avoided, as is substrate-induced void structure in the a-Si:H film (Collins and Cavese, 1988). RTSE was performed using a rotating-polarizer ellipsometer with a multichannel detection system. During PECVD, acquisition and repetition times were set at 160 ms and 1 s for full spectra in (ψ, Δ) from 1.5 to 4 eV. Here, (ψ, Δ) are the ellipsometry angles defined by: $\tan\psi \exp(i\Delta) = r_p/r_s$, where r_p and r_s are the complex reflection coefficients for p- and s-polarized waves.

Etching was performed by exposing the a-Si:H to atomic H, thermally generated using a filament heated in a low pressure (8 mTorr) H_2 atmosphere. Previous studies have shown that layer-by-layer etching occurs without generation of significant additional surface roughness or columnar microstructure in the a-Si:H (Collins et al., 1992). The etch rate depends on the concentration of H in the gas phase, which can be controlled by the filament power. When 35 W is applied to a 0.025 cm diameter W filament, it reaches a temperature of ~2250°C, and these conditions yield an a-Si:H etch rate of 10 Å/min. for a direct, line-of-sight filament-sample configuration. Because etching can be controlled at lower rates than growth, acquisition and repetition times for (ψ, Δ) spectra were 3.2 and 14.5 s.

5.3.2 Results and Discussion of μc-Si:H Seed Layer Studies

In Figure 28, a typical trajectory in the real and imaginary parts of the pseudo-dielectric function $\langle\varepsilon\rangle = \langle\varepsilon_1\rangle + i\langle\varepsilon_2\rangle$ at 3.41 eV depicts a-Si:H growth (circles) and etching (triangles). $\langle\varepsilon\rangle$ is calculated from (ψ, Δ) using the Fresnel equations for a single interface (Azzam and Bashara, 1976). These results were selected from a full RTSE data set spanning a useful range from 1.5 to 4 eV in ~80 spectral positions.

The characteristic features of a number of physical processes can be identified in Fig. 28, based on modeling of the full RTSE data set. These features permit real-time control of the growth/etching process. First, the lobe in the early stages of growth, consisting of a decrease in $\langle\varepsilon_2\rangle$, represents the formation of isolated nuclei. These nuclei make contact when they reach a thickness of 23 Å (arrow); here the first bulk-like monolayers begin to form. From this point onward, the nucleating layer remains as roughness on the surface of the bulk layer, but relaxes from a thickness of 23 Å to 15 Å in the first 50 Å of bulk film growth. In Fig. 28, the bulk film is grown to a thickness of 180 Å before deposition is terminated. When the film is exposed to atomic H, three processes occur simultaneously: (i) layer-by-layer etching of the film structure that leads to a reversal of the trajectory, (ii) reaction-limited Si-Si bond-breaking that modifies the dielectric function of the bulk a-Si:H throughout the thickness, and (iii) conversion of the near-surface layer of the a-Si:H to a μc-Si:H phase. The latter two processes have saturated in the

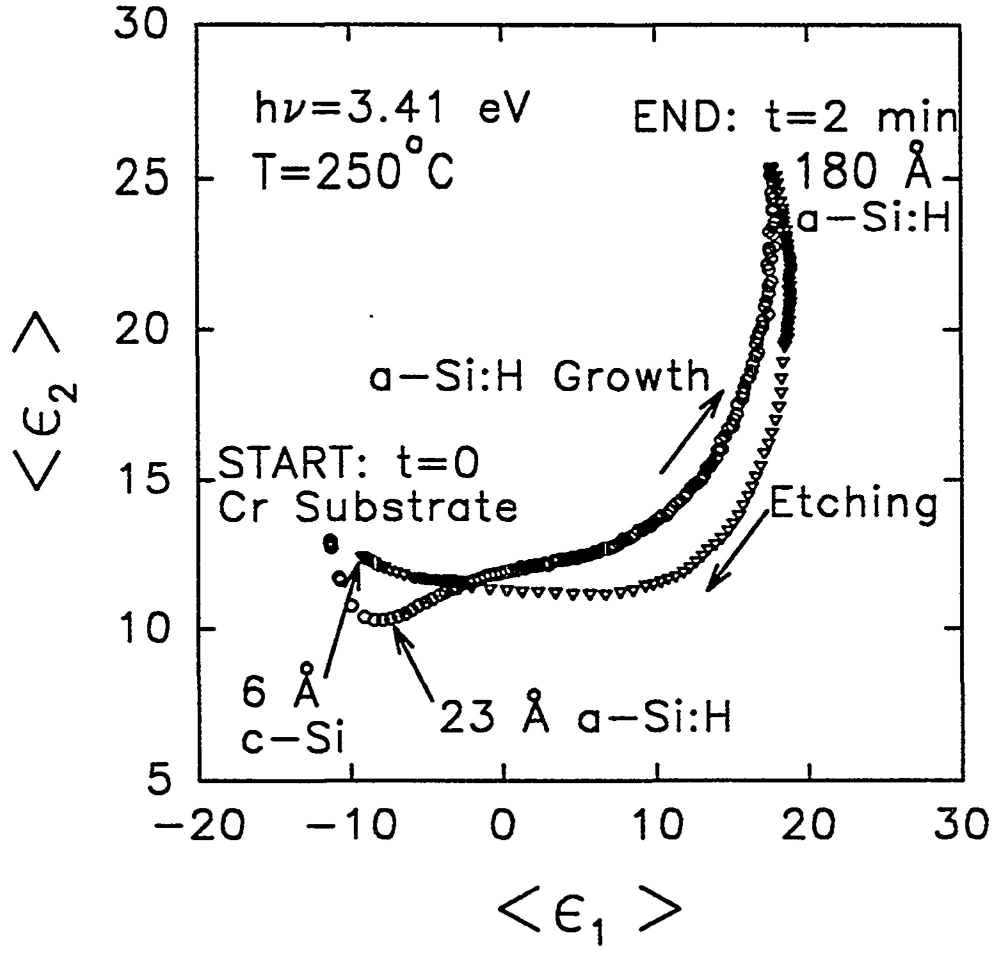

Figure 28. Typical pseudo-dielectric function trajectory at 3.41 eV depicting the growth of a-Si:H to a bulk layer thickness of 180 Å on a Cr substrate (circles). Subsequently, the film was etched by exposure to thermally-generated atomic H (triangles). The process was terminated in order to leave a 6 Å thick layer of single phase μc-Si:H at the interface to the substrate. The sample temperature throughout this process was 250°C.

later stages of etching, allowing us to extract accurate information on the near-surface μc-Si:H.

Least-squares regression analysis and mathematical inversion methods were applied to RTSE spectra collected during the later stages of such an etching run, in order to deduce the microstructural evolution and dielectric functions associated with the film structure. The procedure is the same as that used in the studies of a-Si:H film growth reported elsewhere. It first involves establishing the number of layers required to model the film structure. Once this is done, the dielectric functions of the layer components and the thicknesses and compositions of the layers are obtained in an iterative, self-consistent analysis. Figures 29 and 30 show the key results of the analysis. These results are taken from two different runs, and provide the clearest insights into the later stages of the etching process.

The analysis of Fig. 29 reveals a transition from a two-layer to a one-layer model as etching proceeds (vertical broken line). In the two-layer regime, $t < 33$ min., the surface layer (thickness: d_s) simulates the combined effects of surface roughness and Si crystallization, with a dielectric function determined from the Bruggeman effective medium theory as a μc-Si:H/void mixture. The underlying layer (thickness: d_b) simulates a-Si:H with an assumed thickness-independent dielectric function. This latter dielectric function is established as part of the fitting procedure, in which d_s, d_b, and the surface layer void volume fraction are also determined. In the one-layer regime, $t > 33$ min, a single-phase μc-Si:H/void layer (thickness: d) remains at the substrate interface. The dielectric function of the μc-Si:H component is deduced by direct inversion of the (ψ, Δ) spectra collected just after t=33 min. in the one-layer regime. The void volume fractions in the crystalline layers are measured relative to dense, thick, single-phase μc-Si:H prepared by PECVD. The inset in Fig. 29 shows the void volume fraction in the μc-Si:H layer versus thickness in the one-layer regime (squares).

Next, we will discuss the features that develop versus time in Fig. 29. During etching, the μc-Si:H surface layer is stable at 13 Å, representing an equilibrium between loss from the surface, and crystallization of deeper a-Si:H. When the underlying a-Si:H layer thickness is ~25 Å, the H concentration is reduced to decelerate etching. The underlying film is fully etched away at t~33 min., leaving a 10 Å μc-Si:H film. The inset shows that the void fraction in the μc-Si:H layer increases to 0.60 as the film thickness is etched down to a monolayer. The solid line is the result expected for hemispheres on a 15 Å square grid that decrease in size versus time during etching. The results appear to be consistent with a disc-like, rather than hemispherical geometry. Overall, we can conclude that etching occurs more uniformly than growth. This asymmetry is evident in Fig. 28 in that the etching trajectory crosses the growth trajectory before termination. Finally, the $(\langle\varepsilon_1\rangle, \langle\varepsilon_2\rangle)$ spectra for the Cr substrate are identical before and after the growth/etching process of Fig. 29; thus, no modification of the Cr is incurred that would lead to errors in the optical analysis.

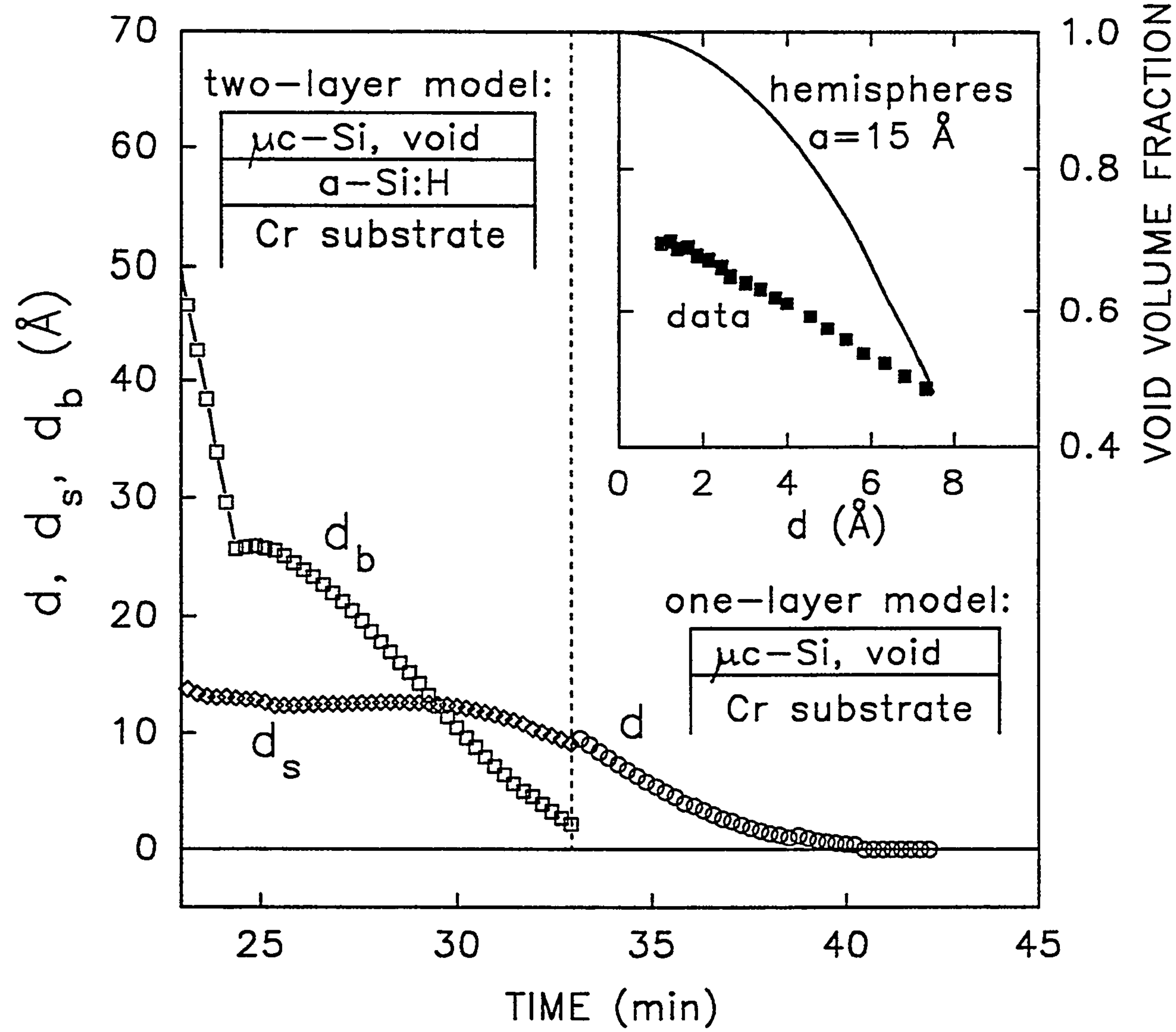

Figure 29. Evolution of a-Si:H and μc-Si:H layer thicknesses obtained in an analysis of RTSE data collected in the later stages of the complete etching of a-Si:H on a Cr substrate. For t > 33 min., a one-layer optical model for the etched film is sufficient to fit the data. The dielectric function of the layer is modeled as a mixture of μc-Si:H and voids using an effective medium theory. The inset shows the void volume fraction in the film versus thickness in this regime (squares). The solid line in the inset is the expected result for hemispherical Si clusters on a 15 Å square grid that decrease in size uniformly during etching. For t < 33 min., a two-layer optical model for the film is required. The underlying layer is bulk a-Si:H with a thickness-independent dielectric function, and the top layer is modeled as a physical mixture of μc-Si:H/void.

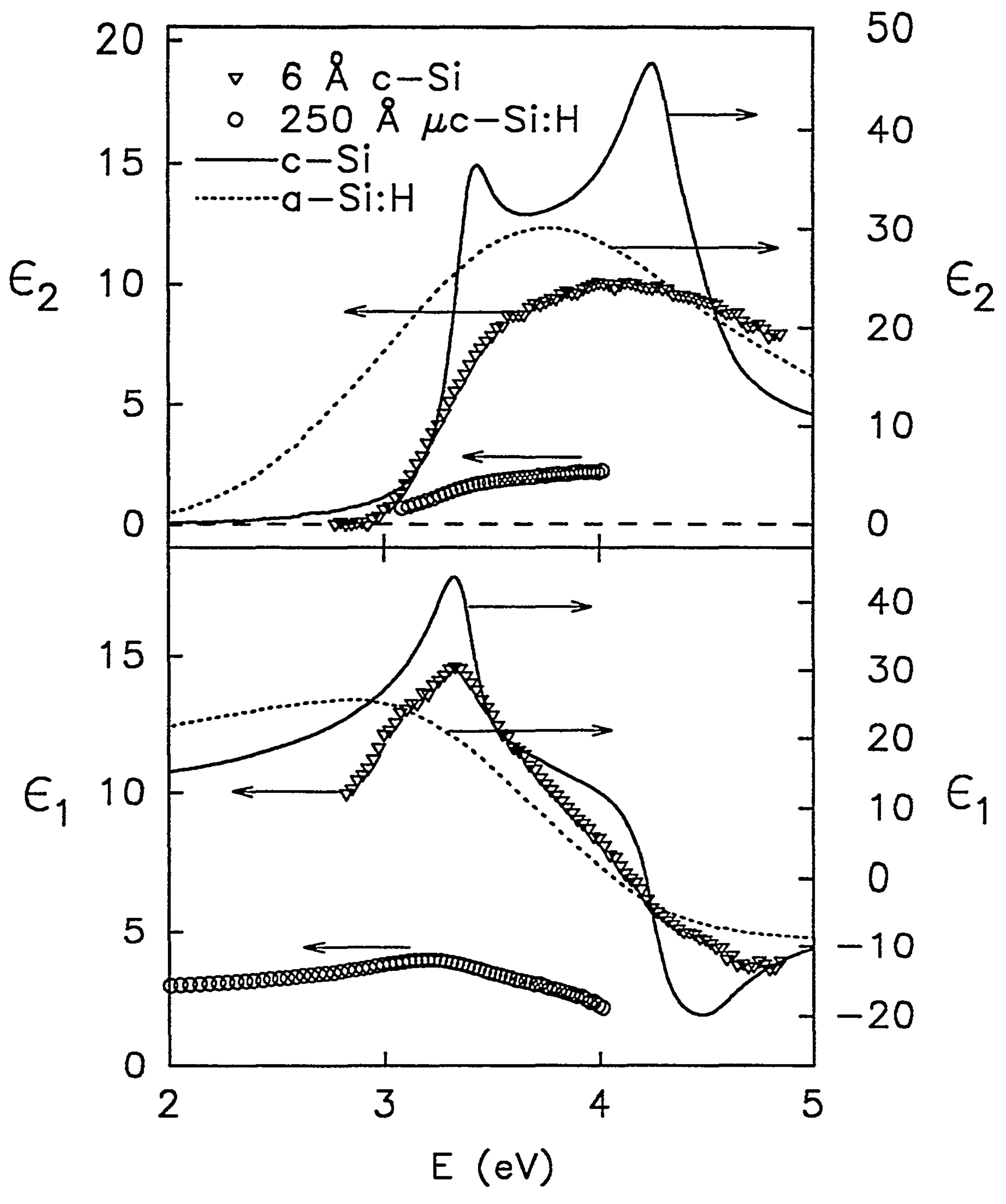

Figure 30. Dielectric function for 6 Å single-phase μc-Si:H prepared onto a Cr substrate in the growth/etching process (triangles). Also shown for comparison are the dielectric functions for: bulk c-Si (solid lines, left scale), bulk a-Si:H (broken lines, left scale), and a 250 Å thick, single-phase μc-Si:H film prepared by PECVD using a 1/80 gas flow ratio of SiH_4/H_2 (circles). All results were obtained ex situ at 25°C except those of the PECVD μc-Si:H which was measured in real time during growth at 250°C.

In order to obtain the μc-Si:H film whose dielectric function appears in Fig. 30 (triangles), etching was terminated in the one-layer regime under RTSE control. The film was transported and measured ex situ under N_2 using a single-channel ellipsometer with a wider spectral range. H-coverage of the film surface may also protect it from oxidation. The dielectric function of the μc-Si:H film was deduced by inversion of the ex situ (ψ, Δ) spectra, choosing the thickness (6 Å) to ensure that ε_2 vanishes at the lowest photon energy of 1.5 eV. The ~0.5 void volume fraction in the ultrathin film accounts for the low amplitude of its dielectric function in comparison with bulk c-Si (solid line; left scale; Aspnes and Studna, 1983). Further comparison of these dielectric functions reveal two common characteristics, suggesting that the ultrathin film is indeed single-phase μc-Si:H. First, ε_2 shows a sharp absorption onset near 3 eV, and second, there is a well-defined feature, clearest in ε_1 at the position of the E_0'-E_1 critical point complex of c-Si. Both characteristics are absent in thick (broken line) and ultrathin a-Si:H. It is surprising that a 6 Å film of μc-Si:H shows such a well-defined critical point feature. The feature observed here may be attributed to a bound excitonic contribution within the E_0-E_1' complex that remains as other contributions are broadened (Lautenschlager et al., 1987).

The key point of this study, however, is the comparsion in Fig. 30 between the dielectric function of the 6 Å μc-Si:H film prepared by etching (triangles) and a 250 Å thick single-phase μc-Si:H film prepared by PECVD on an identically-prepared Cr substrate (circles). The large difference in the amplitude of the dielectric functions is attributed to a void volume fraction of 0.9 in the PECVD film, arising from the free space between isolated microcrystals. Obviously the morphology of the two films are controlled by different factors. For the ultrathin film, the microcrystallites nucleate from the solid phase within an a-Si:H matrix, whereas for the PECVD film, they nucleate from the gas phase onto the Cr substrate. Thus, if a material serves as a good substrate for a-Si:H deposition, it can also be used as a substrate for preparation of ultrathin μc-Si:H. A key issue, however, is the ability to terminate the etching process at the precise time to leave a thin layer of μc-Si:H at the interface, perhaps bonded by a residual monolayer or more of a-Si:H. Thus, real-time monitoring and control is invaluable in this application, as it avoids extensive empirical investigations.

We have prepared ultrathin μc-Si:H films by etching relatively thick a-Si:H (150-200 Å). In this way, the microstructural evolution shown in Fig. 29 could be readily deduced. In device applications, one can start with a much thinner film (30-50 Å). This reduces the etch time and places less stringency on the macroscopic uniformity of the etching process. We emphasize that a thin and dense layer of μc-Si:H at the substrate interface, by itself, is not particularly useful technologically. However, this layer can be used to enhance nucleation of PECVD μc-Si:H on substrates that provide unacceptably low nucleation rates, but the procedure is not trivial. It has been found that a single 10 Å layer of μc-Si:H is etched away if exposed to the SiH_4/H_2 plasma used in PECVD. Thus, one needs to repeat the growth/etch sequence a number of times to generate a thicker (~50 Å) μc-Si:H layer; then PECVD can be used the complete the film. A desirable feature of the filament in comparison to a H_2 plasma, is the layer-by-layer etching characteristic of the former process.

Finally, the growth/etching approach for preparing μc-Si:H layers is most successful if the deposition system is free of C and O. If the surface of the film becomes contaminated during etching, diffusion of thermal H is blocked and etching gradually ceases (An et al., 1993). Thus, for wide-gap μc-Si:C:H alloy preparation, the C can only be introduced in the PECVD stage.

In conclusion, we have studied single cycles consisting of a-Si:H growth on a Cr substrate, followed by etching with thermally-generated atomic H to prepare ultrathin layers (<15 Å) of μc-Si:H. Real-time monitoring provides monolayer-level endpoint detection in this process and allows one to identify the phase-purity of the residual crystalline layer on the substrate. The advantage of the growth/etch processing demonstrated here is the ability to obtain a high density μc-Si:H phase as a nucleation promoter at the substrate interface for substrates onto which conventional PECVD μc-Si:H will not readily nucleate.

6. a-Si:H-Based Solar Cell Preparation

In this section, we will describe the current status of solar cell development at Penn State under Phase III of our research program. This research can be divided into two areas. First, cell preparation in a single-chamber system under RTSE monitoring and control will be described in Sec. 6.1. At present, the (single-chamber deposition)/(real-time spectroscopic ellipsometer) facility does not have the capability of depositing n-layers. Thus, p-i structures are prepared and monitored, then transferred under N_2 gas to the multichamber system for completion of the device. Second, cell preparation in the multichamber system will be described in Sec. 6.2. In this case, the p, i, and n-layers are deposited in separate chambers. In spite of the fact that there is no real-time monitoring on the multichamber deposition system, we coordinate closely our materials and device studies for the two facilities. In this way, insights deduced from the single-chamber real-time monitoring can be applied in an attempt to improve materials, interfaces, and devices prepared in the multichamber system.

6.1 *Monitoring Solar Cell Preparation in a Single-chamber System*

Next, we focus on RTSE analysis of the two interfaces (SnO_2/a-SiC:H:B and a-SiC:H:B/a-Si:H) that are generated in the preparation of the p-i structure. In each case, the substrate exhibits roughness on a scale that is comparable to or larger than the scale of thin film nucleation. When this is the case, then the nucleation process cannot be characterized. [For this reason ultrasmooth substrates such as Si wafers or ion-beam sputtered metal films were used as substrates in the nucleation studies of Phase II (Collins et al., 1994a).] Figure 31 shows a simple structural schematic of film growth on a rough substrate, and the optical model that simulates the structure is also shown. As a result, relatively complex optical models are needed to characterize the process of interface formation with rough substrates. These models simulate the conformal coverage of the substrate with nuclei that increase in size and coalesce. Even after coalescence, considerable roughness remains on the film, having been induced by the extensive roughness on the substrate.

6.1.1 Growth of a-SiC:H:B on SnO_2

Figure 32(a) shows microstructural data that characterize a-SiC:H:B growth on SnO_2, as determined by RTSE during single-chamber solar cell preparation. No metal or dopant contamination is detected at the SnO_2/p-layer interface for this run, since minimal H_2 dilution is used (R=0.1) and the plasma is ignited <1 min. after introduction of the p-layer gas. In this p-layer deposition, p-type gas flow ratios of CH_4:SiH_4:H_2:B_2H_6= 4:6:1:0.01 were employed with a pressure of 0.2 Torr. The substrate temperature and rf plasma power were 250°C and 3 W, respectively. This led to p-type material with optical gap and activation energies of 1.85 eV and 0.48 eV, respectively.

Because the SnO_2 surface has an estimated 92 Å of microscopic roughness, a three-layer structure for the a-SiC:H:B film is needed to model the full RTSE data set [see Figs. 31 and 32(b)]. The layers include (from the bottom to the top of the film): (i) a SnO_2/a-SiC:H:B interface roughness layer with a fixed thickness (d_i) of 92 Å, (ii) an a-SiC:H:B bulk layer (thickness: d_b), and (iii) a substrate-induced roughness layer on the a-SiC:H:B surface (thickness: d_s). In Figs. 32(a) and (b), three regimes are identified: (1) prior to plasma ignition; (2) after plasma ignition but prior to bulk layer formation, and (3) after bulk layer formation. In regime (2), the voids in the SnO_2 roughness layer fill with a-SiC:H:B [volume fraction: f_i, see lower panel in Fig. 32(a)] to form the interface layer, and the surface roughness layer develops as the a-SiC:H:B nuclei cover the SnO_2 conformally. In regime (3), the interface layer has stabilized, a bulk layer develops and increases in thickness linearly with time, and the substrate-generated surface roughness on the a-SiC:H:B smoothens versus time. When the plasma is extinguished, we have an accurate estimate of the p-layer microstructure: d_i=92 Å, d_b=156 Å, d_s= 66 Å. This corresponds to an effective single-layer thickness (or mass thickness) of d_m = 156 + 0.5(92+66) Å = 235 Å. In further cell preparations, this layer thickness will be decreased.

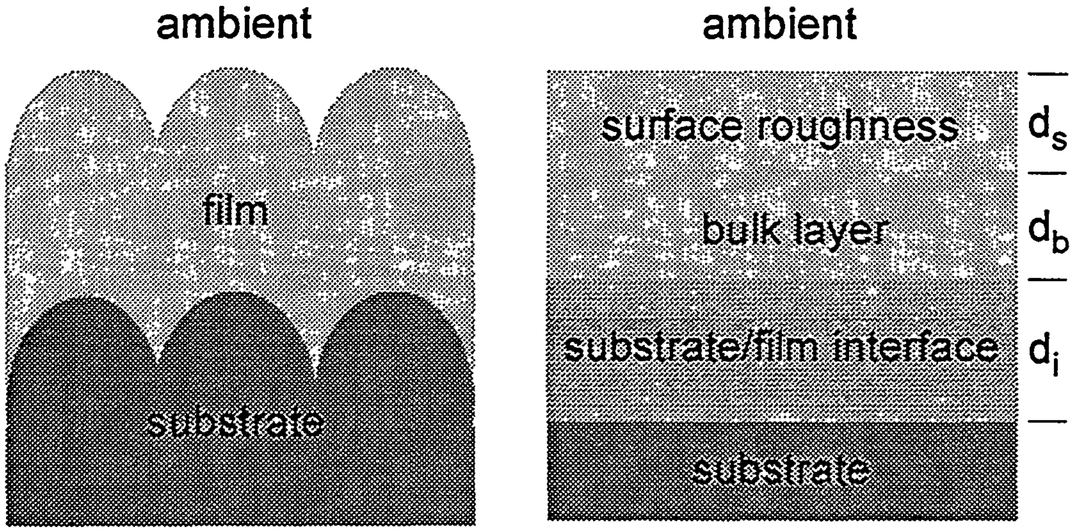

Figure 31. A simple structural schematic of growth on a rough substrate (left), and the optical model that simulates the microstructure.

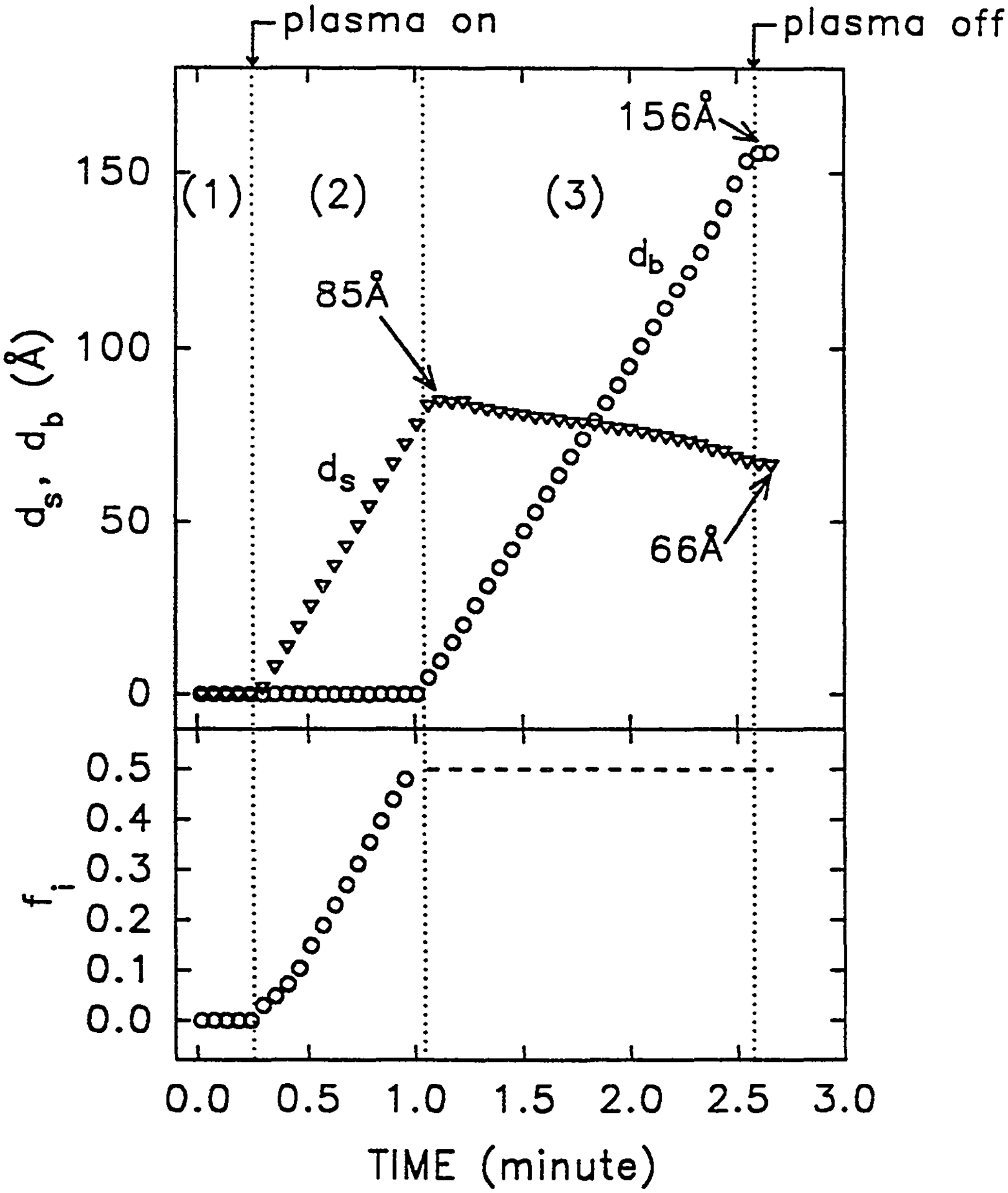

Figure 32(a). Experimental parameters deduced from RTSE that characterize the microstructural evolution of p-type a-SiC:H on a specular SnO_2 substrate. Overall, a three-layer model for the a-SiC:H:B film is required to interpret the RTSE data. In regime (1), the plasma has yet to be ignited and a 92 Å thick roughness layer is present of the SnO_2. Plasma ignition defines the onset of regime (2). In this regime, a fixed-thickness (d_i=92 Å) interface roughness layer develops from the SnO_2 surface roughness. The SnO_2/a-SiC:H:B interface layer is modeled during regime (2) as a physical mixture of SnO_2 (volume fraction: 0.50), a-SiC:H:B (volume fraction: f_i), and void. The lower panel describes the filling of the SnO_2 roughness by a-SiC:H using this model. In regime (2), a roughness layer modeled as a physical mixture of a-SiC:H and void (thickness: d_s) develops as the SnO_2 is covered conformally with nuclei and/or bulk film. The onset of regime (3) is identified when the roughness in the SnO_2 layer is completely filled by a-SiC:H, forming a layer with 0.5/0.5 physical mixture of SnO_2/a-SiC:H. After that point, a bulk-density a-SiC:H:B layer (thickness: d_b) evolves and increases linearly in thickness until termination of the deposition. In this regime, the roughness on the a-SiC:H layer smoothens from an intial thickness of 85 Å to a final thickness of 66 Å.

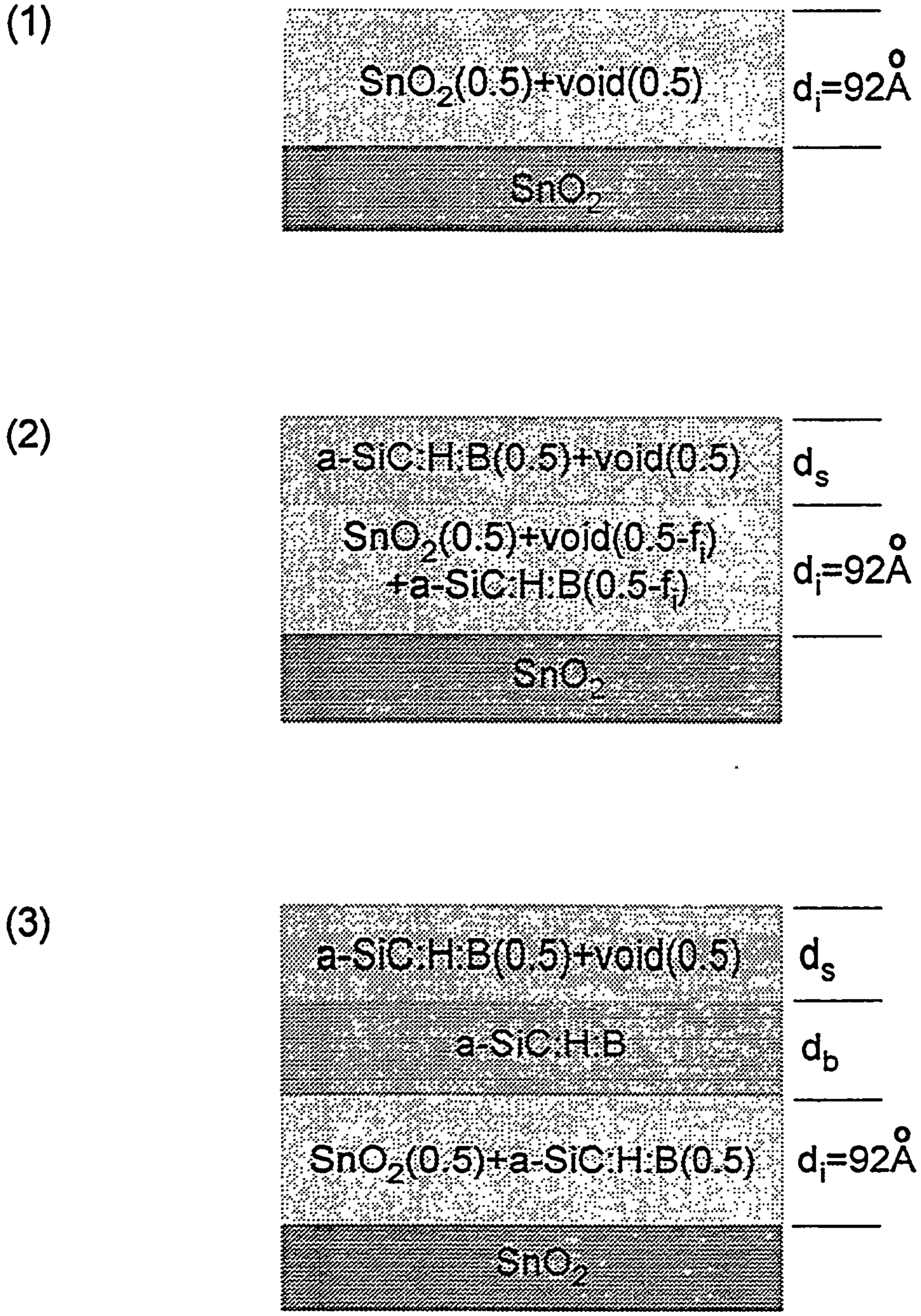

Figure 32(b). Schematic multilayer structures that characterize the microstructural evolution for p-type a-SiC:H growth on specular SnO_2. Overall, a three-layer model for the a-SiC:H:B film is required to interpret the RTSE data. In regime (1) (top), the plasma has yet to be ignited and a 92 Å thick roughness layer is present of the SnO_2. Plasma ignition defines the onset of regime (2) (center). In this regime a fixed-thickness (d_i=92 Å) interface roughness layer develops from the SnO_2 surface roughness. The SnO_2/a-SiC:H:B interface layer is modeled during regime (2) as a physical mixture of SnO_2 (volume fraction: 0.50), a-SiC:H:B (volume fraction: f_i), and void. In regime (2), a roughness layer modeled as a physical mixture of a-SiC:H and void (thickness: d_s) develops as the SnO_2 is covered conformally with nuclei and/or bulk film. The onset of regime (3) (bottom) is identified when the roughness in the SnO_2 layer is completely filled by a-SiC:H, forming a layer with 0.5/0.5 physical mixture of SnO_2/a-SiC:H. After that point, a bulk-density a-SiC:H:B layer (thickness: d_b) evolves.

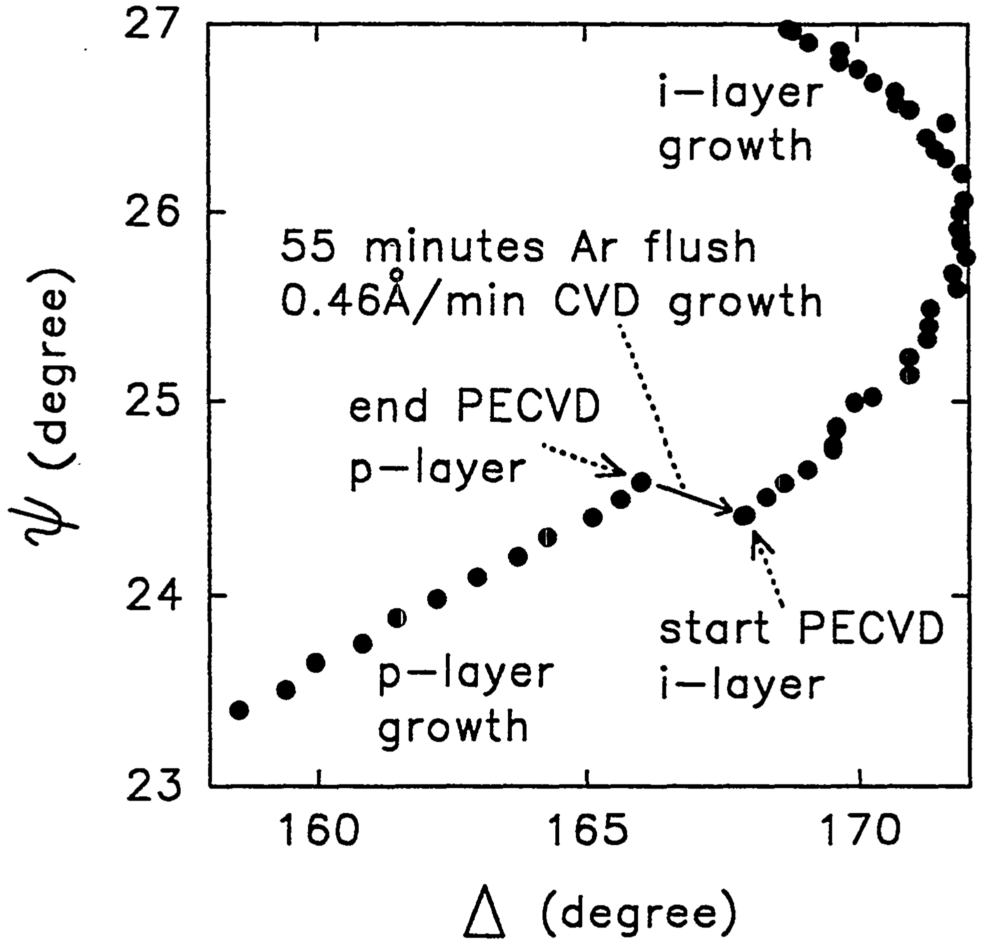

Figure 33. Real-time ellipsometry (ψ, Δ) trajectory obtained at 2.52 eV during formation of the p/i interface for the solar cell deposition of Fig. 31 (in a one-chamber system). Spectra were collected every 1 s as (i) the p-layer deposition was terminated, (ii) the p-type gas (CH_4:SiH_4:H_2:B_2H_6= 4:6:1:0.01) was evacuated from the chamber, (iii) the chamber was purged with Ar gas, (iv) the i-layer gas was stabilized, and (v) the plasma was ignited for i-layer growth. During (ii)-(iii) (a total of 55 min.), 25 Å thick layer of a heavily B-contaminated CVD material forms at the p-i interface (arrow).

Figure 33 shows the ellipsometric (ψ, Δ) trajectory at 2.52 eV during formation of the p/i interface of the same device as was studied in Fig. 32. First, the p-layer plasma is extinguished, and the ($CH_4/SiH_4/H_2/B_2H_6$) gas mixture is evacuated and replaced with Ar flushing gas. During this process, and during 55 min. of flushing and i-layer gas stabilization, a 25 Å CVD layer forms on the surface of the p-layer (Collins, 1988). This B-contamination is buried at the interface when the i-layer is deposited. This contamination is important not only in single-chamber depositions, but also in multichamber depositions. In the latter case, the p-layer chamber is generally purged with an inert gas (in the same way) prior to in-vacuum transfer of the sample to the i-layer chamber. Although purging prevents cross-contamination of the chambers during transfer, the process ultimately contaminates the p-layer surface with boron. The next part briefly describes a model study in a single-chamber system that has provided greater insights into the rate of contamination of the p-layer surface under the p-layer conditions used in our single- and multiple- chamber reactor systems.

6.1.2 P-i Interfaces

In a model study, we have quantified the B-contamination that occurs via CVD in the formation of the p-i interface. This effect is expected to be important in single- and multiple-chamber solar cell preparation because B_2H_6 will decompose on the p-layer surface in the time between extinguishing the p-layer plasma and evacuating the gas. As shown in Fig. 33, however, the CVD effect continues even while flushing the chamber with an inert gas (after the p-layer gas is evacuated from the chamber). Thus, it appears that the B_2H_6 is adsorbed on the chamber walls and desorbs during the flushing process.

In the experiment of Fig. 34, an opaque a-SiC:H p-layer (3200 Å) is first prepared by PECVD using a 0.1% doping gas flow ratio (B_2H_6/SiH_4), and is then exposed to the same gas after extinguishing the plasma. Throughout the process the substrate temperature is maintained at 250°C. Growth of a-SiB:H by CVD occurs during the gas exposure period.

Figure 34(a) shows the experimental parameters deduced from RTSE during the growth of a-SiB:H on a-SiC:H:B in the CVD process (i.e., in the absence of plasma excitation). Figure 34(b) provides the schematic multilayer structures that characterize the microstructural evolution of the CVD layer. Overall, a two-layer model for the growth of the CVD film is required to interpret the RTSE data. In regime (1), the p-type a-SiC:H film is being deposited by PECVD. Plasma extinction (while maintaining the p-layer gas flow) defines the onset of regime (2). In this regime a fixed-thickness (d_i=16 Å) interface roughness layer develops between PECVD and CVD layers, originating from the final 16 Å surface roughness layer on the PECVD film. The PECVD/CVD interface layer is modeled during regime (2) as a physical mixture of PECVD

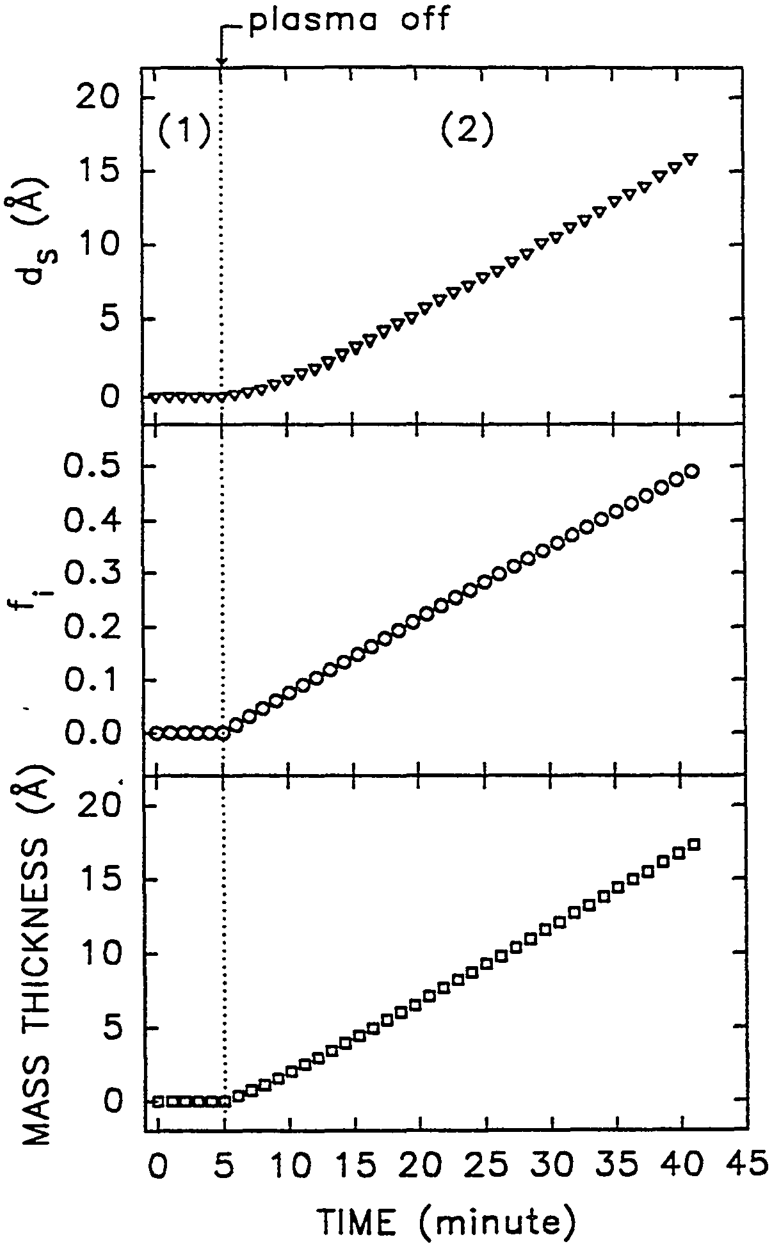

Figure 34(a). Experimental parameters deduced from RTSE that characterize the microstructural evolution during the growth of a-SiB:H on a-SiC:H:B by a CVD process in the absence of plasma excitation. In this case, an a-SiC:H p-layer is initially prepared by PECVD using a 0.1% doping gas flow ratio (B_2H_6/SiH_4), and is then exposed to the same gas after extinguishing the plasma. This gas exposure leads to growth by CVD. Overall, a two-layer model for the growth of the CVD film is required to interpret the RTSE data. In regime (1), the p-type a-SiC:H film is being deposited by PECVD. Plasma extinction defines the onset of regime (2). In this regime a fixed-thickness (d_i=16 Å) interface roughness layer develops between PECVD and CVD layers, originating from the surface roughness on the PECVD film. The PECVD/CVD interface layer is modeled during regime (2) as a physical mixture of PECVD material (volume fraction: 0.50), CVD material (volume fraction: f_i), and void. The center panel describes the filling of the voids in the PECVD film roughness by CVD material using this model. Also in regime (2), a roughness layer modeled as a physical mixture of the CVD material and void (thickness: d_s) develops as the PECVD film is covered conformally with CVD nuclei and/or bulk material. The lower panel shows the mass thickness of the deposited CVD material; this is the critical parameter that quantifies the interface contamination.

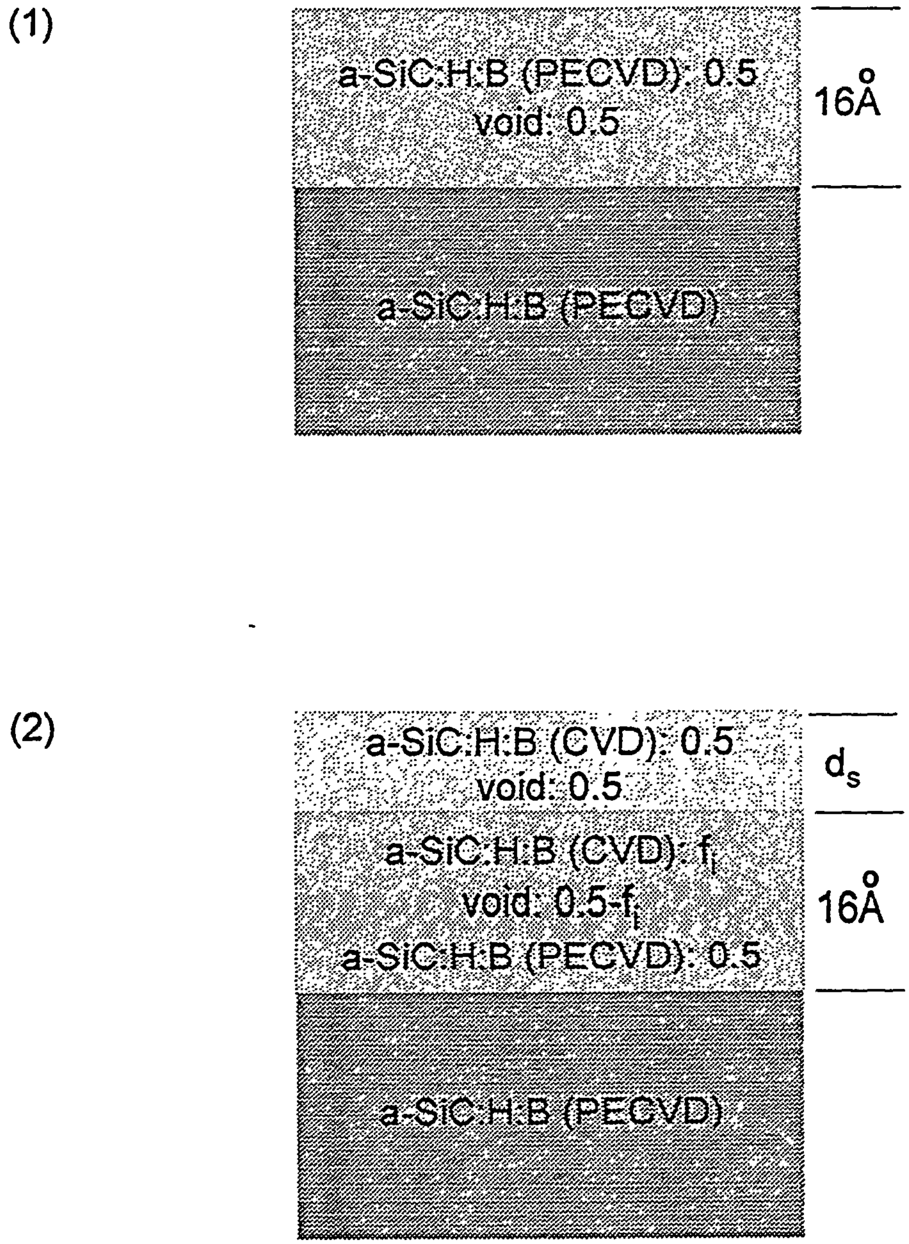

Figure 34(b). Schematic multilayer structures that characterize the microstructural evolution during the growth of a-SiB:H on a-SiC:H:B by a CVD process in the absence of plasma excitation. In this case, an a-SiC:H p-layer is initially prepared by PECVD using a 0.1% doping gas flow ratio (B_2H_6/SiH_4), and is then exposed to the same gas after extinguishing the plasma. This gas exposure leads to growth by CVD. Overall, a two-layer model for the growth of the CVD film is required to interpret the RTSE data. In regime (1) (top), the p-type a-SiC:H film is being deposited by PECVD. Plasma extinction defines the onset of regime (2) (bottom). In this regime a fixed-thickness (d_i=16 Å) interface roughness layer develops between PECVD and CVD layers, originating from the surface roughness on the PECVD film. The PECVD/CVD interface layer is modeled during regime (2) as a physical mixture of PECVD material (volume fraction: 0.50), CVD material (volume fraction: f_i), and void. Also in regime (2), a roughness layer modeled as a physical mixture of the CVD material and void (thickness: d_s) develops as the PECVD film is covered conformally with CVD nuclei and/or bulk material.

material (volume fraction: 0.50), CVD material (volume fraction: f_i), and void (volume fraction $0.5-f_i$). The center panel in Fig. 34(a) describes the filling of the voids in the PECVD film roughness by CVD material using this model. Also in regime (2), a roughness layer modeled as a physical mixture of the CVD material and void (thickness: d_s) develops as the PECVD film is covered conformally with the CVD nuclei and/or coalesced film material. The top panel in Fig. 34(a) shows the development of this layer.

The lower panel in Fig. 34(a) shows the mass thickness of the deposited CVD material. This is the critical parameter that quantifies the interface contamination. The rate at which CVD growth occurs during exposure of the a-SiC:H:B to the p-type gas mixture (CH_4:SiH_4:H_2:B_2H_6= 4:6:1:0.01, in sccm) is ~0.5 Å/minute, as estimated by the slope of the linear relationship in the lower panel. Although this seems like a very thin layer, if each B atom contributes a gap state, it averages to an effective defect density of ~10^{20} cm^{-3} over a full 200 Å p-layer.

In a similar analysis, we have also determined the optical properties of the CVD a-SiB:H at the substrate temperature of 250°C. This provides information of the effectiveness of the ultrathin contaminant layer to trap holes in gap states at the p-i interface. Again flow ratios of CH_4:SiH_4:H_2:B_2H_6 =4:6:1:0.01) and a pressure of 0.2 Torr were used in this study.

In Fig. 35(a), real and imaginary parts of the optical functions for the CVD material are presented, collected in real time and corrected for the effects of surface roughness (in order to obtain an accurate gap value). In Fig. 35(b), we present the optical gap plots for the CVD and PECVD material prepared from the same gas mixture. Because these measurements were collected in real time, the optical gap is obtained at the deposition temperature (250°C) using the $\varepsilon_2^{1/2}$ extrapolation. The effects of elevated temperature and constant dipole-matrix element gap extrapolation lead to a 0.25 eV narrower gap than the room temperature Tauc (or contant momentum matrix-element) gap extrapolation. Thus, the room temperature Tauc gap of the CVD material is predicted to be ~1.5 eV. The Tauc optical gap of the CVD material, obtained in a second experiment is found to be quite close ~1.45 eV, or 0.4 eV lower than the a-SiC:H:B. Such a thin, narrow-gap material at the p-i interface is expected to reduce the open-circuit voltage of the cell; however, the magnitude of the problem is an extremely senstive function of the preparation procedure. Solar cell modeling is now being undertaken to understand the effects of such layers on the device parameters.

6.1.3 Single-chamber Cell Performace

As noted above, the single-chamber system employed in this research is configured to allow monitoring of solar cell preparation by RTSE. Because only p- and i-layer deposition capabilities exist, the device is completed with a μc-Si:H n-layer in the multi-chamber system. The μc-Si:H:P

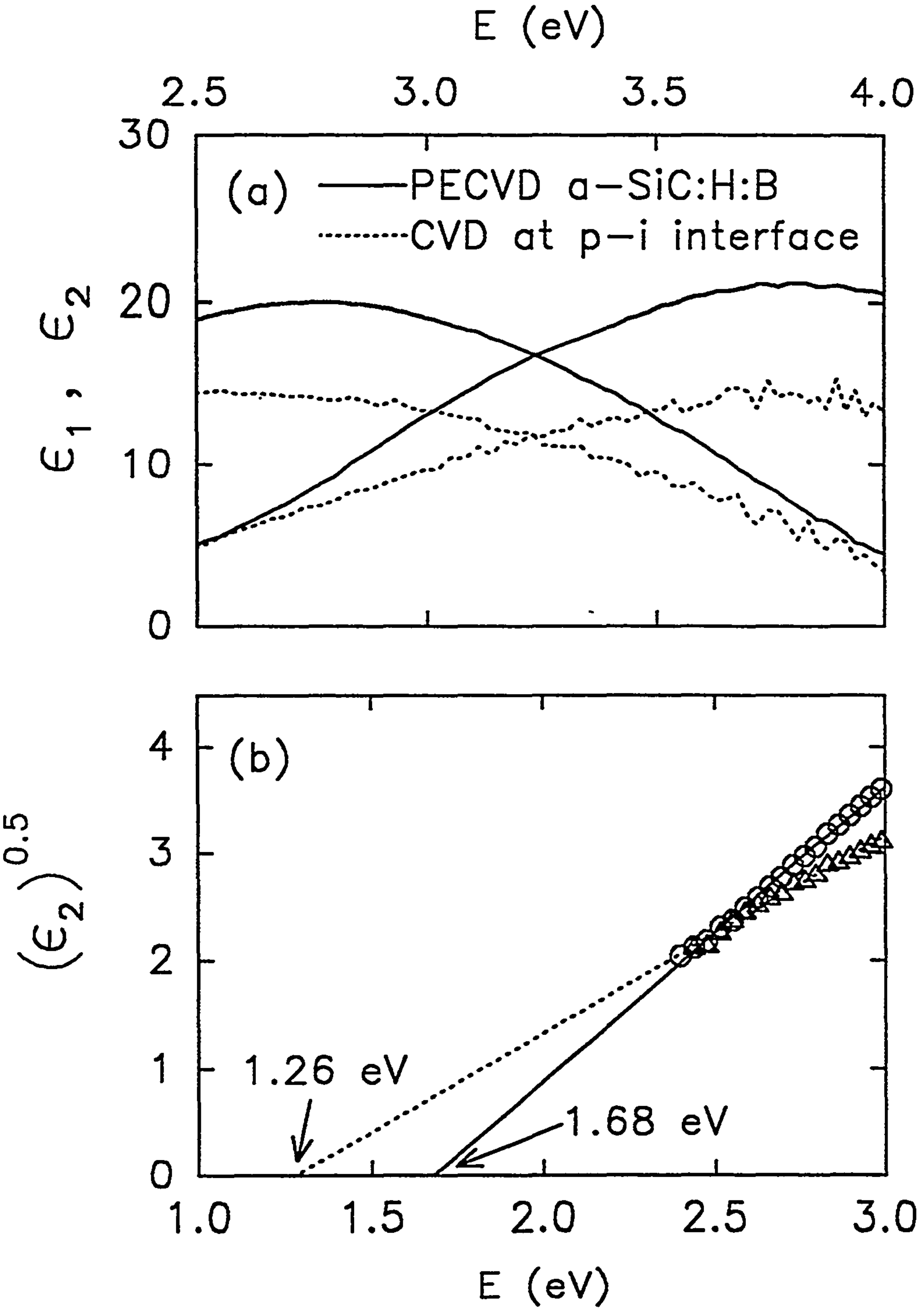

Figure 35. Optical properties of a-SiB:H deposited by CVD in the absence of a plasma by exposing a p-type a-SiC:H substrate film to the p-type gas mixture, having flow ratios of (CH_4:SiH_4:H_2:B_2H_6=4:6:1:0.01) and a pressure of 0.2 Torr. (a) Real and imaginary parts of the dielectric functions for the CVD material (corrected for surface roughness); (b) determination of the optical gaps for CVD and PECVD material prepared from the same gas mixture. The optical gap is obtained at the deposition temperature using the $\varepsilon_2^{1/2}$ extrapolation. The effects of substrate temperature (250°C) and gap extrapolation lead to a 0.25 eV narrower gap than the room temperature Tauc gap. Thus, the room temperature Tauc gap of the CVD material is expected to be ~1.5 eV.

layer is deposited at the back of the cell in an attempt to eliminate any contaminants on the i-layer surface through the etching that occurs in the initial nucleation of the crystallites. Such contaminants may form during transfer of the p-i structure from the single-chamber reactor to the multichamber one. We have performed extensive studies demonstrating that the resulting cell performance is not adversely impacted by possible i/n interface problems that may arise from the transfer. Such studies have involved fabricating two cells in the multichamber system, a control cell prepared using in-vacuum transfer between i- and n-layers, and a test cell which is prepared under identical conditions except that it is removed from the chamber between preparation of the i- and n-layers. Between the i- and n-layer preparations the test cell is handled in the same way as would be a p/i structure from the single-chamber system. The handling process and n-layer deposition were designed so that the control and test cells exhibited no measurable performance differences.

In our study of TCO/p/i preparation, we employ three types of substrates: specular SnO_2- and ZnO-coated glass for solar cells, and SnO_2-coated Si for RTSE. This latter structure is used to enhance the sensitivity of RTSE. The assumption in these studies is that the growth and interface characteristics of a-SiC:H:B are the same for SnO_2/glass and SnO_2/c-Si structures.

Characterization of the solar cells deposited on the both ZnO and SnO_2 TCO's in this run yield identical performances with initial efficiencies of ~5%. This result suggests that the TCO/p interface is not limiting the cell performance; however, the contamination observed by RTSE at the p/i interface may play a key role. Present efforts are being devoted to correlating the RTSE characteristics of the interface with the cell performance. Buffer layers and p-layer growth using $B(CH_3)_3$ dopant gas will both be explored.

Table VI provides a summary of the interface effects uncovered in this study, and believed to be important in solar cell preparation. We include the magnitudes of the various effects, as deduced from our RTSE studies using a single-chamber system. These should be considered only as a rough guide to the reader, since such effects are expected to be very sensitive to the design of the growth reactor.

6.2 *Multichamber Cells*

In a first attempt, a solar cell with a 7.7% initial efficiency has been prepared in our multi-chamber system. As shown by the results in Figure 36, the following characteristics were obtained: fill-factor, 0.72; open-circuit voltage, 0.82 V; and short-circuit current, 13.1 mA/cm^2. The TCO was textured SnO_2, and the p-layer was 200 Å thick a-SiC:H:B with a band gap of 1.85 eV and a conductivity activation energy of 0.53 eV. No H_2 dilution was used in the preparation of the p-layer. The i-layer was prepared to 0.6 μm using a-Si:H growth conditions that include

Table VI: Interface Effects in Solar Cell Preparation

TCO/a-SiC:H Interfaces		
ZnO/a-SiC:H Interface Formation		
250°C, intrinsic H_2 dilution, R=20	H penetration	8x10^{19} cm^{-3} electrons 0.07 eV F.L. shift 300 Å penetration of H
250°C, p-type 0.1% min H_2 dilution, R=0.1	H/B penetration	>10^{20} cm^{-3} electrons 0.1-0.2 eV F.L. shift 100 Å penetration of H <50 Å penetration of B
SnO_2/a-SiC:H Interface Formation		
250°C, intrinsic H_2 dilution, R=20	SnO_2 reduction	5 Å mass thickness free metal (Sn)
SnO_2/a-SiC:H Interface Formation		
250°C, p-type min H_2 dilution, R=0.1	SnO_2 reduction	< 0.5 Å mass thickness free metal (Sn)
Exposure of TCO's to p-Type Gas		
SnO_2 Exposure 250°C, p-type gases CH_4:SiH_4:H_2:B_2H_6 = 4:6:1:0.01	B-contamination	0.03 Å/min
ZnO Exposure 250°C, p-type gases CH_4:SiH_4:H_2:B_2H_6 = 4:6:1:0.01	B-contamination	<0.008 Å/min
Exposure of p-Layer to p-Type Gas		
a-SiC:H:B Exposure 250°C, p-type gases CH_4:SiH_4:H_2:B_2H_6 = 4:6:1:0.01	B-contamination	0.5 Å/min
Exposure of p-Layer to System Clean After p-Layer Deposition		
a-SiC:H:B @ 250°C, Ar gas flush: 60 min	B-contamination	0.5 Å/min

Table VI. Summary of interface effects relevant for a-Si:H-based solar cell preparation.

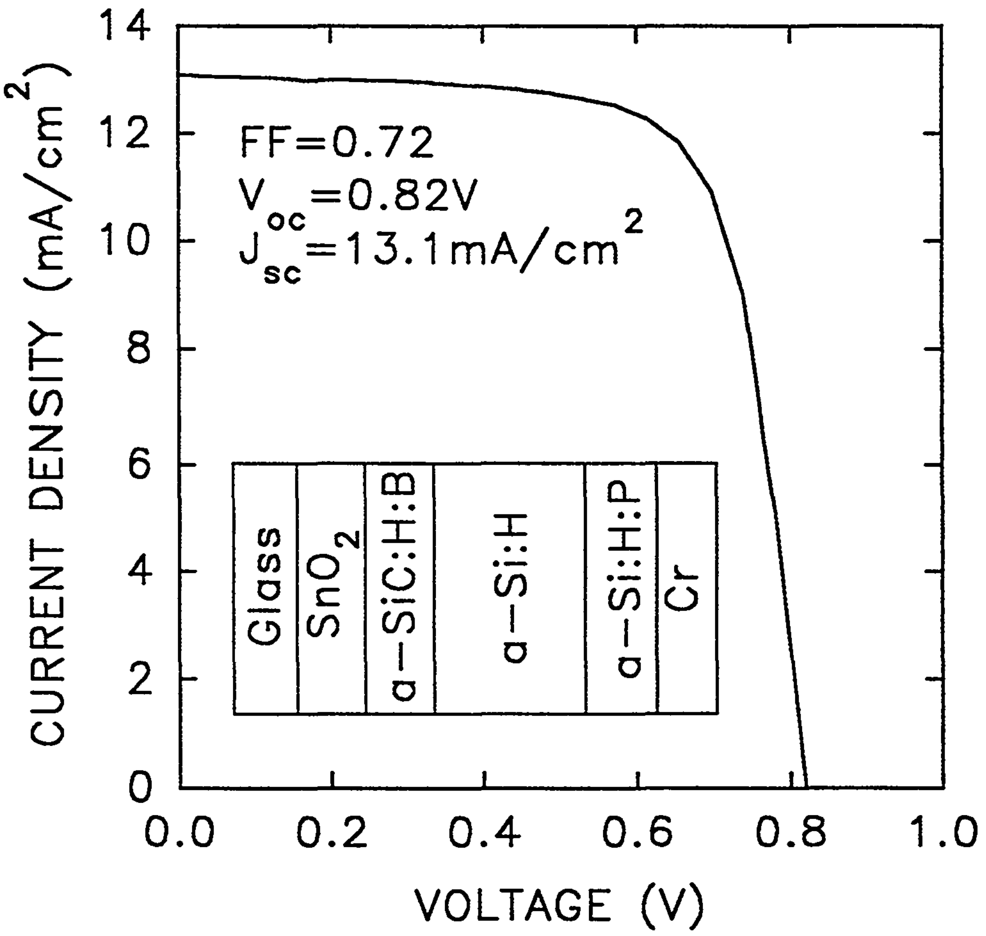

Figure 36(a). Initial current-voltage characteristic for a baseline mid-gap solar cell prepared in the multichamber system. A 200 Å a-SiC:H:B p-layer was prepared onto textured SnO_2 at a substrate temperature of 240°C without H_2-dilution (R=0). A 0.3% $B_2H_6/(SiH_4+CH_4)$ doping gas flow ratio and a 1.86:1 (in sccm) SiH_4/CH_4 alloy gas flow ratio were used for the p-layer. The 6000 Å a-Si:H i-layer was prepared at 200°C from pure SiH_4. The structure was completed with a 300 Å n-layer and a Cr back contact. No procedures were used to enhance reflection or scattering from the back contact.

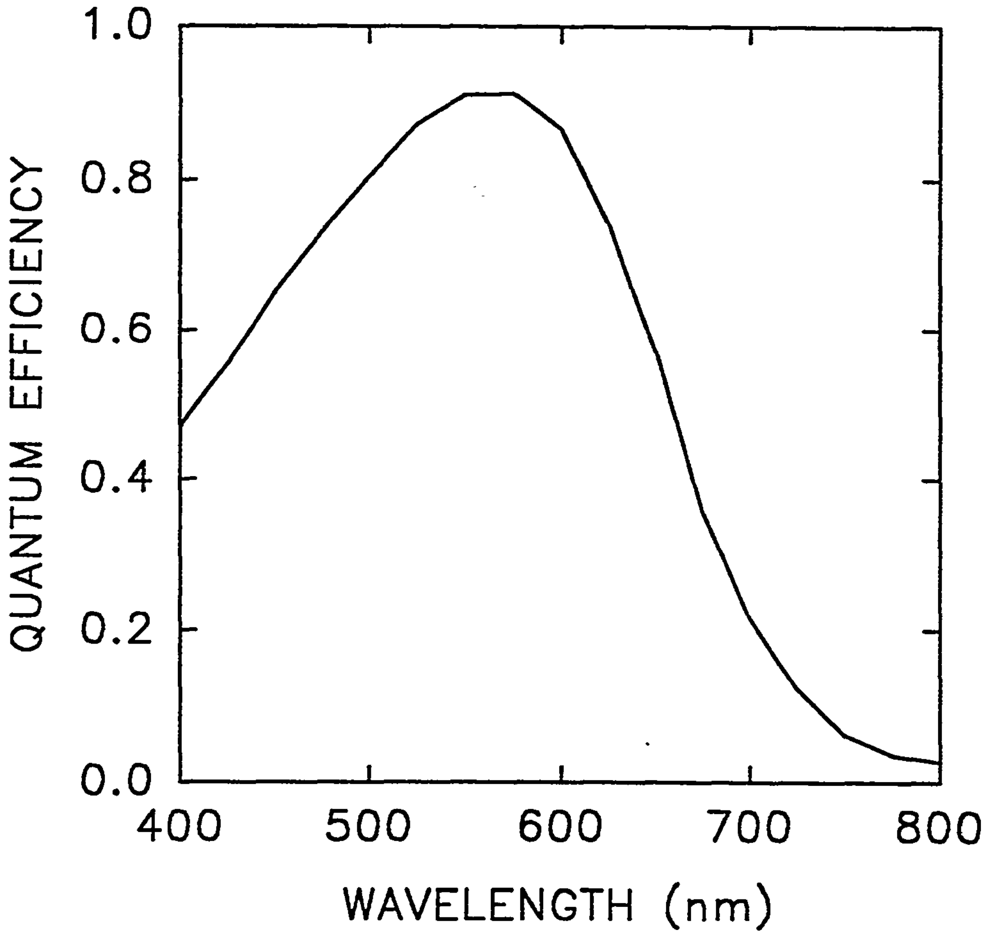

Figure 36(b). Initial quantum effciency versus wavelength for a baseline mid-gap solar cell prepared in the multichamber system. A 200 Å a-SiC:H:B p-layer was prepared onto textured SnO_2 at a substrate temperature of 240°C without H_2-dilution (R=0). A 0.3% $B_2H_6/(SiH_4+CH_4)$ doping gas flow ratio and a 1.86:1 (in sccm) SiH_4/CH_4 alloy gas flow ratio were used for the p-layer. The 6000 Å a-Si:H i-layer was prepared at 200°C from pure SiH_4. The structure was completed with a 300 Å n-layer and a Cr back contact. No procedures were used to enhance reflection or scattering from the back contact.

no silane dilution and a substrate temperature of 200°C. The n-layer was 300 Å thick. No special procedures were performed at the TCO/p and p/i interfaces; thus, this cell is considered a "baseline" mid-gap cell. In the future, we intend to explore the effects of a number of growth parameters/procedures on the characteristics of this cell. These include studies of the effects of the following: (i) varying levels of H_2 dilution of the p-layer gas, designed to generate interfacial free metal layers of different mass thickness; (ii) undoped a-SiC:H buffer layers at the p/i interface, deposited continuously after the p-layer in order to avoid CVD B-contamination; (iii) p-layers prepared by $B(CH_3)_3$, also to avoid CVD; and (iv) filament-generated atomic H-treatment at p/i interface to passivate defects.

7. Future Work

Future investigations will continue under a new subcontract with the National Renewable Eneregy Laboratory. The future directions enumerated in this section are confined to those topics that have been motivated by the present Phase III investigations. The numbers below correspond to the topics described in the Executive Summary at the beginning of this report.

(1) In Phase II-III, we optimized a-SiC:H alloys for use as the intrinsic layer of wide-gap solar cells, in accordance with the goals of the wide-gap team. We have carefully studied the effects of H_2 dilution on both the structure and photoelectronic properties of the alloys, and have established meaningful correlations and recommendations. The effects of substrate temperature, pressure, power, and gas flows on the microstructure have also been studied, but correlations with the photoelectronic properties need to be established definitively. In the next research period, we will determine the photoelectronic properties of the optimum 1.90-2.00 eV gap a-SiC:H alloys prepared in both single- and multi-chamber systems. Optimization will be performed through variations in the substrate temperature, pressure, power, and gas flows and will be expedited through microstructural information established in RTSE studies. Similar research will be performed on unalloyed a-Si:H using high H_2-dilution and reduced substrate temperature in order to achieve the wider gap. Comparisons between the results for alloyed and unalloyed intrinsic layers will lead to recommendations for wide-gap solar cells, based on AMPS modeling.

(2-4) Conventional 200 Å unalloyed a-Si:H:B p-layers will be hydrogenated using filament methods in order to generate wide-gap p-layers (1.95 eV) according to the process described in Sec. 2.2. The electrical transport in the resulting films will be characterized to determine if this processing step is detrimental to the conductivity of the p-layer. For example, it is possible that the additional incorporated H will passivate the dopant atoms, making the process unsuitable in the preparation of solar cells. Further studies will also be done to determine the depth to which the p-layer can be crystallized when a much higher atomic H flux is utilized. Any such methods deemed to be promising will be incorporated into p-i-n solar cells in the superstrate configuration, and then compared to our baseline control cells.

(3-4) In comparing interfaces, it is interesting to note that free metal forms at the SnO_2/a-SiC:H:B interface, and the interface resistance in this case is relatively low; free metal does not form at the ZnO/a-SiC:H:B interface, and the interface resistance is believed to be higher. Thus, it is possible that a monolayer of free metal at the interface is beneficial to its electrical properties. In future studies of ZnO, we intend to expose the surface of the material to various controlled chemical treatments while probing by RTSE. In this way, we will attempt to establish treatment conditions that yield a free Zn monolayer at the surface. Solar cells will be prepared on surfaces with and without the treatments, and an assessment of their performance will be undertaken.

(5-6) Solar cells will be co-deposited onto SnO_2 and ZnO under conditions used for our standard baseline cell in the single-chamber system. However, the TCO surfaces will be exposed to atomic H generated by a filament just prior to p-layer deposition. Each exposure will be performed under real-time control by SE in order to generate an accurately-determined mass thickness of metal at the SnO_2/p-layer interface and a well-defined carrier concentration gradient at the ZnO/p-layer interface. The resulting solar cells will be characterized and compared to control cells prepared without the H-treatments. The effect of the TCO/p-layer interface effects on the solar cell parameters will be accurately determined. The mass thickness of metal at the SnO_2 p-layer interface will be correlated with the long term stability of the solar cell. Similar studies of the effect of TCO/p-layer interface problems on the solar cell performance will also be studied for devices prepared in our multichamber system. This study may lead to further information on how to reduce TCO/p-layer interface problems.

(7-9) We will not continue in our attempts to prepare p-type microcrystalline SiC alloy films with the conventional PECVD methods because of the ability of C to stabilize an amorphous component in the film under these conditions. Unless one can prepare µc-Si:H onto the TCO surface, the microcrystalline SiC alloy will be out of the question. The work described in this report suggests that the next step is to study the nucleation and microstructural evolution of µc-Si:H on ZnO substrates, due to the resistance of the latter to reduction by atomic H. If a 200 Å coalesced and dominantly crystalline Si film cannot be prepared onto ZnO because of the low nucleation density, or due to etching of the ZnO by the plasma, then a sequence of a-Si:H:B growth/etching cycles will be utilized to seed the substrate with a dense 50 Å microcrystalline layer. This will promote the further growth of a thicker µc-Si:H:B by PECVD on the surface. If such a process is found to be successful on the basis of the RTSE analysis, then the procedure will be incorporated into our baseline solar cells in single- and multi- chamber systems. Materials studies will focus on the preparation of doped microcrystalline silicon carbide by microwave plasma CVD, starting with the conditions for diamond growth.

(10-11) The efficiency of solar cells prepared in our single-chamber system appears to be limited by the p/i interface quality, in particular the B-contamination that is formed during single-chamber flushing between depositing the p- and i-layers. In future work, procedures to eliminate this effect and optimize the efficiency of solar cells in our single-chamber system will be studied using RTSE. These include atomic H and plasma treatments after p-layer deposition, buffer layers, and the use of tri-methyl boron dopant gas. As improvements are uncovered, they will also be incorporated into the multichamber solar cell preparation process in attempts to further improve the baseline solar cell efficiency. If graded buffer layers are found to be important, procedures will be developed in the single-chamber system for automatic band gap control at the p/i interface.

8. References

An, I.; Li, Y.M.; Wronski, C.R.; Collins, R.W. (1993). Phys. Rev. B **48**, p. 4464.

An, I.; Lu, Y.; Wronski, C.R.; Collins, R.W. (1994). Appl. Phys. Lett. (in press).

Asano, A. (1990). Appl. Phys. Lett. **56**, p. 533.

Aspnes, D.E.; Studna, A.A. (1983). Phys. Rev. B **27**, p.985.

Azzam, R.M.A.; Bashara, N.M. (1977). *Ellipsometry and Polarized Light.* Amsterdam: North-Holland.

Berggren K.-F.; Sernelius, B.E. (1981). Phys. Rev. B **24**, p. 1971.

Burstein, E. (1954). Phys. Rev. **93**, p. 632.

Camargo, S.S.; Beyer, W. (1989). J. Non-Cryst. Solids **114**, p. 807.

Chen, I.; Wronski, C.R. (1993). Unpublished results.

Cody, G.D. (1984). In J.I. Pankove (ed.) *Semiconductors and Semimetals*, Vol. 21-B. New York, NY: Academic, p. 11.

Collins, R.W. (1988). Appl. Phys. Lett. **53**, p. 1086.

Collins, R.W.; Cavese, J.M. (1988). Mater. Res. Soc. Symp. Proc. **118**, p. 19.

Collins, R.W.; Wronski, C.R.; An, I.; Lu, Y.; Nguyen, H.V. (1992). "In-Situ Characterization of Growth and Interfaces in a-Si:H Devices". NREL Annual Subcontract Report for 1 May 1991 - 30 April 1992, TP-451-5265 Golden, CO: NREL.

Collins, R.W.; Wronski, C.R.; An, I.; Lu, Y.; Nguyen, H.V. (1994a). "In-Situ Characterization of Growth and Interfaces in a-Si:H Devices". NREL Annual Subcontract Report for 1 May 1992 - 30 April 1993, TP-451-6135 Golden, CO: NREL.

Collins, R.W.; An, I.; Nguyen, H.V.; Li, Y.; Lu, Y. (1994b). In M. Francombe and J. Vossen (eds.) *Physics of Thin Films*, Vol. 19. New York, NY: Academic, p. 49.

Jin, Z.-C.; Hamberg, I.; Granqvist, C.G. (1988). J. Appl. Phys. **64**, p. 5117.

Lautenschlager, P.; Garriga, M.; Vina, L.; Cardona, M. (1987). Phys. Rev. B **36**, p. 4821.

Li, Y.M.; An, I.; Nguyen, H.V.; Wronski, C.R.; Collins, R.W. (1992). Phys. Rev. Lett. **68**, p. 2814.

Lu, Y.; Kim, S.; Gunes, M.; Lee, Y.; Wronski, C.R.; Collins, R.W. (1994). Mater. Res. Soc. Symp. Proc. (in press).

Lu, Y.; An, I.; Gunes, M.; Wakagi, M.; Wronski, C.R.; Collins, R.W. (1993). Appl. Phys. Lett. 63, p. 2228.

Luft, W.; Tsuo, Y.S. (1993). *Hydrogenated Amorphous Silicon Deposition Processes.* New York, NY: Marcel-Dekker.

Mahan, H.; von Roedern, B.; Williamson, D.L.; Madan, A. (1985). J. Appl. Phys. **57**, p. 2717.

Matsuda, A.; Tanaka, K. (1987). J. Non-Cryst. Solids **97&98**, p. 1367.

Moss, T.S. (1954). Proc. Phys. Soc. London, Ser. B **67**, p. 775.

Nguyen, H.V.; Collins, R.W. (1993). Phys. Rev. B **47**, p. 1911.

Nguyen, H.V.; Collins, R.W. (1994). Unpublished results.

Prasad, K.; Kroll, U.; Finger, F.; Shah, A.; Dorier, J.-L.; Howling, A.; Baumann, J.; Schubert, M. (1991). Mater. Res. Soc. Symp. Proc. **219**, p. 469.

Stutzmann, M.; Jackson, W.B.; Tsai, C.C. (1985). Phys. Rev. B **32**, p. 23.

Tsai, C.C. (1988). In H. Fritzsche (ed.) *Amorphous Silicon and Related Materials*, Vol. 1. Singapore: World Scientific, p. 123.

von Roedern, B. (1993). Personal communication.

Weiser, G.; Mell, H. (1989). J. Non-Cryst. Solids **114**, p. 298.

Wooten, F. (1972). *Optical Properties of Solids*. New York, NY: Academic.

Yang, Y.H.; Katiyar, M.; Abelson, J.R.; Maley, N. (1993). Mater. Res. Soc. Symp. Proc. **297**, p. 25.

9. Bibliography of Published Work

An, I.; Li, Y.M.; Nguyen, H.V.; Wronski, C.R.; Collins, R.W. (1991). "In situ determination of dielectric functions and optical gap of ultrathin a-Si:H by real time spectroscopic ellipsometry," Appl. Phys. Lett. **59**, pp. 2543-2545.

An, I.; Li, Y.M.; Wronski, C.R.; Collins, R.W. (1992). "Modification of a-Si(:H) by Thermally- Generated Atomic Hydrogen: A Real Time Spectroscopic Ellipsometry Study of Si Bond Breaking," Mater. Res. Soc. Symp. Proc. **258**, pp. 27-32.

An, I.; Li, Y.M.; Wronski, C.R.; Collins, R.W. (1993). "Sub-surface equilibration of hydrogen with the a-Si:H network under film growth conditions," Mater. Res. Soc. Symp. Proc. **297**, pp. 43-48.

An, I.; Li, Y.M.; Wronski, C.R.; Collins, R.W. (1993). "Chemical equilibration of plasma-deposited amorphous silicon with thermally generated atomic hydrogen," Phys. Rev. B **48**, pp. 4464-4472.

An, I.; Collins, R.W.; Nguyen, H.V.; Vedam, K.; Witham, H.S.; Messier, R. (1993). "Hydrogen diffusion and reaction processes in thin films investigated by real time spectroscopic ellipsometry," Thin Solid Films **233**, pp. 276-280.

An, I.; Nguyen, H.V.; Heyd, A.R.; Collins, R.W. (1994). "Simultaneous real time spectroscopic ellipsometry and reflectance for monitoring semiconductor and thin film preparation," Mater. Res. Soc. Symp. Proc. (in press).

An, I.; Lu, Y.; Wronski, C.R.; Collins, R.W. (1994). "A real time spectroellipsometry study of the interaction of hydrogen with ZnO during ZnO/a-$Si_{1-x}C_x$:H interface formation," Appl. Phys. Lett. (in press).

An, I.; Nguyen, H.V.; Heyd, A.R.; Collins, R.W. (1994). "Simultaneous real time spectroscopic ellipsometry and reflectance for monitoring thin film preparation, Rev. Sci. Instrum. (submitted).

Collins, R.W.; An, I.; Li, Y.M.; Wronski, C.R. (1992). "Surface Microstructural Evolution of Ultrathin Films," in K.S. Liang, M.P. Anderson, and R.F. Bruinsma (eds.) *Interface Dynamics and Growth*, Pittsburgh: MRS, Vol. 237.

Collins, R.W.; Wronski, C.R.; An, I.; Li, Y.M. (1992). "In-situ characterization of growth and interfaces in a-Si:H devices," in *Annual Report Photovoltaic Subcontact Program FY 1991*, TP-410-4724, Golden, CO: NREL, pp. 55-60.

Collins, R.W.; Wronski, C.R.; An, I.; Li, Y.M. (1992). "In-situ characterization of growth and interfaces in a-Si:H devices," NREL Annual Subcontract Report for 1 May 1991 - 30 April 1992, TP-451-5265, Golden, CO: NREL.

Collins, R.W.; An, I.; Nguyen, H.V.; Lu, Y. (1993). "Real time spectroscopic ellipsometry for characterization of nucleation, growth, and optical functions of thin films," Thin Solid Films **233**, pp. 244-252.

Collins, R.W.; An, I.; Heyd, A.R.; Li, Y.M.; Wronski, C.R. (1993). "Real time spectroscopic ellipsometry monitoring of semiconductor growth and etching," in Z.C. Feng (ed.) *Semiconductor Interfaces, Microstructures, and Devices: Properties and Applications*, Philadelphia: Institute of Physics, pp. 55-86.

Collins, R.W. (1993). "Multichannel spectroscopic ellipsometry for real time analysis of electrochemical and plasma deposition of thin films," in N. Masuko, T. Osaka, and Y. Fukunaka (eds.) *New Trends and Approaches in Electrochemical Technology*, Tokyo, Japan: Kodansha, pp. 115-150.

Collins, R.W.; Wronski, C.R.; An, I.; Li, Y.M.; Lu, Y. (1993). "In-situ characterization of growth and interfaces in a-Si:H devices," in *Annual Report Photovoltaic Subcontact Program FY 1992*, Golden, CO: NREL, pp. 206-209.

Collins, R.W.; Wronski, C.R.; An, I.; Lu, Y.; Nguyen, H.V. (1994). "In-situ characterization of growth and interfaces in a-Si:H devices". NREL Annual Subcontract Report for 1 May 1992 - 30 April 1993, TP-451-6135, Golden, CO: NREL.

Collins, R.W.; Wronski, C.R.; An, I.; Lu, Y.; Nguyen, H.V. (1994). "In-situ characterization of growth and interfaces in a-Si:H devices". NREL Final Subcontract Report for 1 May 1991 - 31 May 1994, This report, Golden, CO: NREL.

Collins, R.W.; An, I.; Nguyen, H.V.; Li, Y.; Lu, Y. (1994). "Real time spectroscopic ellipsometry studies of the nucleation, growth, and optical properties of thin films, part I: tetrahedrally-bonded thin films," in M. Francombe and J. Vossen (eds.) *Physics of Thin Films*, Vol. 19. New York, NY: Academic, p. 49-125.

Collins, R.W.; Wronski, C.R.; An, I.; Lu, Y. Nguyen, H.V. (1994). "In-situ characterization of growth and interfaces in a-Si:H devices," in *Annual Report Photovoltaic Subcontact Program FY 1993*, Golden, CO: NREL, (in press).

Dawson, R.M.A.; Li, Y.M.; Gunes, M.; Nag, S.; Collins, R.W.; Bennett, M.; Wronski, C.R. (1992). "Optical properties of the component materials in multijunction hydrogenated amorphous silicon-based solar cells", in *Proceedings of the Eleventh European Photovoltaic and Solar Energy Conference and Exhibition*, Montreux, Switzerland, October 1992.

Dawson, R.M.; Li, Y.M.; Gunes, M.; Heller, D.; Nag, S.; Collins, R.W.; Wronski, C.R.; Bennett, M.; Li, Y.M. (1993). "Optical properties of hydrogenated amorphous silicon, silicon-germanium, and silicon-carbon alloy thin films," Mater. Res. Soc. Symp. Proc. **258**, pp. 595-600.

Dawson, R.M.A.; Fortmann, C.M.; Gunes, M.; Li, Y.M.; Nag, S.S.; Collins, R.W.; Wronski, C.R. (1993). "Effects of microstructure on transport properties of undoped hydrogenated amorphous silicon films," Appl. Phys. Lett. **63**, pp. 955-957.

Dawson, R.M.A.; Fortmann, C.M.; Gunes, M.; Li, Y.M.; Nag, S.S.; Wronski, C.R.; Collins, R.W. (1993). "Transport considerations in hydrogenated amorphous silicon materials with widely mobilities and the consequences on device performance," in *Proceedings of the 23rd IEEE Photovoltaic Specialists Conference*, Louisville, KY; May, 1993 (in press).

Flueckiger, R.; Meier, J.; Shah, A.; Catana, A.; Brunel, M.; Nguyen, H.V.; Collins, R.W.; Carius, R. (1994). "Structural, optical, and electrical properties of <p> μc-Si:H very thin films deposited by the VHF-GD technique," Mater. Res. Soc. Symp. Proc. (in press).

Li, Y.M.; An, I.; Nguyen, H.V.; Wronski, C.R.; Collins, R.W. (1991). "Real Time Spectroscopic Ellipsometry Determination of the Evolution of Amorphous Semiconductor Optical Functions, Bandgap, and Microstructure," J. Non-Cryst. Solids **137&138**, pp. 787-790.

Li, Y.M.; Dawson, R.M.; Collins, R.W.; Wronski, C.R.; Wiedeman, S. (1991). "Effect of Surface Recombination on the Spectral Dependence of Photocurrent in Intrinsic Hydrogenated Amorphous Silicon Films," Appl. Phys. Lett. **59**, pp. 2549-2551.

Li, Y.M.; An, I.; Nguyen, H.V.; Wronski, C.R.; Collins, R.W. (1992). "Thin-film coalescence in hydrogenated amorphous silicon probed by spectroscopic ellipsometry with millisecond resolution," Phys. Rev. Lett. **68**, pp. 2814-2817.

Li, Y.M.; An, I.; Gunes, M.; Dawson, R.M.; Collins, R.W.; Wronski, C.R. (1992). "Optoelectronic Properties of Plasma CVD a-Si:H Modified by Filament-Generated Atomic H," Mater. Res. Soc. Symp. Proc. **258**, pp. 57-62.

Lu, Y.; An, I.; Gunes, M.; Wakagi, M.; Wronski, C.R.; Collins, R.W. (1993). "Effect of gas phase hydrogen-dilution on the nucleation, growth, and interfaces of a-$Si_{1-x}C_x$:H," Mater. Res. Soc. Symp. Proc. **297**, pp. 31-36.

Lu, Y.; An, I.; Gunes, M.; Wakagi, M.; Wronski, C.R.; Collins, R.W. (1993). "Nucleation and growth of hydrogenated amorphous silicon-carbon alloys: effect of hydrogen dilution in plasma-enhanced chemical vapor deposition, " Appl. Phys. Lett. **63**, pp. 2228-2230.

Lu, Y.; Kim, S.; Gunes, M.; Lee, Y.; Wronski, C.R.; Collins, R.W. (1994). "Process-property relationships for a-SiC:H deposition: excursions in parameter space guided by real time spectroellipsometry, " Mater. Res. Soc. Symp. Proc. (in press).

Lu, Y.; Kim, S.; Chen, I.; Lee, Y.; Fortmann, C.M.; Wronski, C.R.; Collins, R.W. (1994). "Real time characterization of the interface structures during the preparation of amorphous silicon-based solar cells," First World Conference on Photovoltaic Energy Conversion, (submitted).

Nguyen, H.V.; An, I.; Li, Y.M.; Wronski, C.R.; Collins, R.W. (1992). "Optical Properties and Structure of Microcrystalline Silicon," Mater. Res. Soc. Symp. Proc. **258**, pp. 235-240.

Nguyen, H.V.; Collins, R.W. (1993). "Finite-size effects on the optical properties of Si nanocrystallites: a real time spectroellipsometry study," Phys. Rev. B **47**, pp. 1911-1917.

Nguyen, H.V.; Collins, R.W. (1993). "Analysis of critical points in semiconductor optical functions from in situ and real time spectroscopic ellipsometry," Thin Solid Films **233**, pp. 272-275.

Nguyen, N.V.; An, I.; Collins, R.W.; Lu Y.; Wakagi, M.; Wronski, C.R. (1994). "Ellipsometry- Controlled Preparation of Ultrathin Microcrystalline Silicon Layers by Atomic Hydrogen Etching of Amorphous Silicon," Appl. Phys. Lett. (submitted).

Wronski, C.R.; Dawson, R.M.A.; Gunes, M.; Li, Y.M.; Collins, R.W. (1993). "Photocarrier transport and recombination in amorphous silicon," Mater. Res. Soc. Symp. Proc. **297**, pp. 443-454.

REPORT DOCUMENTATION PAGE

Form Approved
OMB NO. 0704-0188

1. AGENCY USE ONLY (Leave blank)

2. REPORT DATE
July 1994

3. REPORT TYPE AND DATES COVERED
Final Subcontract Report, 1 May 1991 - 31 May 1994

4. TITLE AND SUBTITLE
In-Situ Characterization of Growth and Interfaces in a-Si:H Devices

5. FUNDING NUMBERS
C: XG-1-10063-10
TA: PV431101

6. AUTHOR(S)
R. W. Collins, C. R. Wronski, I. An, Y. Lu, H. V. Nguyen

7. PERFORMING ORGANIZATION NAME(S) AND ADDRESS(ES)
Pennsylvania State University
Materials Research Laboratory
University Park, PA 16802

8. PERFORMING ORGANIZATION REPORT NUMBER

9. SPONSORING/MONITORING AGENCY NAME(S) AND ADDRESS(ES)
National Renewable Energy Laboratory
1617 Cole Blvd.
Golden, CO 80401-3393

10. SPONSORING/MONITORING AGENCY REPORT NUMBER
TP-451-7045
DE94011847

11. SUPPLEMENTARY NOTES
NREL Technical Monitor: B. von Roedern

12a. DISTRIBUTION/AVAILABILITY STATEMENT

12b. DISTRIBUTION CODE
UC-271

13. ABSTRACT *(Maximum 200 words)*

This report describes work to identify materials parameters that can quantitatively describe the solar cell performance correctly in th initial and stabilized states and are consistent with a microscopic model of the metastable defect site. The objective is to be accomplished by applying results of in-situ analyses of a-Si:H surfaces and the transparent conducting oxide (TCO)/p/i interfaces to complement the present understanding of the electronic properties of materials and devices. A second objective of the program is demonstrate, characterize, and understand improved doped and undoped "wide-gap" materials for use in achieving 15% stabilized photovoltaic modules ("wide-gap" materials are defined as those materials with a band gap of at least 1.9 eV).

14. SUBJECT TERMS
characterization ; amorphous silicon ; devices ; material growth ; photovoltaics ; solar cells

15. NUMBER OF PAGES
102

16. PRICE CODE
A06

17. SECURITY CLASSIFICATION OF REPORT
Unclassified

18. SECURITY CLASSIFICATION OF THIS PAGE
Unclassified

19. SECURITY CLASSIFICATION OF ABSTRACT
Unclassified

20. LIMITATION OF ABSTRACT
UL